

# SEARCH FOR

$$(J/\psi, \psi(2S)) \rightarrow \Xi^0(1530)\bar{\Xi}^0(1530)$$



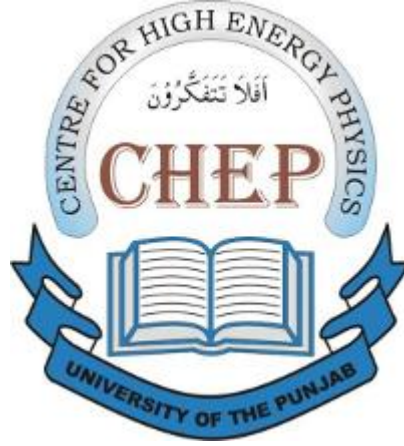
AZMAT IQBAL

**Centre for High Energy Physics  
University of the Punjab  
Lahore-54590, Pakistan**

(August, 2012)

# SEARCH FOR

$$( J / \psi, \psi(2S) ) \rightarrow \Xi^0(1530) \bar{\Xi}^0(1530)$$



by

AZMAT IQBAL

Submitted in Partial Fulfillment of the Requirements for the  
Degree of DOCTOR OF PHILOSOPHY

at

**Centre for High Energy Physics  
University of the Punjab  
Lahore-54590, Pakistan**

(August, 2012)

---

DEDICATED  
TO  
MY PARENTS, SISTERS AND BROTHERS

---

# CERTIFICATE

It is certified that I have read this dissertation and that, in my opinion, it is fully adequate in scope and quality for the degree of Doctor of Philosophy.

Prof. Shan Jin  
(Supervisor)

Prof. Dr. Haris Rashid  
(Supervisor)

Submitted Through:

Prof. Dr. Haris Rashid  
(Supervisor and Director)

---

# DECLARATION

This work represents the efforts of the members of BES Group at the Centre for High Energy Physics University of the Punjab, Pakistan. I claim the credit for the analysis and final results presented in this thesis which are entirely my own.

This thesis which is being submitted for the award of degree of Ph.D. in the university of the Punjab does not contain material which has been submitted for the award of any other degree or diploma in any university. To the best of my knowledge and belief, it does not contain any material published or written by another person, except with due references. If any reference is found missing that would completely be unintentional and I do not pretend to own the credit for that.

Azmat Iqbal

# Acknowledgment

All praise and glory to be Allah Mighty who gave me strength and courage to finish this project. My humblest and sincerest tribute to the Holy Prophet (Peace and Blessings be Upon Him) Who is a permanent source of guidance for the humanity. I offer sincere thanks to my supervisors; Prof. Dr. Haris Rashid and Prof. Dr. Shan Jin. I warmly express my gratitude to Prof. Dr. Haris Rashid for his valuable suggestions and guidance throughout the project. It is great pleasure for me to offer my thanks to him for giving me an opportunity to work in the prestigious BESIII Collaboration. His encouraging and facilitating role has been a great source of motivation for me in completing thesis work.

I express my sincerest gratitude to Dr. Talab Hussain and Dr. Abrar Ahmad Zafar who played a vital role in the completion of my thesis work. Their guidance and help from the very first day till the instant has made all this research work possible for me. Their encouragement and motivation would always instill in me a new confidence and spirit to move ahead on right time. I am extremely indebted to Dr. Talab Hussain for many inspiring and enlightening discussions from which I learnt a lot. I am really grateful to him for making me familiar with intricacies of data analysis and experimental techniques. Working with both of them on this journey of learning and sharing ideas turned out to be most memorable moments of my life. I am also very grateful to Dr. Qadeer Afzal for some valuable comments and suggestions.

I am extremely thankful to all my fiends and colleagues especially Mr. Ghulam Mustafa, Dr. M. Imran Jamil, Mr. Muhammad Mushraf Ansari and Mr. Sohail Gillani for their

---

continuous encouragement and help during my research work. Working together with Mr. Mushraf Ansari in BESIII computational environment turned out be a great experience. I am especially thankful to him for helping me in computer related issues.

Without any exception, I am pleased to thank all teachers from whom I gained a considerable deal of knowledge during my stay at CHEP. I am also grateful to other staff member of CHEP for their sincere cooperation.

I also thank to Higher Education Commission (HEC) of Pakistan for the support during my Ph.D. research work.

My urge to learn science led me to pursue a carrier in physics. I started my journey of learning physics and nature as a lay man knowing little about both. It was my luck that struck in a way and I got company of some great teachers right from school age to this level. Here I also wish to thank all my teachers whose contributions and efforts will be always a great treasure for me.

In the last but not the least, I feel immense pleasure to express deep gratitude to my mother and father, brothers and sisters for their never falling love, care and support for my studies. Without their untiring and sincerest efforts nothing could have been possible. I am at loss for words to express their courage, determination and patience which will be an everlasting source of inspiration and motivation for me. I am short of words to describe how they sacrificed their lives, sleep and peace to put me on the noble path of knowledge. I owe a lot to my elder brother Ali Akram (late) who played an impressive role in my studies. May Allah Mighty rest his soul in peace and shower His countless blessings on him.

---

# Abstract

Based upon analysis work performed using samples of  $2.25 \times 10^8$   $J/\psi$  events and  $1.06 \times 10^8$   $\psi(2S)$  events collected with the BESIII detector at  $e^-e^+$  BEPC II collider in 2009, we report the first measurement of the branching ratios of the decay channels:

$(J/\psi, \psi(2S)) \rightarrow \Xi^0(1530)\bar{\Xi}^0(1530)$ . The measured branching ratios are:

$$Br^{1C}[J/\psi \rightarrow \Xi^0(1530)\bar{\Xi}^0(1530)] = (1.06 \pm 0.07_{sys} \pm 0.37_{stat}) \times 10^{-5}$$

$$Br^{4C}[J/\psi \rightarrow \Xi^0(1530)\bar{\Xi}^0(1530)] = (2.94 \pm 0.06_{sys} \pm 1.10_{stat}) \times 10^{-5}.$$

$$Br^{1C}[\psi(2S) \rightarrow \Xi^0(1530)\bar{\Xi}^0(1530)] = (1.16 \pm 0.77_{sys} \pm 0.07_{stat}) \times 10^{-6}$$

$$Br^{4C}[\psi(2S) \rightarrow \Xi^0(1530)\bar{\Xi}^0(1530)] = (5.16 \pm 1.92_{sys} \pm 0.17_{stat}) \times 10^{-6}.$$

The 4C and 1C results are consistent within  $2\sigma$ . The test results of the 12 % rule are:

$$\frac{Br^{1C}(\psi(2S) \rightarrow B\bar{B})}{Br^{1C}(J/\psi \rightarrow B\bar{B})} \approx 11\%$$

$$\frac{Br^{4C}(\psi(2S) \rightarrow B\bar{B})}{Br^{4C}(J/\psi \rightarrow B\bar{B})} \approx 17.55\%$$

# List of Figures

2.1	Feynman diagrams depicting the three fundamental interactions [15] . . . .	10
2.2	(a,b) Variation of coupling constants of QCD and QED due to screening and antiscreening effects. (a) The strength of QED $\alpha$ decreases with separation of test charge from the source. (b) The strength of QCD $\alpha_s$ increases with the separation of test color charge (another quark) due to the antiscreening effect of gluon self-coupling (c) $\alpha$ is finite at $r \rightarrow \infty (q^2 = 0)$ and increases at shorter distances due to weak screening. $\alpha_s$ is meaningless at large distances $\geq 10^{-13}$ cm because of confinement and is small at short distances. [26] . . .	18
3.1	Baryon multiplets: Baryon octet or $J^p = (1/2)^+$ SU(3) multiplets (left). Baryon decuplet or $J^p = (3/2)^+$ SU(3) multiplets (right), where 1/2 stands for spin and + for even parity and so on [3, 5]. . . . .	25
3.2	Meson Multiplets: (A) Pseudoscalar meson octet with $J^p = 0^-$ . (B) Vector meson octet with $J^p = 1^-$ [3, 5]. . . . .	25
3.3	Quark structure of baryon octet or $J^p = (1/2)^+$ SU(3) multiplets [25]. . . .	27
3.4	Baryon decuplet or $J^p = (3/2)^+$ SU(3) multiplets [25]. . . . .	27
3.5	SU(4) multiplets of :(a) $(1/2)^+$ baryons (b) $(3/2)^+$ baryons [3, 26]. . . . .	29
3.6	SU(3) multiplets of :(a) pseudoscalar and (b) vector mesons [3, 26]. . . . .	30
3.7	SU(4) multiplets of :(a) pseudoscalar mesons (b) vector mesons [3, 26]. . .	30
4.1	Schematic diagram for production of $(J/\psi)$ in $e^+e^-$ collision [54]. . . . .	36

4.2	Narrow resonance peak of $J/\psi$ in $e^-e^+$ at SLAC [25, 55, 56]. . . . .	36
4.3	Narrow resonance peak of $J/\psi$ in PP collisions at BNL respectively [25, 55, 56].	37
4.4	Comparison between energy level diagram of positronium and charmonium [46]. . . . .	38
4.5	Experimentally observed and theoretically predicted charmonium states. The experimentally established states are shown with solid lines. The dotted lines on the left show the predicted states by a non-relativistic potential model while the right dotted lines show the states predicted by the relativistic Godfrey Isgur potential model [8, 61]. . . . .	38
4.6	Approximate QCD static quarkonium potential as a function of interquark separation $r$ [4, 33]. . . . .	39
4.7	Quark diagrams for decay of $\phi$ into decay mesons. (a) OZI suppressed transition (b) OZI allowed transition [4]. . . . .	42
4.8	Quark diagrams for $J/\psi$ decaying to mesons. (a) OZI allowed transition (b) OZI suppressed transition [5]. . . . .	43
5.1	Schematic diagram for $e^+e^-$ BEPCII collider and BESIII detector [68]. . .	49
5.2	Schematic diagram of MDC [68]. . . . .	51
5.3	Schematics of TOF [68]. . . . .	52
5.4	Schematic diagram for EMC [68]. . . . .	53
5.5	Schematic diagram for muon chamber [68]. . . . .	54
6.1	MC and data invariant mass distributions of $p\pi^-$ and $\bar{p}\pi^+$ after kinematic fit results . . . . .	61
6.2	MC and data invariant mass distributions for $\Lambda\pi^-$ and $\bar{\Lambda}\pi^+$ after kinematic fit results . . . . .	62
6.3	MC and data invariant mass distributions for $\Xi^-\pi^+$ and $\bar{\Xi}^+\pi^-$ after kinematic fit results . . . . .	63

6.4	MC and data invariant mass distributions for $p\pi^-$ and $\bar{p}\pi^+$ after final event selection criteria . . . . .	64
6.5	MC and data invariant mass distributions for $\Lambda\pi^-$ and $\bar{\Lambda}\pi^+$ after final event selection criteria . . . . .	65
6.6	MC and data invariant mass distributions for $\Xi^-\pi^+$ and $\bar{\Xi}^+\pi^-$ after final event selection criteria . . . . .	66
6.7	MC and data invariant mass distribution for $p\pi^-$ and $\bar{p}\pi^+$ after 1C fit results	67
6.8	MC and data invariant mass distribution for $\Lambda\pi^-$ and $\bar{\Lambda}\pi^+$ after 1C fit results	68
6.9	MC and data invariant mass distribution for $\Xi^-\pi^+$ and $\bar{\Xi}^+\pi^-$ after 1C fit results . . . . .	69
6.10	MC and data invariant mass distribution for $p\pi^-$ and $\bar{p}\pi^+$ after 4C fit results	70
6.11	MC and data invariant mass distribution for $\Lambda\pi^-$ and $\bar{\Lambda}\pi^+$ after 4C fit results	71
6.12	MC and data invariant mass distribution for $\Xi^-\pi^+$ and $\bar{\Xi}^+\pi^-$ after 4C fit results . . . . .	72
6.13	$M_{\Xi^-\pi^+}$ and $M_{\bar{\Xi}^+\pi^-}$ distribution . . . . .	73
6.14	$M_{\Xi^-\pi^+}$ and $M_{\bar{\Xi}^+\pi^-}$ distribution . . . . .	73
6.15	$M_{\Xi^-\pi^+}$ and $M_{\bar{\Xi}^+\pi^-}$ distribution . . . . .	74
6.16	$M_{\Xi^-\pi^+}$ and $M_{\bar{\Xi}^+\pi^-}$ distribution . . . . .	74
6.17	Scatter plot of $M_{\Xi^-\pi^+}$ VS $M_{\bar{\Xi}^+\pi^-}$ distribution after 1C and 4C fit results for MC exclusive decay channel $J/\psi \rightarrow \Lambda^0(1405)\bar{\Lambda}^0(1405)$ , where $\Lambda^0(1405) \rightarrow \Sigma^{*+}\pi^-$ , $\bar{\Lambda}^0(1405) \rightarrow \bar{\Sigma}^{*-}\pi^+$ , $\Sigma^{*+} \rightarrow \Lambda\pi^+$ , $\Lambda \rightarrow \pi^-p$ , $\bar{\Sigma}^{*-} \rightarrow \bar{\Lambda}\pi^-$ , $\bar{\Lambda} \rightarrow \bar{p}\pi^+$ .	75
6.18	Scatter plot of $M_{\Xi^-\pi^+}$ VS $M_{\bar{\Xi}^+\pi^-}$ distribution after 1C and 4C fit results for MC exclusive decay channel $J/\psi \rightarrow \Lambda^0(1405)\bar{\Lambda}^0(1405)$ , where $\Lambda^0(1405) \rightarrow \Sigma^{*-}\pi^+$ , $\bar{\Lambda}^0(1405) \rightarrow \bar{\Sigma}^{*+}\pi^-$ , $\Sigma^{*-} \rightarrow \Lambda\pi^-$ , $\Lambda \rightarrow \pi^-p$ , $\bar{\Sigma}^{*+} \rightarrow \bar{\Lambda}\pi^+$ , $\bar{\Lambda} \rightarrow \bar{p}\pi^+$ .	75
6.19	Scatter plot of $M_{\Xi^-\pi^+}$ VS $M_{\bar{\Xi}^+\pi^-}$ distribution after 1C and 4C fit results for MC exclusive decay channel $J/\psi \rightarrow \Xi^-\bar{\Xi}^+\pi^+\pi^-$ , where $\Xi^- \rightarrow \Lambda\pi^-$ , $\Lambda \rightarrow \pi^-p$ and $\bar{\Xi}^+ \rightarrow \bar{\Lambda}\pi^+$ , $\bar{\Lambda} \rightarrow \pi^+\bar{p}$ . . . . .	76

6.20	Scatter plot of $M_{\Xi^-\pi^+}$ VS $M_{\Xi^+\pi^-}$ distribution after 1C and 4C fit results for MC exclusive decay channel $J/\psi \rightarrow \Lambda^0(1520)\bar{\Lambda}^0(1520)$ , where $\Lambda^0(1520) \rightarrow \Lambda\pi^+\pi^-$ , $\Lambda \rightarrow p\pi^-$ , $\bar{\Lambda}^0(1520) \rightarrow \bar{\Lambda}\pi^+\pi^-$ , $\bar{\Lambda} \rightarrow \bar{p}\pi^+$ . . . . .	76
6.21	Scatter plot of $\Xi^-\pi^+$ VS $\bar{\Xi}^+\pi^-$ after 1C and 4C fit results for the signal decay channel $J/\psi \rightarrow \Xi^0(1530)\bar{\Xi}^0(1530)$ . . . . .	77
6.22	MC and data invariant mass distribution for $p\pi^-$ and $\bar{p}\pi^+$ after kinematic fit	78
6.23	MC and data invariant mass distribution for $\Lambda\pi^-$ and $\bar{\Lambda}\pi^+$ after kinematic fit . . . . .	79
6.24	MC and data invariant mass distribution for $\Xi^-\pi^+$ and $\bar{\Xi}^+\pi^-$ after kinematic fit . . . . .	80
6.25	MC and data invariant mass distribution for $p\pi^-$ and $\bar{p}\pi^+$ after final event selection . . . . .	80
6.26	MC and data invariant mass distribution for $\Lambda\pi^-$ and $\bar{\Lambda}\pi^+$ after final event selection . . . . .	81
6.27	MC and data invariant mass distribution for $\Xi^-\pi^+$ and $\bar{\Xi}^+\pi^-$ after final event selection . . . . .	82
6.28	MC and data invariant mass spectra for $p\pi^-$ and $\bar{p}\pi^+$ after 1C fit results. .	82
6.29	MC and data invariant mass spectra for $\Lambda\pi^-$ and $\bar{\Lambda}\pi^+$ after 1C fit results.	83
6.30	MC and data invariant mass spectra for $\Xi^-\pi^+$ and $\bar{\Xi}^+\pi^-$ after 1C fit results.	83
6.31	MC and data invariant mass spectra for $p\pi^-$ and $\bar{p}\pi^+$ after 4C fit results. .	84
6.32	MC and data invariant mass spectra for $\Lambda\pi^-$ and $\bar{\Lambda}\pi^+$ after 4C fit results.	84
6.33	MC and data invariant mass spectra for $\Xi^-\pi^+$ and $\bar{\Xi}^+\pi^-$ after 4c fit results.	85
6.34	Invariant mass spectrum of $\Xi(1530)^0$ and $\bar{\Xi}(1530)^0$ for MC exclusive background decay channel $\psi(2S) \rightarrow \Lambda(1520)\bar{\Lambda}(1520)$ . . . . .	85
6.35	Invariant mass spectrum of $\Xi^0(1530)$ and $\bar{\Xi}^0(1530)$ for MC exclusive background decay channel $\psi(2S) \rightarrow \Lambda^0(1690)\bar{\Lambda}^0(1690)$ . . . . .	86

- 6.36 Invariant mass spectrum of  $\Xi^0(1530)$  and  $\bar{\Xi}^0(1530)$  for MC exclusive background decay channel  $\psi(2S) \rightarrow \Lambda^0(1520)\bar{\Lambda}^0(1520)$  where  $\Lambda^0(1520) \rightarrow \Sigma^{*+}\pi^-$ ,  $\bar{\Lambda}^0(1520) \rightarrow \bar{\Sigma}^{*-}\pi^+$ ,  $\Sigma^{*+} \rightarrow \Lambda\pi^+$ ,  $\Lambda \rightarrow \pi^-p$ ,  $\bar{\Sigma}^{*-} \rightarrow \bar{\Lambda}\pi^-$ ,  $\bar{\Lambda} \rightarrow \bar{p}\pi^+$  . . . . . 87
- 6.37 Invariant mass spectrum of  $\Xi^0(1530)$  and  $\bar{\Xi}^0(1530)$  for MC exclusive background decay channel  $\psi(2S) \rightarrow \Lambda^0(1520)\bar{\Lambda}^0(1520)$ , where  $\Lambda^0(1520) \rightarrow \Sigma^{*-}\pi^+$ ,  $\bar{\Lambda}^0(1520) \rightarrow \bar{\Sigma}^{*+}\pi^-$ ,  $\Sigma^{*-} \rightarrow \Lambda\pi^-$ ,  $\Lambda \rightarrow \pi^-p$ ,  $\bar{\Sigma}^{*+} \rightarrow \bar{\Lambda}\pi^+$ ,  $\bar{\Lambda} \rightarrow \bar{p}\pi^+$  . . . . . 87
- 6.38 Invariant mass spectrum of  $\Xi^0(1530)$  and  $\bar{\Xi}^0(1530)$  for MC exclusive background decay channel  $\psi(2S) \rightarrow \Xi^-\bar{\Xi}^+\pi^+\pi^-$  . . . . . 88
- 6.39 Scatter plot of  $M_{\Xi^-\pi^+}$  VS  $M_{\Xi^+\pi^-}$  distribution for MC exclusive decay channel  $\psi(2S) \rightarrow \Lambda^0(1520)\bar{\Lambda}^0(1520)$ , where  $\Lambda^0(1520) \rightarrow \Lambda\pi^+\pi^-$ ,  $\Lambda \rightarrow p\pi^-$ ,  $\bar{\Lambda}^0(1520) \rightarrow \bar{\Lambda}\pi^+\pi^-$ ,  $\bar{\Lambda} \rightarrow \bar{p}\pi^+$  . . . . . 88
- 6.40 Scatter plot of  $M_{\Xi^-\pi^+}$  VS  $M_{\Xi^+\pi^-}$  distribution for MC exclusive background decay channel  $\psi(2S) \rightarrow \Lambda^0(1690)\bar{\Lambda}^0(1690)$ , where  $\Lambda^0(1690) \rightarrow \Lambda\pi^+\pi^-$ ,  $\Lambda \rightarrow p\pi^-$ ,  $\bar{\Lambda}^0(1690) \rightarrow \bar{\Lambda}\pi^+\pi^-$ ,  $\bar{\Lambda} \rightarrow \bar{p}\pi^+$ . . . . . 89
- 6.41 Scatter plot of  $M_{\Xi^-\pi^+}$  VS  $M_{\Xi^+\pi^-}$  distribution for MC exclusive background decay channel  $\psi(2S) \rightarrow \Lambda^0(1520)\bar{\Lambda}^0(1520)$ , where  $\Lambda^0(1520) \rightarrow \Sigma^{*+}\pi^-$ ,  $\bar{\Lambda}^0(1520) \rightarrow \bar{\Sigma}^{*-}\pi^+$ ,  $\Sigma^{*+} \rightarrow \Lambda\pi^+$ ,  $\Lambda \rightarrow \pi^-p$ ,  $\bar{\Sigma}^{*-} \rightarrow \bar{\Lambda}\pi^-$ ,  $\bar{\Lambda} \rightarrow \bar{p}\pi^+$  . . . . . 89
- 6.42 Scatter plot of  $M_{\Xi^-\pi^+}$  VS  $M_{\Xi^+\pi^-}$  distribution for MC exclusive background decay channel  $\psi(2S) \rightarrow \Lambda^0(1520)\bar{\Lambda}^0(1520)$ , where  $\Lambda^0(1520) \rightarrow \Sigma^{*-}\pi^+$ ,  $\bar{\Lambda}^0(1520) \rightarrow \bar{\Sigma}^{*+}\pi^-$ ,  $\Sigma^{*-} \rightarrow \Lambda\pi^-$ ,  $\Lambda \rightarrow \pi^-p$ ,  $\bar{\Sigma}^{*+} \rightarrow \bar{\Lambda}\pi^+$ ,  $\bar{\Lambda} \rightarrow \bar{p}\pi^+$  . . . . . 90
- 6.43 Scatter plot of  $M_{\Xi^-\pi^+}$  VS  $M_{\Xi^+\pi^-}$  distribution for MC exclusive background decay channel  $\psi(2S) \rightarrow \Xi^-\bar{\Xi}^+\pi^+\pi^-$ , where  $\Xi^- \rightarrow \Lambda\pi^-$ ,  $\Lambda \rightarrow \pi^-p$  and  $\bar{\Xi}^+ \rightarrow \bar{\Lambda}\pi^+$ ,  $\bar{\Lambda} \rightarrow \pi^+\bar{p}$ . . . . . 90
- 6.44 Scatter plots of  $\Xi^-\pi^+$  vs  $\bar{\Xi}^+\pi^-$  after 1C and 4C fit results for the signal channel  $\psi(2S) \rightarrow \Xi^0(1530)\bar{\Xi}^0(1530)$ . . . . . 91

# List of Tables

2.1	Fundamental particles [8] . . . . .	6
2.2	Fundamental forces [8] . . . . .	9
6.1	MC inclusive background decay modes for the signal channel: $J/\psi \rightarrow \Xi^0(1530)\bar{\Xi}^0(1530)$ . . . . .	65
6.2	Systematic errors from 1C fit results for the signal channel: $J/\psi \rightarrow \Xi^0(1530)\bar{\Xi}^0(1530)$	77
6.3	Systematic errors from 4C fit results for the signal channel: $J/\psi \rightarrow \Xi^0(1530)\bar{\Xi}^0(1530)$	78
6.4	MC inclusive background decay modes for the signal channel: $\psi(2S) \rightarrow \Xi^0(1530)\bar{\Xi}^0(1530)$ . . . . .	86
6.5	Systematic errors from 1C fit results for the signal channel: $\psi(2S) \rightarrow \Xi^0(1530)\bar{\Xi}^0(1530)$ . . . . .	92
6.6	Systematic results from 4C fit results for the signal channel: $\psi(2S) \rightarrow \Xi^0(1530)\bar{\Xi}^0(1530)$ . . . . .	92

# Contents

<b>1</b>	<b>Introduction</b>	<b>1</b>
<b>2</b>	<b>The Standard Model</b>	<b>4</b>
2.1	Components of the Standard Model . . . . .	4
2.1.1	Fundamental Particles . . . . .	5
2.1.2	Fundamental Interactions . . . . .	7
2.1.3	Range of Interactions . . . . .	9
2.2	Quantum Field Theories . . . . .	10
2.2.1	Gauge Invariance Principle . . . . .	11
2.3	Quantum Electrodynamics . . . . .	13
2.3.1	Consequences of Gauge Invariance . . . . .	13
2.4	Quantum Chromodynamics . . . . .	15
2.4.1	Flavor Symmetry Breaking . . . . .	16
2.5	Running Coupling Constants . . . . .	17
2.6	Effective Field Theories . . . . .	20
<b>3</b>	<b>The Quark Model</b>	<b>21</b>
3.1	Quantum Numbers . . . . .	22
3.1.1	Isospin . . . . .	22
3.1.2	Hypercharge and Strangeness . . . . .	23
3.2	The Eightfold Way . . . . .	24

3.3	The Quark Model of Hadrons . . . . .	26
3.3.1	Baryons Multiplets . . . . .	28
3.3.2	Mesons Multiplets . . . . .	29
<b>4</b>	<b>The Charmonium Physics</b>	<b>31</b>
4.1	Heavy Quarkonia . . . . .	31
4.1.1	Spectral Notation . . . . .	32
4.1.2	Lagrangian for $c\bar{c}$ System . . . . .	33
4.2	Discovery of $J/\psi$ and $\psi(2S)$ Charmonia . . . . .	35
4.3	Charmonium Spectroscopy . . . . .	37
4.4	Transitions . . . . .	41
4.4.1	Radiative Transitions . . . . .	41
4.4.2	Hadron Transitions . . . . .	42
4.5	OZI Rule . . . . .	42
4.6	$\rho\pi$ Puzzle . . . . .	44
<b>5</b>	<b>BES-III Experiment</b>	<b>46</b>
5.1	Fixed Target Accelerators Versus Colliders . . . . .	46
5.2	Electron-Positron Colliders . . . . .	47
5.3	BEPCII Collider . . . . .	49
5.4	BEPCII Detector . . . . .	50
5.5	Physics Goals of BEPCII/BESIII . . . . .	55
<b>6</b>	<b>Analysis Results</b>	<b>57</b>
6.1	Introduction . . . . .	57
6.2	Data Set and Software Framework . . . . .	59
6.3	Analysis of $J/\psi \rightarrow \Xi^0(1530)\bar{\Xi}^0(1530)$ . . . . .	59
6.3.1	Initial Event Selection . . . . .	59
6.3.2	Final Event Selection . . . . .	62

6.3.3	Background Analysis . . . . .	64
6.3.4	Determination of Branching Fraction . . . . .	67
6.3.5	Systematic Error Analysis . . . . .	68
6.4	Analysis of $\psi(2S) \rightarrow \Xi^0(1530)\bar{\Xi}^0(1530)$ . . . . .	72
6.4.1	Initial Event Selection . . . . .	72
6.4.2	Final Event Selection . . . . .	73
6.4.3	Background Analysis . . . . .	78
6.4.4	Determination of Branching Fraction . . . . .	88
6.4.5	Systematic Error Analysis . . . . .	90
<b>7</b>	<b>Summary and Conclusion</b>	<b>94</b>

# Chapter 1

## Introduction

The November revolution that started with the discovery of  $J/\psi$  and  $\psi(2S)$  particles is still in its full swing. This has not only paved the way of experimental discoveries of many new particles, but also helped to develop the quark model and to understand Quantum ChromoDynamics (QCD), the theory of strong interaction. Both  $J/\psi$  and  $\psi(2S)$  are bound states of charm quark and charm antiquark pair and belong to charmonium family. Now charmonium has become an innovative tool to study the complicated nature of strong force both in perturbative as well as in non-perturbative region. In order to understand strong force, charmonium has played the same role as hydrogen atom has played in the understanding of electromagnetic force. The discovery has been helpful in encouraging new trends in technology of accelerators and detectors which has shifted from conventional fixed target accelerators to more useful colliders.

After the discovery of  $J/\psi$  and  $\psi(2S)$  by SPEAR  $e^-e^+$  collider at SLAC in 1974, the significant role of  $e^-e^+$  colliders have been fully realized and applied to study light hadron spectroscopy and charmonium physics. BESIII (Beijing Spectrometer III), operating at Institute of High Energy Physics Beijing China, is the world leading charmonium factory aiming at investigating many crucial aspects of Standard Model of particle physics with high precision in the  $\tau$ -charm region. BEPCII (Beijing Electron Positron Collider II) is

a double ring  $e^-e^+$  collider with design luminosity of  $10^{33}cm^{-2}s^{-1}$  and energy range of 2-5 GeV. We have analyzed BESIII experimental data for the search of  $(J/\psi, \psi(2S) \rightarrow \Xi^0(1530)\bar{\Xi}^0(1530)$  decay channels. The measured branching ratios are:

$$Br^{1C}[J/\psi \rightarrow \Xi^0(1530)\bar{\Xi}^0(1530)] = (1.06 \pm 0.07_{sys} \pm 0.37_{stat}) \times 10^{-5}$$

$$Br^{4C}[J/\psi \rightarrow \Xi^0(1530)\bar{\Xi}^0(1530)] = (2.94 \pm 0.06_{sys} \pm 1.10_{stat}) \times 10^{-5}.$$

$$Br^{1C}[\psi(2S) \rightarrow \Xi^0(1530)\bar{\Xi}^0(1530)] = (1.16 \pm 0.77_{sys} \pm 0.07_{stat}) \times 10^{-6}$$

$$Br^{4C}[\psi(2S) \rightarrow \Xi^0(1530)\bar{\Xi}^0(1530)] = (5.16 \pm 1.92_{sys} \pm 0.17_{stat}) \times 10^{-6}.$$

The 4C and 1C results are consistent within  $2\sigma$ . The test results of the 12 % rule are:

$$\frac{Br^{1C}(\psi(2S) \rightarrow B\bar{B})}{Br^{1C}(J/\psi) \rightarrow B\bar{B}} \approx 11\%$$

$$\frac{Br^{4C}(\psi(2S) \rightarrow B\bar{B})}{Br^{4C}(J/\psi) \rightarrow B\bar{B}} \approx 17.55\%$$

The thesis is composed as follows:

## **Chapter 2: The Standard Model**

The Standard Model of particle physics is the most successful theory of matter summarizing elegantly the constituents of matter and their interactions. In this chapter a brief review of fundamental particles and their interactions has been presented. Classification of fundamental particles and their interactions is presented. Chapter also includes a brief overview of quantum field theories.

## **Chapter 3: The Quark Model**

The Quark Model nicely presents a simple picture of hadrons, the strongly interacting particles. According to the quark model, hadrons are composed of fundamental particles called quarks. This chapter introduces briefly the development of the quark model and classification of particles that emerge from the quark model.

## **Chapter 4: The Charmonium Physics**

Discovery of charm quark not only proved to be a convincing evidence in the favor of quark model, it also opened up new doors to understand strong force in more better way.

Physics of charmonium and charmed mesons systems have become innovative experimental and theoretical tools to further investigate many aspects of strong force. This chapter is an overview of the basic concepts and information of charmonium physics. We briefly describe the importance of heavy quarkonium and charmonium systems, spectral notation, Lagrangian of charmonium, discovery of charmonium, charmonium spectrum, OZI rule and  $\rho\pi$  puzzle.

### **Chapter 5: BESIII Experiment**

In this chapter, we present the pros and cons of Beijing Spectrometer III (BESIII) and Beijing Electron Positron Collider II (BEPCII). Chapter opens with brief comparison of colliders over fixed target machines and the significant role of  $e^-e^+$  colliders. The design and working of BEPCII and BESIII with their physics goals is presented at the end.

### **Chapter 6: Analysis Results**

We have estimated the branching ratios of two decay channels  $(J/\psi, \psi(2S)) \rightarrow \Xi^0(1530)\bar{\Xi}^0(1530)$ , for the first time. This chapter presents the details of this analysis work.

### **Chapter 7: Summary and Conclusion**

This chapter summarizes the analysis work with some concluding remarks.

# Chapter 2

## The Standard Model

Man has always been curious to explore the laws of nature governing the universe and put them in a more consistent and simpler form. His continuous endeavors eventually unfolded two crucial aspects about the universe; fundamental particles and their interactions. The best theory which describes the fundamental particles and their interactions is called the Standard Model of Particle Physics. Originally it was proposed by Glashow, Salam and Weinberg as Electroweak Theory [1] in which the electromagnetic and weak interactions were unified. It was fully accepted after Veltman and G. 't Hooft [2] proved that the theory was renormalizable. Currently it includes strong interaction on an adhoc basis. Establishment of the Standard Model is one of the greatest achievements in the history of physics. It has incredibly explained almost all observed particle physics phenomena and is further being tested by highly sophisticated experiments.

### 2.1 Components of the Standard Model

The Standard Model of Particle Physics provides an excellent theoretical framework to investigate the fundamental physics issues of the universe. In this regard, a rigorous mathematical approach is available in Refs. [3, 4, 5]. This section will provide information about basic components of the Standard Model. Discussion will be focussed on types of

fundamental particles and their interactions.

### 2.1.1 Fundamental Particles

Greek philosopher Democritus put forward the idea of atom meaning “indivisible”. Until the beginning of 20th century, atom was considered to be the fundamental building block of matter. With the discovery of electron by J. J. Thomson in 1897 followed by the discovery of proton in the famous Rutherford’s alpha scattering experiment in 1911 and the discovery of neutron by Chadwick in 1932, totally discarded the conviction about atom being a fundamental particle of matter. Afterwards Dirac introduced the concept of antiparticles such as positron (an antiparticle of electron) [3, 6]. Now we know that protons and neutrons are composite systems while electron is fundamental particle without any internal structure up to a scale of  $10^{-16}\text{cm}$  [7] . On the basis of spin fundamental particles are divided into two groups; the fermions and bosons. These groups of particles are highlighted as follows.

#### Fermions

Fermions are particles with half integral spin and thus obey Fermi-Dirac statistics. They are integral part of matter and are also called matter particles <sup>1</sup>. At fundamental level, fermions which do not experience strong interaction are called leptons (e.g. electron, neutrino etc.), and fermions which feel strong interaction are called quarks. Quarks exist in six flavors : up, down, strange, charm, bottom and top. One distinct feature of quarks is that they carry fractional electric charge. Quarks also carry color charge which is thought to be origin of strong interaction. There are three flavors of color charge; red, green and blue. According to our current knowledge, there are three generations of quarks and

---

<sup>1</sup>Nucleons are also fermions but they are composite and are bound states of three quarks.

leptons <sup>2</sup> as shown in Table 2.1. The ordinary matter consists of three types of fermions, namely; up quark, down quark and electron, belonging to the first generation. Fermions of different generations differ regarding their masses. Fermions of second and third generation are more massive and may decay to the particles of first generation [3, 5, 8].

	Name		Mass [GeV/ $c^2$ ]	Electric charge	Generation
Quarks:	$u$	up	$\sim 0.0015 - 0.004$	+2/3	I
	$d$	down	$\sim 0.004 - 0.008$	-1/3	I
	$c$	charm	$\sim 1.15 - 1.35$	+2/3	II
	$s$	strange	$\sim 0.08 - 0.13$	-1/3	II
	$t$	top	174.3	+2/3	III
	$b$	bottom	$\sim 4.1 - 4.4$	-1/3	III
Leptons:	$\nu_e$	el. neutrino		0	I
	$e$	electron	$5.1 \times 10^{-4}$	-1	I
	$\nu_\mu$	muon neutrino		0	II
	$\mu$	muon	0.11	-1	II
	$\nu_\tau$	tau neutrino		0	III
	$\tau$	tau	1.8	-1	III

Table 2.1: Fundamental particles [8]

## Bosons

Bosons consist of special class of particles called gauge bosons which act as mediators of the fundamental interactions. They are integral spin particles and obey Bose-Einstein statistics. The gauge bosons corresponding to each interaction are shown in Table 2.2. It is assumed that mass is not an intrinsic property of matter, rather particles attain mass when they interact with the Higgs field through ‘Brout-Englert-Higgs Mechanism’ or simply Higgs mechanism [9]. For a rigorous discussion of different modes of Higgs

<sup>2</sup>Corresponding to each particle there exists an antiparticle having same quantum numbers as that of particle except the additive quantum numbers like lepton number, baryon number, charge etc.

mechanism and spontaneous symmetry breaking see Ref. [4]. After the discovery of new heavy Boson, which is likely to be the most wanted missing Higgs Boson, by ATLAS and CMS groups at CERN the Standard Model might be completed. The mass of newly discovered Boson measured by CMS is  $(125.3 \pm 0.4_{stat} \pm 0.5_{sys}) GeV/c^2$  with significance level of  $5.0 \sigma$ , while measured by ATLAS is  $(126.00 \pm 0.4_{stat} \pm 0.4_{sys}) GeV/c^2$  with  $5.9\sigma$  [10]. Its true nature will be further investigated through its production and decay modes and other properties.

### 2.1.2 Fundamental Interactions

With the growing number of elementary particles, physicists realized that all of them could be classified according to their relationship with the fundamental forces of nature [6]. Study of fundamental forces has been a very exciting domain of physics for centuries, and dates back to Newton who formulated his famous gravitational law describing gravity as the force of attraction between two bodies. Coulomb's law was another important breakthrough which established the empirical relation of electric force existing between charge particles. Faraday gave the idea of magnetic force arising from the current. Currently we have four fundamental forces of nature which are briefly described in the following section:

- **gravitational force:** Newton described gravity as the attractive force between massive objects. Einstein gave a geometrical interpretation of gravity in his theory of General Relativity and linked it with the curvature of space-time. The coupling constant  $G_N$  of gravity is the weakest of the four couplings. All gravitational charges are of the same sign and the gauge bosons of gravity (gravitons, not found yet) are massless, hence the range of gravity is infinite. Gravity dominates at large scale (planets, galaxies, universe, . . . ), but loses its power at small scale. Owing to these features gravity is not included in standard model [11].
- **electromagnetic force:** Coulomb discovered electric force between electric charges.

Experiments carried out by Oersted, Ampere and Faraday established the idea of magnetic force arising from the current. Maxwell unified electric and magnetic forces into a single force and proved that they are just the two facets of a single force called electromagnetic force. Range of this force is also infinite due to its massless gauge boson i.e. photon. Electrons revolve round the nucleus of atoms through electromagnetic force. In the absence of this force stability of atom might have been in doll drum. There could be no hydrogen and oxygen atoms, and there could be no traces of life on earth in the absence of water. Atoms combine together to make molecules and molecules in turn make living and non-living things; and all this is possible only through electromagnetic force.

- **strong force:** Strong nuclear force binds protons and neutrons inside the nucleus and is the residual force arising from the strong force existing between quarks and gluons. Thus electromagnetic force and strong force provide us with more than hundred stable elements. Strong nuclear force has short range of order of one fermi (fermi =  $10^{-15}m$ ) despite the fact its gauge bosons which are eight gluons are massless. [3, 11]
- **weak force:** Weak force is responsible for the nuclear  $\beta$ -decay [3, 5, 11]. It is also known to control the burning rate of the sun and to play a decisive role in the explosion of type II supernovae [12]. Contrary to other forces, the weak force does not make any bound state. For example, the strong force is responsible for the bound states of nucleons; the electromagnetic force binds many atoms and molecules together; while the gravity binds together objects on an astronomical scale [13]. Weak force is also of short range of the order of  $10^{-18}m$  [6] as its carriers are massive which are  $W^{\pm}, Z^0$  bosons.

Four fundamental forces of nature are shown in Table 2.2 along with their ranges and force carriers.

Force	Name	Mass [GeV/c <sup>2</sup> ]	Range [fm]	Timescale [s]
Strong force	$g$ gluon	0	$\sim 1$	$\sim 10^{-22} - 10^{-24}$
Electromagnetic force	$\gamma$ gamma	0	Infinite	$\sim 10^{-16} - 10^{-21}$
Weak force	$Z^0$ Z boson	$91.1876 \pm 0.0021$	$\sim 10^{-3}$	$\sim 10^{-7} - 10^{-13}$
	$W^\pm$ W boson	$80.403 \pm 0.029$	$\sim 10^{-3}$	$\sim 10^{-7} - 10^{-13}$

Table 2.2: Fundamental forces [8]

### 2.1.3 Range of Interactions

Instead of force, which is usually considered a push or pull, a more appropriate term “interaction” is used by particle physicists [6]. The usual connotation of force is not appropriate while discussing the production of photons resulting from atomic and nuclear transition (electromagnetic process), production of electron and neutrino in nuclear beta decay (weak process), and the production of pions from the energetic collision of protons (strong process). The interactions among the fundamental particles and their bound states take place via exchange of intermediate particles called gauge bosons: particles with integer spin. Feynman devised a fruitful pictorial scheme, called Feynman diagram, to represent the fundamental interactions as shown in Fig. 2.1 [3, 6, 14].

Range of interactions is determined by the mass of gauge bosons involving in the respective interaction. The same can be elaborated by uncertainty principle defined by

$$\Delta x \Delta p \approx \hbar \quad (2.1)$$

or

$$\Delta x \approx \hbar / \Delta p \quad (2.2)$$

Hence the range of interaction is inversely proportional to the mass of the gauge bosons. In the case of electromagnetic interaction we have massless photon and hence the range

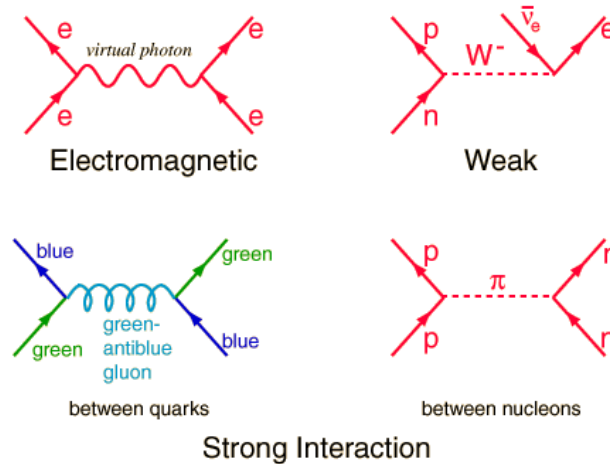


Figure 2.1: Feynman diagrams depicting the three fundamental interactions [15]

of electromagnetic interaction is infinite. On the other hand the masses of weak gauge bosons  $W^\pm$  and  $Z^0$  are  $80 \text{ GeV}/c^2$  and  $91.6 \text{ GeV}/c^2$  respectively, which is reason for the short range of the weak interaction. The same scheme does not hold for strong interaction which depicts short range characteristics despite the fact that the quanta of strong force (gluons) are massless.

For more precise description of fundamental interactions, physicists have formulated a set of theories called quantum field theories. Instead of point-like objects, quantum field theories describe fundamental particles as extended objects in terms of fields. This description is consistent both with Einstein's Special Theory of Relativity and quantum mechanics (wave mechanics) [16]. In the following section we present a brief overview of quantum field theories.

## 2.2 Quantum Field Theories

Famous Coulomb's electrostatic law and Newton's law of gravity are example of action at a distance which are not in harmony with the special theory of relativity. In order to remove this inconsistency, idea of field as an intervening medium between the objects was devised

by Einstein and Faraday. Faraday's law and Maxwell's four equations incorporated the idea of fields. Though Maxwell's equations fulfil the requirements of field theories and are in accordance with theory of relativity but they are not consistent with quantum mechanics. For instance they could not explain the non-zero value of vacuum field that appears in QED which is the quantized version of electromagnetic interaction [6]. Also quantum mechanics alone could not offer any explanation to the non-conservation of particles in any reaction which is allowed by Einstein mass energy relationship. For instance, Schrodinger equation in QM is single particle equation, which is not consistent with special theory of relativity (STR). Embedding quantum mechanics with relativity emerged as a new field of quantum field theories and the Klein-Gordan and the Dirac equations as many body field equations nicely explain the interactions of bosons and fermions respectively. [4].

The generic name for quantum field theories of the Standard Model is the "gauge theories". According to gauge theories, fermions interact with each other by forces which couple them to bosons mediating the forces. Apart from gravitons, the existence of other bosons have been experimentally verified. The fate of gravitation interaction as a local gauge theory is yet to be established [4, 17]. The Lagrangian of mediating bosons for each gauge theory is invariant under a local gauge transformation, so these mediating bosons are referred to as gauge bosons.

### **2.2.1 Gauge Invariance Principle**

The principle of gauge invariance plays crucial role in describing theories of the Standard Model of particle physics. Originally, Vladimir Fock extended the principle of gauge principle in classical electrodynamics to the quantum mechanics. (For comprehensive review of historical development and implications of gauge principle see Ref. [18]). Gauge invariance is an essential characteristics of all quantum field theories such that Lagrangian remains invariant under a certain symmetry transformation called gauge transformation. Firstly it was established in classical electrodynamics, where invariance of Maxwell's equations

under transformation of vector potential  $A$  and scalar field  $\phi$  preserve the electric field  $E$  and magnetic field  $B$  [3, 4, 5] defined as

$$B = \nabla \times A, E = -\nabla\phi - \frac{\partial A}{\partial t} \quad (2.3)$$

The transformations of  $A$  and  $\phi$  that preserve  $B$  and  $E$ , and hence the Maxwell equations are given as below

$$A \rightarrow A' = A + \nabla\chi, \phi \rightarrow \phi' = \phi - \frac{\partial\chi}{\partial t} \quad (2.4)$$

where  $\chi$  is an arbitrary scalar function.

If we define 4-vector potential as  $A^\mu = (\phi, A)$ , then gauge transformation in compact form will be  $A^\mu \rightarrow A'^\mu = A^\mu - \partial^\mu\chi$ .

Now we see the behavior of Lagrangian density of vector field under the above gauge transformation. For a massive gauge vector field  $A^\mu$ , field Lagrangian density is

$$L = -\frac{1}{4}F_{\mu\nu}F^{\mu\nu} + \frac{1}{2}m^2 A^\mu A_\mu \quad (2.5)$$

Now the anti symmetric second-rank field strength tensor  $F^{\mu\nu} = \partial^\mu A^\nu - \partial^\nu A^\mu$  remains invariant under the gauge transformation  $A^\mu \rightarrow A'^\mu = A^\mu - \partial^\mu\chi$ , while the mass term does not. Therefore, to keep the Lagrangian of Maxwell theory invariant the mass term must be zero i.e.  $\frac{1}{2}m^2 A^\mu A_\mu = 0$ . It implies  $m = 0$ , hence the quanta of gauge field i.e. photon is massless and the range of electromagnetic interaction is accordingly infinite [3, 4, 5].

Quantum field theories like quantum electrodynamics and quantum chromodynamics respect gauge principle and hence are called gauge theories and are discussed in the following sections.

## 2.3 Quantum Electrodynamics

Quantum electrodynamics (QED) is the quantum field theory of electromagnetic interaction. It is one of the simplest and most successful gauge theories agreeing nicely with experiments and has a huge power of predictability. For detail about development and full mathematical treatment of QED, see Refs. [3, 4, 5, 19]. QED describes the interactions of charged fermions (such as the electron) that are coupled to gauge field of SU(1) group. The quantum of SU(1) gauge field is massless photon which does not show self interaction, and hence QED is Abelian in nature. Lagrangian density for free Dirac particle in QED is given by [3]

$$\mathbb{L}_0 = \bar{\psi}(x)(i\gamma^\mu \partial_\mu - m)\psi(x) \quad (2.6)$$

where  $\gamma^\mu$  are the Dirac matrices obeying the anti-commutation relation  $[\gamma^\mu, \gamma^\nu] = 2g^{\mu\nu}$ , the derivative is  $\partial_\mu = \frac{\partial}{\partial x^\mu}$ , and  $m$  is the fermion mass, and adjoint of  $\psi$  is  $\bar{\psi} = \psi^\dagger \gamma^0$ . Dirac equation for a free particle corresponding to the above Lagrangian density is given as

$$(i\gamma^\mu \partial_\mu - m)\psi(x) = 0 \quad (2.7)$$

Lagrangian density,  $\mathbb{L}_0$ , for the non-interacting QED remains invariant under the global phase rotation of the fermion field. In order to make Lagrangian density invariant under local gauge transformation of the fermionic field:  $\psi \rightarrow \psi' = e^{i\chi(x)}\psi$ , we replace the ordinary derivative  $\partial_\mu$  with a covariant derivative  $D_\mu = \partial_\mu + ieA_\mu$ . Where  $A_\mu$  is the gauge(vector) field. Hence the new Lagrangian density becomes

$$\mathbb{L}(x) = \bar{\psi}(x)[i\gamma^\mu(\partial_\mu + ieA_\mu) - m]\psi(x) \quad (2.8)$$

### 2.3.1 Consequences of Gauge Invariance

Comparing Eqs. 2.6 and 2.8, the term

$$\mathbf{L}_{int} = -e\bar{\psi}(x)\gamma^\mu A_\mu(x)\psi(x) \quad (2.9)$$

describes the interaction of the lepton and photon fields [4].

Hence, the invariance of the theory implies the coupling of fermion field  $\psi$  with the gauge field  $A_\mu$  (photon field in this case). As a matter of factuality, no free electron exists in nature rather it interacts with the localized gauge field. Hence any physical theory must be locally gauge invariant. Thus,

- The local gauge invariance of the Lagrangian density results into a new massless vector field (the photon field) revealing through the vector potential  $A_\mu$ .
- Dynamical effects in the theory are also produced by making the theory local gauge invariance: it specifies the nature of the interaction between the fermionic field and the vector gauge field  $A_\mu$

Imposing the condition of local gauge invariance is called gauging the symmetry and is one of the important tools in quantum field theories. In QED, vector fields  $A_\mu$  for vector gauge bosons (photons) are neutral and hence there is no self interaction of gauge fields which makes QED Abelian gauge theory. Theories containing the feature of local gauge invariance are renormalized theories [4].

The presence of vector field in the Lagrangian  $\mathbf{L}(x)$  also demands the presence of kinetic term and mass term [3, 4, 5]. However, the mass term spoils the invariance of the Lagrangian, and hence is not included. The required kinetic term is  $-\frac{1}{4}F_{\mu\nu}F^{\mu\nu}$ . Therefore, full QED Lagrangian density is given by

$$\mathbf{L}_{QED} = \bar{\psi}(x)[i\gamma^\mu(\partial_\mu + ieA_\mu) - m]\psi(x) - \frac{1}{4}F_{\mu\nu}F^{\mu\nu} \quad (2.10)$$

Hence the local gauge invariance of the Lagrangian results into the interacting theory of quantum electrodynamics.

## 2.4 Quantum Chromodynamics

Quantum chromodynamics (QCD) is a quantum field theory of strong interaction that describes quarks and their interactions [20, 21]. In QCD, the quarks are described by Dirac spinors and are coupled to bosonic gauge fields of SU(3) group. The quanta of gauge fields are massless spin-one particles called gluons with additional degree of freedom called color. Owing to this, there is self interaction among the gluons which makes QCD a non-Abelian gauge theory. For an early theoretical review of QCD see Ref. [22]; for the experimental review see Refs. [23, 24]. Now we intend to obtain the Lagrangian density for non-Abelian SU(3) gauge group under the local gauge transformation  $\psi \rightarrow \psi' = e^{i\alpha_a(x)T_a}\psi$ . Where  $T_a$  with  $a=1,\dots,8$  are generators of SU(3). The conventional choice of  $T_a$  is set of 8 linearly independent traceless  $3 \times 3$  hermitian  $\lambda_a$  matrices such that [3, 27]

$$[T_a, T_b] = if_{abc}T_c \quad (2.11)$$

where  $f_{abc}$  are structure constants of Lie Algebra. Now the lagrangian density for free quarks color fields is

$$\mathbb{L}_{quarks} = \sum_f \bar{\psi}_f(x)(i\gamma^\mu \partial_\mu - m_f)\psi_f(x) \quad (2.12)$$

where  $f=1,2,3$  for three color fields of quarks. Now the above Lagrangian density is not invariant under local gauge transformation. In order to restore the invariance of the Lagrangian density we replace the ordinary derivative with the covariant derivative of the form

$$D_\mu = \partial_\mu + igT_a G_\mu^a \quad (2.13)$$

where  $g$  is strong coupling constant.  $G_\mu^a (a = 1, 2, \dots, 8)$  for eight gauge fields of vector gauge bosons of strong interaction transforming as  $G_\mu^a \rightarrow G_\mu^a - 1/g\partial_\mu\alpha_a - f_{abc}\alpha_b G_\mu^c$ . Now under the replacement  $\partial_\mu \rightarrow D_\mu$ , we get

$$\mathbb{L}'_{quarks} = \bar{\psi}(i\gamma^\mu\partial_\mu - m)\psi - g(\bar{\psi}\gamma^\mu T_a\psi)G_\mu^a \quad (2.14)$$

After adding the kinetic term for the gauge fields  $G_\mu^a$ , the gauge invariant Lagrangian density for QCD is given by

$$\mathbb{L}_{QCD} = \bar{\psi}(i\gamma^\mu\partial_\mu - m)\psi - g(\bar{\psi}\gamma^\mu T_a\psi)G_\mu^a - 1/4G_{\mu\nu}^a G_a^{\mu\nu} \quad (2.15)$$

where the field tensor  $G_{\mu\nu}^a$  is

$$G_{\mu\nu}^a = \partial_\mu G_\nu^a - \partial_\nu G_\mu^a - gf_{abc}G_\mu^b G_\nu^c. \quad (2.16)$$

### 2.4.1 Flavor Symmetry Breaking

Lagrangian density in Eq. 2.14 represents the interaction of three colors of a particular flavor of a quark with eight gluons. The eight color currents  $j_a^\mu = (-)g\bar{\psi}\gamma^\mu T_a\psi$  act as the sources of color fields  $G_\mu^a$  in the same manner as the electric currents act as the source of electromagnetic field. Actually, there would be six such Lagrangian densities, one for each of the six flavors of quarks.  $L_{QCD}$  does not include the mass term corresponding to the gauge fields  $G_\mu^a$  and is gauge invariant. Therefore, the quanta of gauge fields of QCD (gluons) are massless. In the case of QCD, gauge vector fields  $G_\mu^a$  carry color which causes self interaction among the gauge fields and hence QCD is non-Abelian in nature.

In Eq. 2.11, only a single gauge coupling constant  $g$  describes the gluons coupled to the quark flavors, which means the flavor symmetry breaking in the QCD Lagrangian is due to unequal masses  $m_f$  for different flavors of quarks [4].

It is pertinent to mention that QED and QCD are, in fact, low energy effective field theories and their famous renormalizable character drastically spoils at extremely high energy such as the Planck energy. At the Planck scale, gravity becomes too strong to be neglected which is usually assumed [4, 5, 16]. The strengths of QCD and QED at different

energy scales can be described in terms of constants termed as the running coupling constants as discussed in the following section.

## 2.5 Running Coupling Constants

Strength of any force can be described in terms of the coupling constant of the theory. The value of coupling constant at a particular energy gives the reaction rate in terms of the absorption or emission of the gauge bosons. For instance, in QED and QCD large coupling constant means more absorption or emission rate of photons and gluons respectively. These coupling constants cannot be measured directly, rather these can be obtained from a measured quantity, for instance cross section, decay rate etc [25]. In terms of momentum transfer  $q^2$  we have

$$\alpha(q^2) = \frac{\alpha(\mu^2)}{1 - \frac{\alpha(\mu^2)}{3\pi} \ln\left(\frac{q^2}{\mu^2}\right)} \quad (2.17)$$

where  $\mu^2$  is an arbitrary energy scale not to be fixed by QED. Hence, coupling constant  $\alpha$  increases with increase in momentum transfer. It can be explained on the basis of shielding of electric charge due to the vacuum polarization as shown in Fig. 2.2 [4, 26, 27]. In fact, around a field charge (electron) a charge of opposite polarity is developed by the vacuum polarization which in turn produces the screening effect seen by the test charge placed at large distance from the source charge. Experimentalists measure this effective electron charge rather a bare charge which is visible only at a very short distance. Actually, at a small distance the screening effect reduces and the test charge feels more charge thus increasing the reaction rate or the value of  $\alpha$  of QED [5].

If we consider only an  $e^+e^-$  loop, at low energy i.e low  $q^2$ ,  $q^2 \rightarrow \mu^2 \rightarrow 0$ ,  $\alpha(0) = 1/37$ , hence

$$\alpha(q^2) = \frac{\alpha(0)}{1 - \frac{\alpha(0)}{3\pi} \ln\left(\frac{q^2}{m^2}\right)} \quad (2.18)$$

However, at higher momentum transfer when more and more particle-antiparticle pairs are excited,  $\mu^+\mu^-, \tau^+\tau^-, u\bar{u}, d\bar{d}, \dots$  we get [5, 25]

$$\alpha(q^2) = \frac{\alpha(\mu^2)}{1 - z_f \frac{\alpha(\mu^2)}{3\pi} \ln(\frac{q^2}{\mu^2})} \quad (2.19)$$

where  $z_f$  is the sum of the squares of the fermion charges contributing at a particular value of  $q^2$ , practically with  $m \leq q^2$ .

Therefore, QED coupling constant is oftenly considered to be constant as its dependence on momentum transfer is very slow as shown in Fig. 2.2c [26].

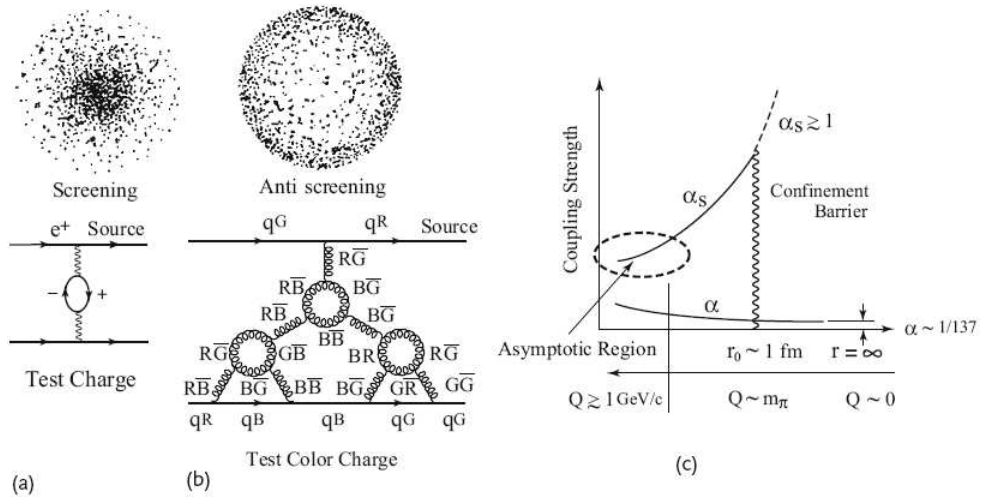


Figure 2.2: (a,b) Variation of coupling constants of QCD and QED due to screening and antiscreening effects. (a) The strength of QED  $\alpha$  decreases with separation of test charge from the source. (b) The strength of QCD  $\alpha_s$  increases with the separation of test color charge (another quark) due to the antiscreening effect of gluon self-coupling (c)  $\alpha$  is finite at  $r \rightarrow \infty (q^2 = 0)$  and increases at shorter distances due to weak screening.  $\alpha_s$  is meaningless at large distances  $\geq 10^{-13}$  cm because of confinement and is small at short distances. [26]

For instance, at high momentum transfer of the order of the masses of intermediate weak bosons, QED running coupling constant involving all known lepton and quark loops is [4]  $\alpha(q^2 = (90 \text{ GeV})^2) \simeq 1/30$ .

Due to small value of  $\alpha$ , calculations in QED can be carried out using the idea of perturbative techniques. According to perturbative scheme, any physical quantity can be written as a sum of increasing power of the coupling of the theory.

In QCD, the expression for running coupling in momentum space is [3, 4, 5, 26]:

$$\alpha_s(q^2) = \frac{\alpha_s(\mu^2)}{1 + \frac{\alpha_s(\mu^2)}{4\pi} (11 - \frac{2}{3}n_f)\log(q^2/\mu^2)} = \frac{12\pi}{(33 - 2n_f)\log(\frac{q^2}{\Lambda_{QCD}})} \quad (2.20)$$

where  $n_f$  is the number of quark flavors involved in the loop diagram under consideration and  $\Lambda_{QCD}$  is QCD scale parameter to be determined experimentally.

Form the above expression, we see that  $\alpha_s$  approaches zero as  $q^2 \rightarrow \infty$ . This is called asymptotic freedom where quarks behave as free particles. This is due to antiscreening effect of gluons as shown in fig.2.2b. The vacuum polarization effect due to physical fermions and gluons causes screening effect, but the effect of the unphysical gluon loop is opposite and is the cause of antiscreening. Discovery of asymptotic freedom by Politzer, Gross and Wilczek in 1973 [28] was a crucial break through in QCD and paved the way to use perturbation theory in QCD at large  $q^2$  (phenomenologically at  $q \leq 1\text{GeV}/c$ ) and the parton model, which take quarks as point particles [26]. Asymptotic freedom can also explain the formation of quarkonium and the famous OZI rule [5].

In physics, we encounter many situations which involve two quite separate scales: the light and the heavy. If energy-momentum is smaller than the heavy scale, the interaction can be represented by an effective Hamiltonian, containing only light degrees of freedom but which fully accommodates all (virtual) effects of the heavy scale. Such an interaction can effectively isolate and describe the underlying physics of a particular phenomena rather than a rigorous treatment of the entire system [29]. In the following section we describe theories called effective field theories which contain the above mentioned features.

## 2.6 Effective Field Theories

Properties of hadrons can be described by QCD Lagrangian in terms of the quark masses  $m$  and the coupling constant  $\alpha_s$ . At low energy scale of leading order QCD (LQCD), non-perturbative effects become prominent and  $\alpha_s$  becomes large. The non-perturbative QCD (nPQCD) dynamics originates from the confinement of quarks inside hadrons. At such scale, systems are described either by phenomenological potential models and constituent quark-model, or by first principles lattice simulations. However, the physics of systems containing a heavy quark  $q$  can be simplified. For systems containing heavy quarks, the quark-mass scale  $m_q$  becomes larger than LQCD which means  $\Lambda_{QCD}$  is small which allows the use of perturbative expansion at this scale [29].

Non-relativistic bound states comprising heavy quarks are represented by a hierarchy of energy scales ordered by the quark velocity  $v \ll 1$ : the quark mass  $m$  (hard scale), the relative momentum of heavy quark antiquark  $mv$  (soft scale), the typical kinetic energy of the heavy quark  $mv^2$  i.e. the quark binding energy in the bound state (ultrasoft scale), where  $m$  is the heavy-quark mass and  $v$  is its velocity in the CM frame. Such hierarchy of scales are advantageous to introduce non-relativistic effective field theories (NR EFTs) for the description of two particle non-relativistic bound states containing heavy quarks i.e. heavy quarkonia [29, 30, 31, 32, 33].

Annihilation and production of quarkonium system occur at the quark mass scale  $m$ , called the hard scale. An effective field theory obtained from QCD by integrating the hard scale is named as non-relativistic QCD (NRQCD) [33, 34]. Formation of quarkonium occurs at the quark momentum scale  $mv$ , called the soft scale. The suitable EFT obtained from NRQCD by integrating out the soft scale i.e.  $mv \sim r^{-1}$  is named as potential NRQCD (pNRQCD) [33, 34]. Depending upon the radius of the quarkonium system, the scale  $mv$  may or may not be larger than the QCD confinement scale  $\Lambda_{QCD}$  [33].

# Chapter 3

## The Quark Model

In order to classify large number of subatomic particles in simple fashion, Gell-Mann [35] and Zweig [36] independently put forth the idea of quark in 1964. According to them, all known hadrons were composed of more fundamental entities called quarks. Initially quarks were not accepted as physical objects owing to their strange nature; they carried fractional electric charge, also no isolated quark is ever found. Hence quark concept could not get any big success at that time. The first evidence that confirmed the reality of quark as physical object, came from series of deep inelastic e-p scattering experiments carried out at SLAC in the early 1970's [37]. These experiments revealed point-like structures inside proton, called the partons by Feynman [38]. At high energy, the parton model describes the hadron as a composition of small constituents-the partons. Partons were naturally identified with quark and gluon degrees of freedom described by QCD [39]. However, the discovery of charm quark in terms of  $J/\psi$  and  $\psi(2S)$  states (each being bound state of charm-anticharm quark pair, called charmonium), proved to be even more convincing evidence in the favor of quark model. The quark model got much sophistication due to the work of Nathan Isgur and Gabriel Karl [40], who established that all of the low energy hadronic systems could be understood as bound states of quarks [5]. We discuss the ideas and information related to quark model, in the following sections.

## 3.1 Quantum Numbers

In this section, we will discuss quantum numbers which form the basis of classification of hadrons such as Gell-Mann's Eightfold scheme and the quark model.

### 3.1.1 Isospin

The idea of isospin was given by Heisenberg [5, 41] by considering proton and neutron as two different states of one particle called the nucleon. Nucleon has isospin of  $I=1/2$ ; therefore, there are  $(2I+1=2)$  isospin states for nucleon, called doublet comprising proton and neutron. Each state is distinguished with the third component of isospin  $I_3$ , which is  $1/2$  for proton and  $-1/2$  for neutron. For proton and neutron, the isospin states are defined by

$$|p\rangle = \begin{pmatrix} 1 \\ 0 \end{pmatrix} = |1/2, 1/2\rangle, \quad |n\rangle = \begin{pmatrix} 0 \\ 1 \end{pmatrix} = |1/2, -1/2\rangle \quad (3.1)$$

Like spin triplet and spin singlet, we can join two  $I=1/2$  states to form either an isospin triplet  $(|p\rangle|p\rangle, \frac{1}{\sqrt{2}}(|p\rangle|n\rangle + |n\rangle|p\rangle), |n\rangle|n\rangle)$  with  $I=1$  and  $I_3=1, 0, -1$ , or an isospin singlet  $(\frac{1}{\sqrt{2}}(|p\rangle|n\rangle - |n\rangle|p\rangle))$  with  $I=0$  and  $I_3=0$  [5].

Isospin invariance implies that the isospin operator  $\mathbf{J}$  commutes with the Hamiltonian  $H_n$  of the nuclear force  $[H_n, \mathbf{J}] = 0$ . The inclusion of electromagnetism destroys this invariance  $[H_n + H_{em}, \mathbf{J}] \neq 0$ . Since charge is conserved, the charge operator must commute with the total Hamiltonian  $[H_n + H_{em}, Q = 0] \implies [H_n + H_{em}, J_3] = 0$ . This is true only when  $B$  is conserved which implies the conservation of the third component of isospin even in the presence of an electromagnetic interaction. Now the relationship between baryon number  $B$  and third component of isospin is [3, 5]:

$$Q = I_3 + \frac{B}{2} \quad (3.2)$$

Each nucleon has  $B=1$ , while antinucleon has  $B=-1$ .

### 3.1.2 Hypercharge and Strangeness

Nuclear experiments performed at high energy observed some particles produced through strong interaction (conserving isospin) but decayed through weak interaction (violating isospin) [3, 5]:

$$\pi^- + p \rightarrow \begin{cases} \Sigma^- + K^+ \\ \Sigma^0 + K^0 \\ \Lambda^0 + K^0 \end{cases} \quad (3.3)$$

and

$$\Sigma^- \rightarrow n + \pi^-, \quad \Sigma^0 \rightarrow n + \pi^0.$$

Keeping in view the strange behavior of such particles, Gell-Mann and Nishijima proposed the following relation among their quantum numbers [3, 5, 42]:

$$Q = I_3 + \frac{1}{2}(B + S) = I_3 + \frac{Y}{2} \quad (3.4)$$

where  $Y$  is called hypercharge defined as  $Y=B+S$ .

By definition,  $K^+$  is assigned +1 strangeness and all pions and nucleons are associated with zero strangeness. With the discovery of new particles, isospin was assigned to them on the basis of simplicity and near-degeneracy of masses of different particles if they occurred. From the reaction 3.3, we observe that  $\Sigma^-$  has  $S=-1$ . Accordingly for  $K^+$ ,  $S = +1$  and for  $\Sigma^0$ ,  $S = +1$ . Consider an isospin-strangeness-conserving reaction  $K^-p \rightarrow \Lambda\pi^0$ . Clearly for  $\Lambda$ ,  $S = -1$ . Accordingly in reaction 3.3, for  $K^0$ ,  $S = +1$ . This creates a bit paradox - there are two Kaons,  $K^+$ , and  $K^0$ , with  $S = +1$ , but only one with  $S = -1$  i.e.  $K^-$ . Gell-Mann resolved this puzzle by suggesting that there should be an antiparticle  $\bar{K}^0$  with  $S = -1$  i.e.  $K^-$ . Soon, this particle was discovered in the reaction  $\pi^+p \rightarrow p\bar{K}^0\bar{K}^+$  [5].

Now we discuss Gell-Mann's *Eightfold Way* classification scheme in view of above mentioned quantum numbers.

## 3.2 The Eightfold Way

After the discovery of more particles the assignment of isospin and strangeness quantum numbers became chaotic. To make things simpler, Gell-Mann in 1961 devised an ordered pattern in the mass of so called elementary particles so as to arrange the particles in a symmetric fashion [14]. He arranged the *baryons*, and *mesons* into a geometrical pattern on the basis of their charge and strangeness. The pattern is known as the *Eightfold Way*, or technically SU(3) symmetry. In this method, the particles with same strangeness are placed on the same horizontal lines while the particles having same charge are placed on the same diagonal lines. The resultant hexagonal arrays are called the baryon and meson multiplets [14], as shown in Fig.3.1. and Fig. 3.2, respectively. The families of hadrons with different electric charge but having similar masses are called multiplets. For instance,  $\Delta$  is one of a quartet of particles,  $\Delta^{++}$ ,  $\Delta^+$ ,  $\Delta^0$  and  $\Delta^-$ , each having mass close to 1232 MeV/ $c^2$ . Other familiar examples are proton-neutron doublet, and the triplet comprising  $\pi^+$ ,  $\pi^0$  and  $\pi^-$  [6].

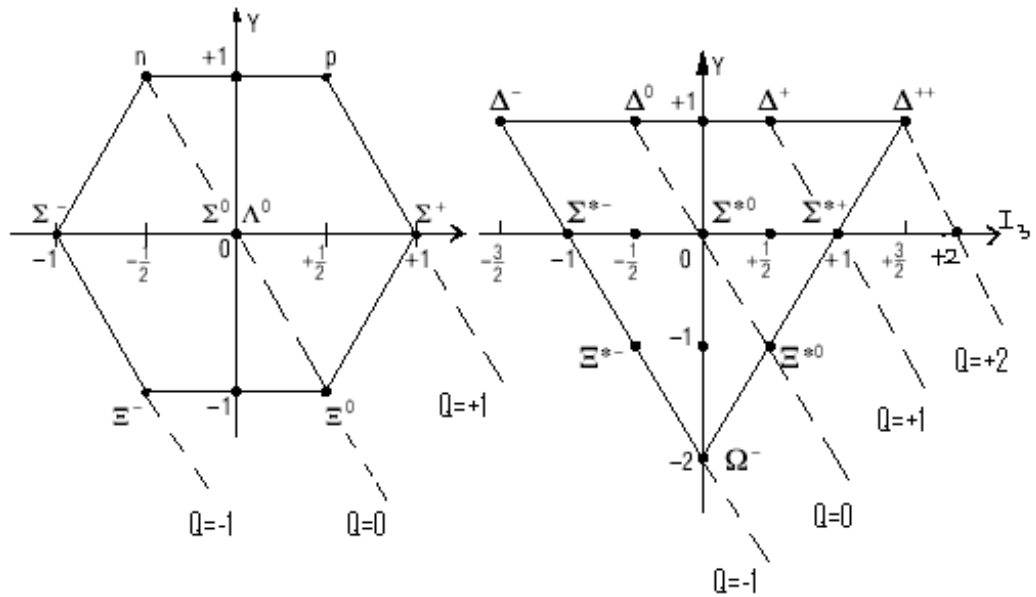


Figure 3.1: Baryon multiplets: Baryon octet or  $J^P = (1/2)^+$  SU(3) multiplets (left). Baryon decuplet or  $J^P = (3/2)^+$  SU(3) multiplets (right), where 1/2 stands for spin and + for even parity and so on [3, 5].

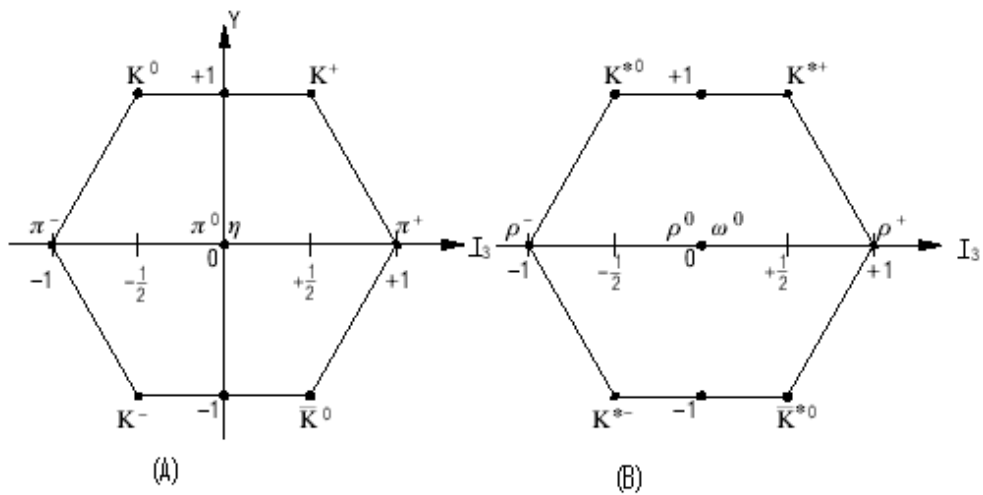


Figure 3.2: Meson Multiplets: (A) Pseudoscalar meson octet with  $J^P = 0^-$ . (B) Vector meson octet with  $J^P = 1^-$  [3, 5].

One particle shown in the Eightfold Way, having strangeness -3, and spin 3/2 was still missing. Gell-Mann called this particle the  $\Omega^-$ , meaning in Greek the last one,

and predicted it three years before its discovery [43]. It has also been seen at BESII in  $\psi(2S) \rightarrow \Omega^-\bar{\Omega}^+$  decay channel [44].

Success of the Eightfold Way itself raised a very crucial question: why do the hadrons fit into these patterns? [14]. Many of the new hadrons appear to be the excited states of proton and neutron which imply that proton and neutron must be the composite systems made out of even more fundamental particles [6]. It also raised a question as to why the particles in multiplets, which otherwise look different, seem to be excited states of one entity? [3]. Responding to these fundamental questions, Gell-mann and Zweig, independently came up with an innovative idea that all hadrons are in fact composed of three elementary particles, which Gell-Mann called *quarks*., which established the foundation of the quark model to be discussed in the following section.

### 3.3 The Quark Model of Hadrons

The idea of three quarks (antiquarks) came to the rescue of the Eightfold Way classification of hadrons. By using all the combination of quarks and antiquarks, baryon and meson multiplets could be constructed conveniently [3, 6, 14].

According to the constituent quark model, all baryons are bound states of three valence quarks while mesons are composed of valence quark- antiquark pairs. Each quark has baryon number  $B=1/3$ , giving  $B=1$  to each baryon. For example, neutron is the lowest bound state of one up quark and two down quarks (udd), while proton is the lowest bound state of two up quarks and one down quark (uud). The baryon,  $\Delta^+$  is an excited state of the three quarks (uud) which make up proton [6]. Since the s quark is massive than u and d quarks, there exist some heavier baryons like  $\Sigma$  and  $\Xi$  etc. In fact, all of the particles in a single super-multiplet have many common features, and this behavior is even more prominent for the particles in a single multiplet. For instance, all particles of a given super-multiplet have the same spin; the masses in a given multiplet are very close, while

those in a super-multiplet are roughly equal. Also, particles in a single super-multiplet, often have very different lifetimes. The relatively small difference in masses can influence the decay probabilities to a great extent [6].

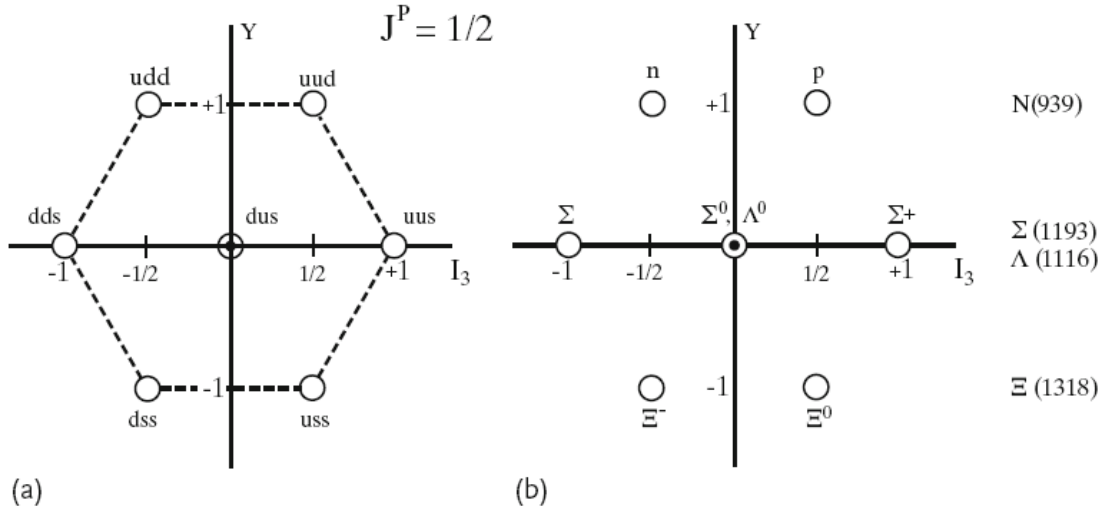


Figure 3.3: Quark structure of baryon octet or  $J^P = (1/2)^+$   $SU(3)$  multiplets [25].

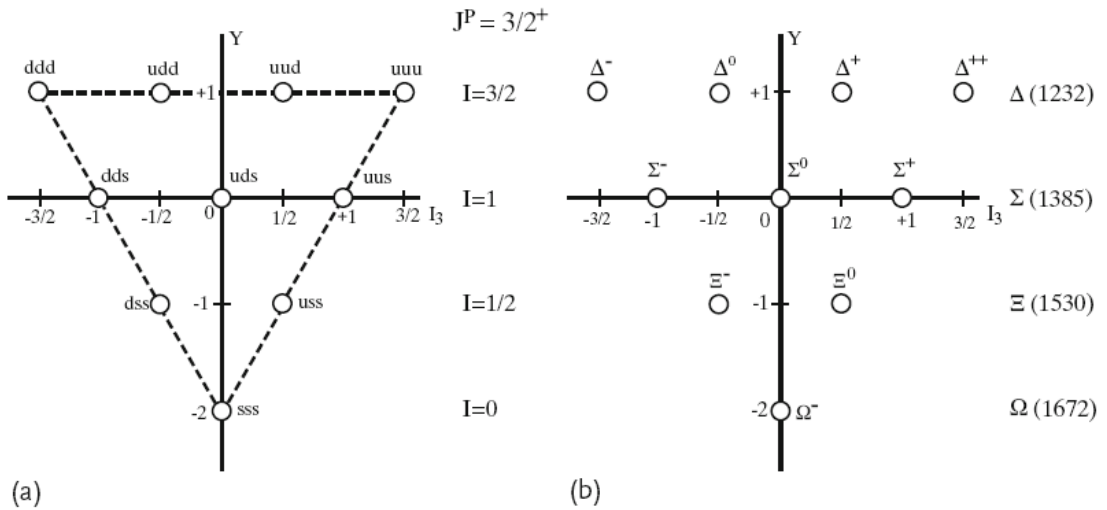


Figure 3.4: Baryon decuplet or  $J^P = (3/2)^+$   $SU(3)$  multiplets [25].

### 3.3.1 Baryons Multiplets

In order to arrange hadrons into symmetrical pattern Gell-Mann and Zweig extended isospin  $SU(2)$  symmetry group, which only incorporates up and down quark, to  $SU(3)$  flavor symmetry group which incorporates up, down and strange quarks. Isospin and strangeness quantum numbers are collectively known as flavor. Now baryon octet and decuplet called flavor multiplets can be defined in terms of three flavors of the quarks. All possible multiplets of baryons discussed so far may be conveniently classified on the basis of quark model by using flavor symmetry group  $SU(3)$ .

For three flavors, there may exist  $3^3 = 27$  distinct flavor states. By using three flavors, u, d and s we get the following baryon multiplet comprising one decuplet, two octets and one singlet [3]:

$$3 \otimes 3 \otimes 3 = 10 \oplus 8 \oplus 8 \oplus 1 \quad (3.5)$$

It was observed experimentally that the total spin of  $\Delta^{++}$  is  $3/2$ , and hence three quarks must be in the same state

$$\Delta^{++} = |u \uparrow u \uparrow u\rangle \quad (3.6)$$

Nevertheless, the existence of  $\Delta^{++}$  and  $\Delta^-$  particles having three fermions (quarks) of same flavour in the same single state is forbidden according to Pauli principle [6, 14]. This problem was tackled by O. W. Greenberg by assigning another quantum number called color charge or strong charge. He suggested that each flavor of quarks comes in three colors: red, green and blue [14]. Owing to their different colors, the three quarks are no more identical and thus are not forbidden to exist in the same state. If we regard the color of antiquark as anticoulour, i.e. antired, antigreen and antiblue, then according to color hypothesis only the colourless bound sates are possible in nature [6, 14]. Each of the super-multiplets as shown in Fig. 3.4, is formed from several multiplets with particles



The 15-plet further consists of an octet, a singlet, a triplet and an anti-triplet (Fig. 3.7) [3]:

$$15 = 3 \oplus 8 \oplus 1 \oplus \bar{3} \tag{3.9}$$

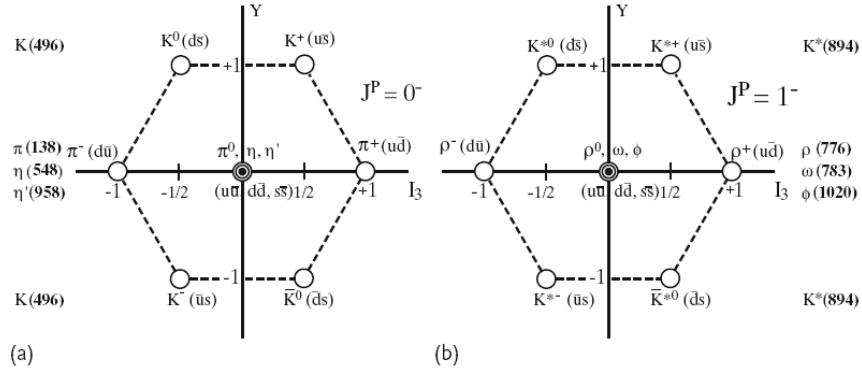


Figure 3.6: SU(3) multiplets of :(a) pseudoscalar and (b) vector mesons [3, 26].

Like charmed barons, charmed mesons were also discovered after the discovery of  $J/\psi$ .  $D^0 = c\bar{u}$  and  $D^+ = c\bar{d}$  were the first charmed mesons [3, 45] as shown in Fig. 3.7. Thus the charmness which was hidden in charmonium revealed itself in charmed baryons and charmed mesons and it was in accordance with the quark model prediction.

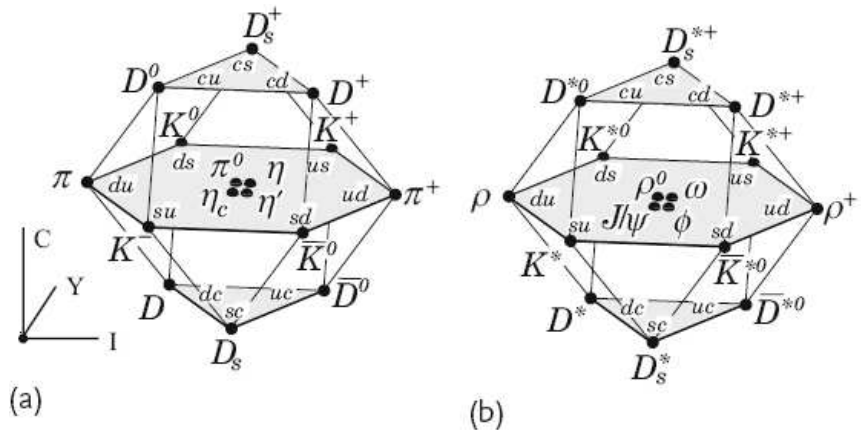


Figure 3.7: SU(4) multiplets of :(a) pseudoscalar mesons (b) vector mesons [3, 26].

# Chapter 4

## The Charmonium Physics

Mesons containing heavy quark-antiquark pairs termed as heavy quarkonia are very important systems to explore the QCD dynamics both within and beyond the Standard Model. Among them is an important quarkonium called charmonium (a  $c\bar{c}$  state). The first charmonia discovered include  $J/\psi$  and  $\psi(2S)$ . After their discovery a chain of their companion states were also discovered. Therefore the group of such states is also called *Charmonium Family*. The charmonium system plays significant role in understanding QCD. Charmonium being non-relativistic system is well suited to understand the production and decay mechanism of heavy quarkonia and spectra of light hadrons from their decays and can be effectively treated perturbatively [46, 47, 48, 49, 50, 51, 52]. In this chapter, we will present experimental and theoretical aspects of charmonium physics. First of all we brief generally about heavy quarkonia in the following section.

### 4.1 Heavy Quarkonia

Heavy quarkonia are multiscale systems which can probe all regions of QCD. At high energies, perturbative expansion in terms of strong coupling  $\alpha_s(q^2)$  is possible. At low energies, non-perturbative techniques are applied. Between these two regions, more complex approaches may be used. Thus heavy quarkonium is an ideal system for investigating the

interplay between perturbative and non-perturbative QCD [33, 46].

Heavy quarkonia are composed of a pair of heavy quark and an anti-quark, whose mass  $m$  is much larger than QCD scale  $\Lambda_{QCD}$ , called the confinement scale. Being non-relativistic systems, heavy quarkonia are characterized by the bound-state velocities,  $v \ll 1$  ( $v^2 \sim 0.3$  for  $c\bar{c}$ ,  $v^2 \sim 0.1$  for  $b\bar{b}$ ,  $v^2 \sim 0.01$  for  $t\bar{t}$ ) and by different energy scales: the hard scale in terms of the mass of quark  $m$ , the soft scale in terms of relative momentum of quark anti-quark pair  $p \sim mv$ , and the ultrasoft scale in terms of the binding energy of quark/anti-quark  $E \sim mv^2$ . Perturbation theory fails at energy scales close to  $\Lambda_{QCD}$  where nonperturbative methods are used. There exists a nonrelativistic hierarchy of scales below the confining scale  $\Lambda_{QCD}$ :  $m \gg p \sim 1/r \sim mv \gg E \sim mv^2$ , where  $r$  is the typical separation between the heavy quark-antiquark pair. Now  $m \gg \Lambda_{QCD}$  implies  $\alpha_s(m) \ll 1$ , which means perturbative technique may always be used for the phenomena occurring at the scale  $m$ . The coupling  $\alpha_s$  may also be small if we have  $mv \gg \Lambda_{QCD}$  and  $mv^2 \gg \Lambda_{QCD}$ , which implies  $\alpha_s(mv) \ll 1$  and  $\alpha_s(mv^2) \ll 1$ , respectively [31, 33].

### 4.1.1 Spectral Notation

We can consider meson as a quark-antiquark “atom”, akin to the electron-nucleus atom or the  $e^+e^-$  atom called positronium [5]. We might expect that same techniques should work for mesons as they did for positronium or ordinary atoms; hence the name “quarkonia” for mesons. Spectroscopic notation for  $q\bar{q}$  system is analogous to that of atomic system like hydrogen or positronium and is given by  $(n+1)^{2S+1}L_J$  [53]. Here  $L$  is the orbital angular momentum,  $S$  is the spin of quark-antiquark pair:  $S = \vec{s}_c + \vec{s}_{\bar{c}}$ , which could be 1 if both of quarks are aligned, and 0 otherwise, hence four possible spin states of quark-antiquark pair split into singlet and a triplet state. For spin singlet state  $S=0$ ,  $J=L$ , while for spin triplet state  $S=1$ ,  $J = L-1, L, L+1$ .  $J$  is the total angular momentum which gives the spin of meson:  $\vec{J} = \vec{L} + \vec{S}$ , here  $2s+1$  is for spin multiplicity. Analogous to atomic physics,  $L=0, 1, 2, 3, \dots$  correspond to  $S, P, D, F, \dots$  states. Different

radial excited states ( $L = 0, n \geq 1$ ) are  $1^1S_0, 1^3S_1, 2^1S_0, 2^3S_1 \dots$  and orbital excited states ( $L = 1, n \geq 1$ ) are  $1^1P_1, 1^3P_{0,1,2}, 2^1P_0, 2^3P_{0,1,2}$ . Space parity  $P$  and charge parity  $C$  are defined by:  $P = (-1)^{L+1}, C = (-1)^{L+S}$ . For a non-relativistic system  $n, L$  and  $S$  are good quantum numbers. But for mesons and baryons which are strongly interacting physical systems,  $J^{PC}$  are good quantum numbers for relativistic systems too, meaning by they can be used to describe a physical state. The  $J^{PC}$  for scalars, pseudoscalars, vectors, axial vectors and tensors are:  $0^{++}, 0^{-+}, 1^{--}, 1^+, 2^{++}$ , respectively. The lowest state with  $L = 0, S = 0$ , and thus  $J = 0$ , is the state  $\eta_c$  with symbol  $1^1S_0$ , while its first radial excited state is  $\eta'_c$  represented by  $2^1S_0$  [53].

#### 4.1.2 Lagrangian for $c\bar{c}$ System

Charmonium mesons are bound states of  $c\bar{c}$  pairs. Mass of charm quark i.e.  $m_c$  is sufficiently large hence the motion of a charm quark inside charmonium system is slow which approximately make charmonium as non-relativistic in nature. According to lattice simulations or potential model calculations we have  $v^2 \sim 0.3$  for charmonium system, where  $v$  is the relative velocity between  $c$  and  $\bar{c}$  inside charmonium. The binding energy is of the order of  $m_c v^2$  while the momentum is of the order of  $m_c v$ . In limit  $v^2 \ll 1$ , there is hierarchy of energy scales in charmonium satisfying the relation  $m_c \ll m_c v \ll m_c v^2$ . The effective field theory incorporating the effects by integrating out the energy scale  $m_c$  is named as nonrelativistic QCD (NRQCD) which expands full QCD in powers of  $v$ . RN-QCD is very suitable effective theory to describe charmonium spectroscopy, its inclusive production and annihilation decays. The effective theory derived by integrating the effects at the energy scale  $m_c v$  containing only the energy scale  $m_c v^2$  is called potential NRQCD (pNRQCD) [46].

The QCD Lagrangian for heavy quarks is as follows :

$$\mathbb{L}_q = \bar{\psi}(x)(iD^\mu - m_c)\psi(x) \quad (4.1)$$

where  $D^\mu = \partial^\mu + gT_a G^{\mu a}$  is the covariant derivative,  $g$  is strong coupling constant and  $G^{\mu a}$  ( $a = 1, 2, \dots, 8$ ) for eight gauge fields of vector gauge bosons of strong interaction i.e eight gluons.

The above Lagrangian includes all energy scale of QCD and hence turns out to be complicated. Simplification can be done by assuming the non-relativistic limit i.e  $v \ll c$  and having cut-off energy scale in the limit  $\Lambda_{QCD} < m_c$ . This decouples the quark and antiquark by suppressing the quark pair creation and annihilation. The effective NRQCD Lagrangian can be written as sum of powers of  $v$  with coefficients called Wilson short-distance coefficients that are determined to match NRQCD and QCD. Fields are represented by two-component Pauli spinor fields  $\psi$  and  $\chi$  for the quark and antiquark respectively. Up to order  $v^4$  NRQCD lagrangian is [46]:

$$L_{NRQCD} = L_l + L_0 + \delta L \quad (4.2)$$

where  $L_l$  is the ordinary Lagrangian for gluons and light quarks and

$$L_0 = \psi^\dagger (iD_0 + \frac{\mathbf{D}^2}{2m_c})\psi + \chi^\dagger (iD_0 - \frac{\mathbf{D}^2}{2m_c})\chi$$

$$\delta L_0 = \frac{c_1}{8m_c^3} \psi^\dagger (\mathbf{D}^2)^2 \psi + \frac{c_2}{8m_c^3} \psi^\dagger g(\mathbf{D} \cdot \mathbf{E} - \mathbf{E} \cdot \mathbf{D})\psi + \frac{c_3}{2m_c} \psi^\dagger g\sigma \cdot \mathbf{B}\psi + i \frac{c_4}{8m_c} \psi^\dagger g \cdot \sigma (\mathbf{D} \times \mathbf{E} - \mathbf{E} \times \mathbf{D})\psi + c.c$$

where  $\delta L$  contains the correction terms to  $L_0$ . Gauge invariance of the theory implies that the appearance of the gluon field in the lagrangian is only via gauge-covariant derivative  $iD_0$ ,  $i\mathbf{D}$  and the QCD field strengths  $\mathbf{E}$  and  $\mathbf{B}$ . The terms  $iD_0$  and  $\frac{\mathbf{D}^2}{2m_c}$  present in  $L_0$  contribute the same order of quarkonium energy. The absence of Pauli matrix  $\sigma^i$  in  $L_0$  reveals the explicit symmetry at leading order of  $v$ . This indicates the degeneracy in the states  $J/\psi$  and  $\eta_c$ , and  $\chi_{c0}$ ,  $\chi_{c1}$ ,  $\chi_{c2}$ , and  $h_c$ . However, the inclusion of spin dependent term  $\sigma^i$  in  $\delta L$  due to next-leading-order corrections violates the explicit symmetry [46].

## 4.2 Discovery of $J/\psi$ and $\psi(2S)$ Charmonia

Despite all its successes, the quark model could not explain the non-existence of a single isolated quark. To this end, idea of quark confinement was put forth which stated that for some unknown reasons quarks are confined within the hadrons. Another explanation was given on the basis of color hypothesis which states that only colorless particles can exist in nature; quark being a colored particle can no more exist in isolation.

Owing to these mysteries, the quark model could not touch the final triumph until the discovery of a new meson called  $J/\psi$  meson. The  $J/\psi$  was found to be electrically neutral and extremely heavy meson having a mass of  $3.1\text{GeV}/c^2$  more than three times the mass of proton. The spin and parity of  $J/\psi$  is  $J^{PC} = 1^{--}$ , where J represents the spin, P is for parity and C is the charge conjugation [3, 6, 54]. The discovery of such heavy meson initiated a wide spread discussion among the particle physicists as to what was its true nature. Nevertheless, the explanation that won the whole discussion was provided by the quark model [14].

As said earlier, the  $J/\psi$  and  $\psi(2S)$ , both are bound states of charm-anticharm pair. The  $J/\psi$  was discovered in 1974, simultaneously at SLAC (by Richter group) and at BNL (by Ting group) [55, 56]. The  $\psi(2S)$  meson was discovered at SLAC, after ten days of this event [57]. At SLAC, these charmonia were observed in the following process:

$$e^+ + e^- \rightarrow (J/\psi, \psi(2S)) \rightarrow e^+ + e^-, \mu^+ + \mu^-, \text{hadrons} \quad (4.3)$$

The above mentioned processes are shown in Figures 4.1 and 4.2.

At BNL,  $J/\psi$  and  $\psi(2S)$  were observed through the following process:

$$P + Be \rightarrow (J/\psi, \psi(2S)) + X \rightarrow e^+ + e^- + X \quad (4.4)$$

where X represents any set of particles allowed by conservation laws.

Narrow peaks were observed at center of mass energy of  $3.1\text{ GeV}/c^2$  (for  $J/\psi$ ) in the

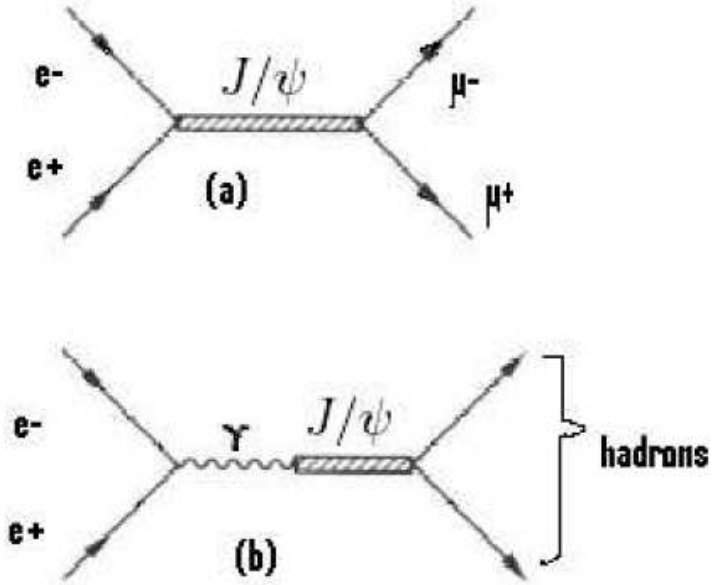


Figure 4.1: Schematic diagram for production of ( $J/\psi$ ) in  $e^+e^-$  collision [54].

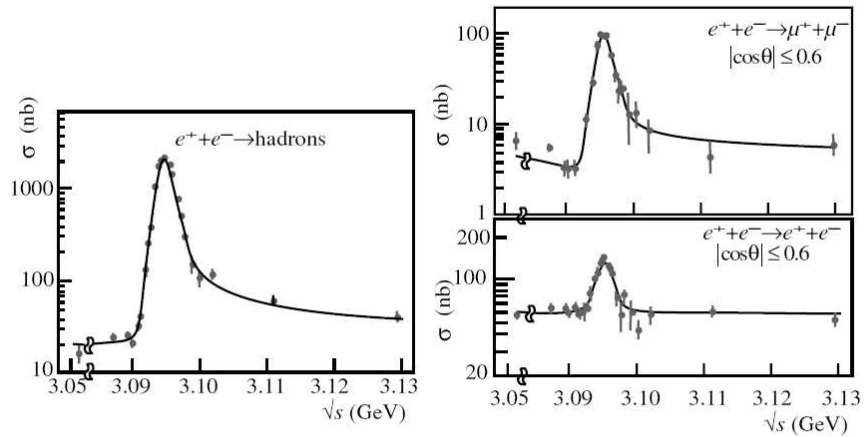


Figure 4.2: Narrow resonance peak of  $J/\psi$  in  $e^-e^+$  at SLAC [25, 55, 56].

cross sections for the above mentioned processes (Figure 4.3).

Production of charmonia in electron positron collision process have many advantages: small background, large cross-section, and well-defined initial state [58]. In electron-positron annihilation processes direct formation of charmonium is possible only for states having the quantum numbers of  $J^{PC} = 1^{--}$ , such as  $J/\psi$ ,  $\psi(2S)$ ,  $\psi(3770)$  and so on [59].

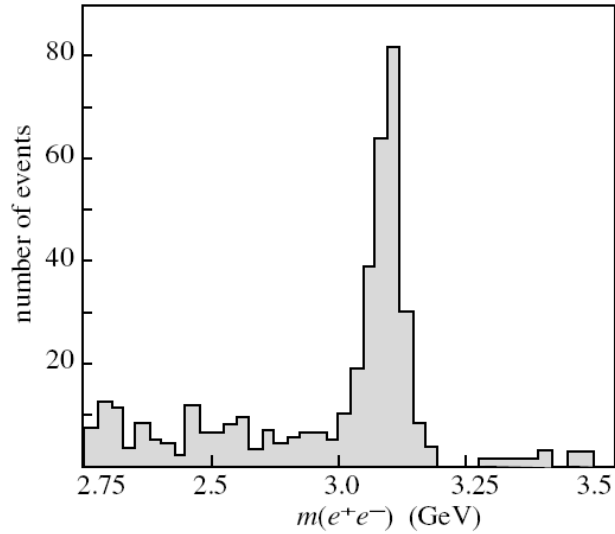


Figure 4.3: Narrow resonance peak of  $J/\psi$  in PP collisions at BNL respectively [25, 55, 56].

### 4.3 Charmonium Spectroscopy

Comparison of charmonium spectrum with that of positronium is shown in Fig. 4.4. From the comparison we see that the states with  $n=1$  and  $n=2$  are similar, however the higher charmonium states do not show  $1/n^2$  feature as compared to positronium. Since the potential determines the relative spacings of the energy levels, it is evident that the potential of the strong interaction for charmonium must be of Coulomb form (at least for  $n=1,2$  i.e. at short distance). This fact is also favored by QCD which describes the short distance interaction between the quarks by *one gluon exchange* (OGE) Coulomb like potential. Also the absence of any degeneracy between  $2^3S$  and  $1^3P$  states in charmonium, in comparison to positronium, indicates that the potential is not of pure Coulomb form (even at fairly short interquark separation). Since quarks have not been observed experimentally in isolation, it seems reasonable to assume a potential which is of Coulomb like at short distances and increases linearly at greater separation, thus leading to the confinement of quarks in hadrons [60].

In the nonrelativistic limit, the spectra of charmonia can be evaluated by solving the

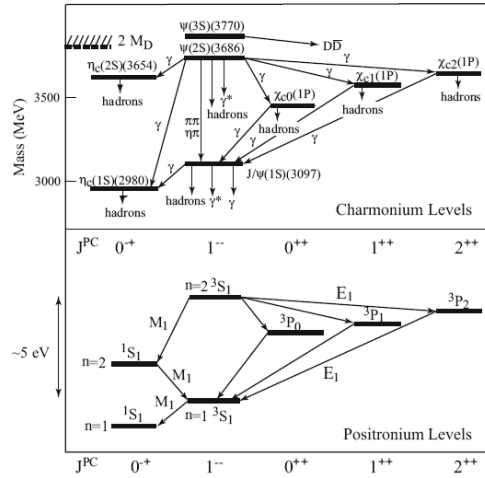


Figure 4.4: Comparison between energy level diagram of positronium and charmonium [46].

non-relativistic Shrodinger equation with conventional quarkonium potential. Charmonium spectrum of experimentally established states and those predicted by nonrelativistic potential model is shown in Fig. 4.5 [8, 61].

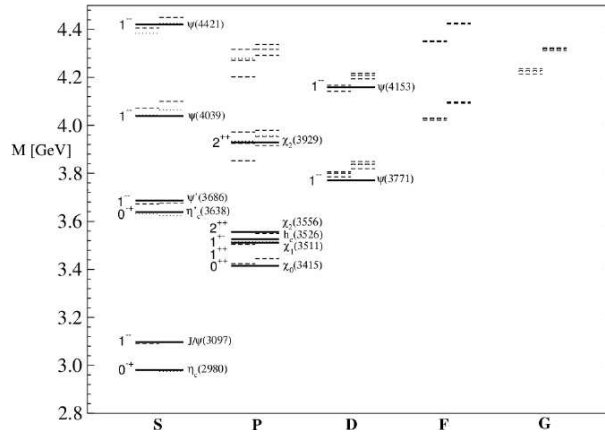


Figure 4.5: Experimentally observed and theoretically predicted charmonium states. The experimentally established states are shown with solid lines. The dotted lines on the left show the predicted states by a non-relativistic potential model while the right dotted lines show the states predicted by the relativistic Godfrey Isgur potential model [8, 61].

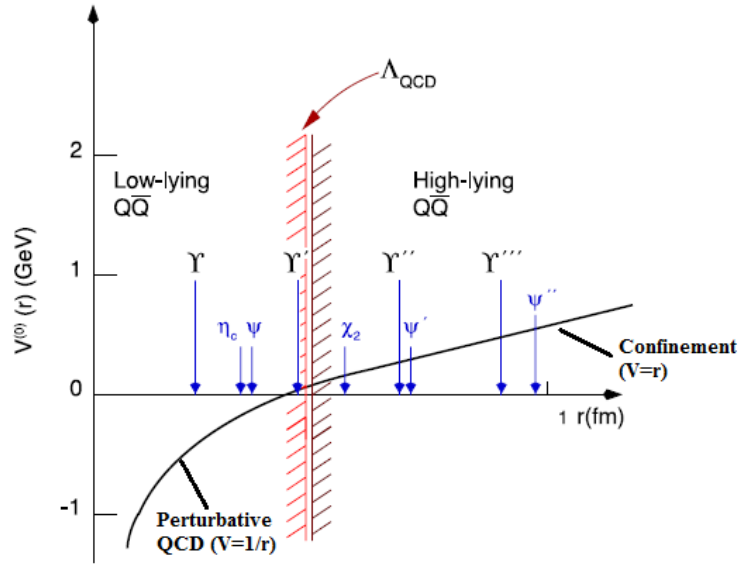


Figure 4.6: Approximate QCD static quarkonium potential as a function of interquark separation  $r$  [4, 33].

The experimentally established charmonium states of relatively narrow widths below the open charm mass  $D\bar{D}$  threshold can be well described by simple  $c\bar{c}$  potential model comprising short distance color Coulomb potential due to *one gluon exchange* (OGE) term and long distance linear scalar confining potential:

$$V_0^{c\bar{c}}(r) = -\frac{4\alpha(s)}{r} + kr \quad (4.5)$$

Its form is shown in Fig. 4.6 [4, 33] which shows the varying sensitivities of Quarkonia systems to the Coulombic and confining interactions. Only Coulomb term is not sufficient for it will not stop ionization of free quarks; but the potential in Eq. (4.5) confines the quarks and the corresponding Schrödinger has no continuum states.

The observed splitting in the narrow states are caused by quark-antiquark spin-dependent coupling, and is consistent with spin-dependent Breit-Fermi Hamiltonian due to OGE plus inverted spin-orbit coupling term due to scalar nature of the linear confining potential:

$$V_s(r) = \frac{32\pi\alpha(s)}{9m_c^2} \vec{S}_c \cdot \vec{S}_{\bar{c}} \delta(\vec{x}) + \frac{1}{m_c^2} \left[ \left( \frac{2\alpha(s)}{r^3} - \frac{b}{2r} \right) \vec{L} \cdot \vec{S} + \frac{4\alpha(s)}{r^3} T \right] \quad (4.6)$$

1. The small spin-orbit potential term, which is generally small, is the cause of fine-structure splitting of levels having the same orbital angular momentum but different total spin  $J$  and can be observed in the  $\chi_{cJ}(c\bar{c})$  triplet states.
2. The spin-spin term, (also called color magnetic term) causes the hyperfine splitting due to spin-spin interaction of the quark and the antiquark. This can be observed in singlet and triplet states, i.e.,  $\eta_c(c\bar{c})$  and  $J/\psi(c\bar{c})$ .
3. The tensor potential, causes mixing between states with the same  $J^{PC}$  but different L and S.

Both  $J/\psi$  and  $\psi(2S)$  decay to hadrons either electromagnetically or strongly. Dominant hadronic decay is through charm-anticharm annihilation into a photon or three gluons [62]. In the mass range 2900 MeV/ $c^2$  to 3700 MeV/ $c^2$ , only eight well-separated and narrow bound states exist in the 800MeV region, each with width  $\leq 20$  MeV/ $c^2$ . Thus, the charmonium system is obviously very “cleaner” and more tractable as compared to light quark mesons [47].

Owing to the similar masses of the light quarks, mesons with light quarks are invariably mixtures of three flavors i.e. up, down and strange. This results into intricate structures owing to overlapping of close lying states. For instance, in the 1000 MeV/ $c^2$  mass region lying between 1500 MeV/ $c^2$  and 2500 MeV/ $c^2$ , there is expectation of as many as 77 mesons having typical widths of 200 MeV/ $c^2$ -400 MeV/ $c^2$ . Also, the small masses of light quarks cause some theoretical problems; the motion of quarks in these light mesons is highly relativistic and, consequently, the value of strong coupling constant is very large which makes it impossible to use perturbative techniques [47].

The  $J/\psi$  is the lowest  $^3S_1$  (triplet) state, but not the ground state of the charmonium family. Actually spin-spin interaction of quark antiqark pair pushes the triplet state up

relative to the singlet ground state  $\eta$  [4, 60].  $\psi(2S)$  is its first radial excited state. Ground state of  $c\bar{c}$  system is the singlet ( $^0S_1$ )  $\eta$  state.  $^3S_1$  states can be formed directly from  $e^-e^+$  collision, for they have quantum numbers of photon. Spin-spin interaction is the cause of shift between  $J/\psi$  and  $\eta$  state. While spin-orbit interaction splits  $\chi$  states.

## 4.4 Transitions

Charmonium higher states decay to low energy states through radiative and strong transitions. Wave functions obtained by solving Schrodinger equation with quark model potential can be used to calculate transition rates for different transitions. For detailed theoretical and experimental aspects of different transitions see Ref. [33].

### 4.4.1 Radiative Transitions

These are electromagnetic transition which occur between quarkonium states via emission of single photon. Radiative transitions are of two types: electric transitions and magnetic transitions. In the non-relativistic limit, quarkonium wave function separates into spin and spatial parts. The spatial part,  $\psi(x)$ , can be written in terms of a radial wave function,  $u_{nl}$ , and spherical harmonics,  $Y_{lm}$ :  $\psi(x) = Y_{lm}(\theta, \phi)u_{nl}(r)/r$ .

where  $n$  is the radial quantum number,  $l$  is the orbital angular momentum,  $s$  is the total spin, and  $J$  is the total angular momentum given as  $J=l+s$ .

The spin of quark is changed by magnetic transitions. In case of electric transitions there is no change in the quark spin. The transitions that do not change the orbital angular momentum are called magnetic dipole, or M1, transitions. While the transitions that change the orbital angular momentum by one unit are called electric dipole, or E1, transitions. Transitions for which  $n = n'$  are called allowed M1 transitions, otherwise they are called hindered or forbidden transitions.

### 4.4.2 Hadron Transitions

The general expression for a hadronic transition is:  $\psi_i \rightarrow \psi_f + h$ , where  $\psi_i$ ,  $\psi_f$  and  $h$  represent quarkonia of initial state, final state, and the emitted light hadron(s) respectively. In the  $c\bar{c}$  and  $b\bar{b}$  systems, the kinematically allowed final light hadron(s)  $h$  are dominated by single particle ( $\pi^0, \eta, \omega, \dots$ ) or two-particle ( $2\pi$  or  $2K$ ) states because the mass difference  $m_{\psi_i} - m_{\psi_f}$  changes from a few hundred MeV to slightly over a GeV. Until now, twenty hadronic transitions have been observed experimentally [33]. For study of low lying heavy-quarkonium states, hadronic decay modes are important. Such transitions can be calculated by non-perturbative QCD.

### 4.5 OZI Rule

It was found by Okubo, Zweig and Iizuka, that the decay rate of  $\phi$  meson (bound state of  $s\bar{s}$ ) into 2 Kaons ( $K^+K^-$ ) is greater than into three 3 pions, despite the latter is energetically favored decay mode because mass of three pions is less than mass of two kaons. The puzzle was explained by OZI rule [63] which states that process with broken quark lines is suppressed. Hence decay mode shown in Fig. 4.7a is OZI suppressed while decay mode shown in Fig. 4.7b is OZI allowed. It was also verified experimentally, because decay width of  $\phi$  was found to be smaller than expected [4, 5].

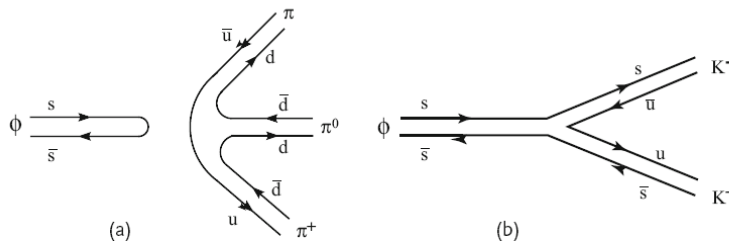


Figure 4.7: Quark diagrams for decay of  $\phi$  into decay mesons. (a) OZI suppressed transition (b) OZI allowed transition [4].

In fact in case of OZI suppressed decay mode, the intermediate state is that of pure gluons. These gluons must be of high energy (“hard”) since they carry the total mass of  $\phi$  meson. While in the case of OZI allowed decay mode the intermediate gluon is of low energy (“soft”), since strange/antistrange meson pairs share most of the energy. Hence according to OZI rule processes that proceed through hard-gluon exchange are suppressed. The coupling of soft-gluons with quarks is more stronger than that of hard-gluons, so the soft-gluon exchanges are more probable [4, 5, 16].

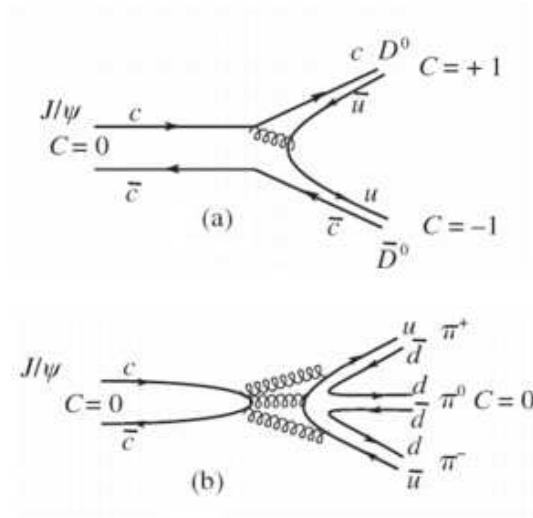


Figure 4.8: Quark diagrams for  $J/\psi$  decaying to mesons. (a) OZI allowed transition (b) OZI suppressed transition [5].

Similarly we can apply OZI rule to explain the narrow width of about 90 KeV and long life of  $J/\psi$  which is  $\simeq 10^{20}s$ , shorter than EM decays, but 1000 times longer than that of typical strong decay. The preferred decay of the  $J/\psi$  into charm meson is shown in Fig. 4.8a. However, this process is energetically disfavored because  $M_{J/\psi} < 2M_D$ , where  $M_D$  is the lightest meson mass with nonzero charm, while the mass  $2M_D$  is the charm threshold. Now the only possible hadronic allowed decay mode for  $J/\psi$  is through OZI suppressed decay mode as shown in Fig. 4.8b. It is because  $J/\psi$  and its decay products are

color singlets, the decay process should proceed by exchange of color-singlet combination of gluons which require at least two gluons. But  $J/\psi$  has spin-1 and is known to be produced via one photon exchange in  $e^+e^-$  annihilation, so it must have  $C=-1$ . Gluons being bosons also have  $C=-1$ , so at least three gluons must be exchanged carrying all the energy of  $J/\psi$  as shown in Fig. 4.8b. Thus the much slower OZI suppressed decay mode gives relatively long lifetime to  $J/\psi$  [4, 5, 16].

## 4.6 $\rho\pi$ Puzzle

In accordance with the OZI rule the suppressed  $J/\psi$  and  $\psi(2S)$  decays to hadrons are via three gluons or a photon. According to prediction of pQCD the ratio of the branching fractions of  $J/\psi$  and  $\psi(2S)$  in either case is [33, 64]:

$$\frac{Br[\psi(2S) \rightarrow h]}{Br[\psi \rightarrow h]} = \frac{Br[\psi(2S) \rightarrow e^+e^-]}{Br[\psi \rightarrow e^+e^-]} \approx 12.7\% \quad (4.7)$$

This relation is expected to hold true to a certain degree both for inclusive as well as inclusive decays. Since 1983 there are lots of experimental evidences for the violation of this rule in some decay channels especially in  $\rho\pi$  decay channel, hence the “ $\rho\pi$  puzzle” [65].

Variety of solutions have been proposed for the puzzle [33, 66] and have been tested against the experimental results from CLEOc, BESII, and BESIII by two-body decays of  $J/\psi$  and  $\psi(2S)$  with more accuracy, which are vector-tensor (V T), vector-pseudoscalar (V P), pseudoscalar-pseudoscalar (PP), and baryon-antibaryon (BB) modes, and by multi-body decays of  $J/\psi$ ,  $\psi(2S)$  or even by the  $J/\psi(3770)$ . Theoretically, since the Q-value is smaller than 12%, in the case of  $\rho\pi$  enhanced or suppressed  $J/\psi$  decay rate may cause it, or both.

For an extensive study of 12% rule, enough measurements of  $\psi(2S)$  and  $J/\psi$  decay modes have been carried out, the highest priority, however, has been given to the

measurement of Vector-Pseudoscalar (VP) modes, like the  $\rho\pi$ . For these modes, it is generally found that the ratios of the branching fractions relative to 12% are enhanced for Pseudoscalar-Pseudoscalar (PP) modes, while for the non-isospin violating VP and Vector-Tensor (VT) modes are suppressed (i.e., excluding modes like  $\omega\pi^0$  and  $\rho^0\eta^0$ ). Among the baryon anti-baryon and the multihadron modes, some are enhanced, some are suppressed, and some match the expectation of the rule. Solution for all of the measured channels is yet to be provided by the theoretical models, which have been developed for interpreting specific modes [33].

# Chapter 5

## BES-III Experiment

<sup>1</sup>Experimental knowledge of particle physics mostly results from colliding particles together at very high speeds which results in very energetic collisions [5]. This is why sometimes particle physics is also called high energy physics. The machine used to accelerate the particles at very high speed is called accelerator. While the device used to get the physical information emerging from these collisions is called detector.

This chapter is about BESIII experimental apparatus. We will briefly discuss the significance of electron positron colliders, the construction and working of different parts of BESIII detector, and physics goals of BESIII experiment.

### 5.1 Fixed Target Accelerators Versus Colliders

Most of the earlier accelerators were fixed-target in which moving beam collides with target at rest. Such accelerators produce limited energy and interactions after collision and hence have been replaced with special kind of accelerators called colliders. In such machines both beams and target are set to motion and are smashed into each other inside the detector that monitors their collision for useful information. If  $E_b$  is the beam energy,

---

<sup>1</sup>The details of this chapter are available in scholarly work of different authors. If any reference is found missing that will be totally un-intentional.

$m_t$  is the mass of target particles, then the total energy is  $E_{total} \simeq \sqrt{2E_b m_t c^2}$ . However, in the case of collider when both the beam and target are moving toward each other we have  $E_{total} \simeq 2E_b$ . Therefore, large energy is available in colliders which in turn increases the number of particle produced during interaction. But this large energy comes at the price of reduced luminosity. Typical luminosity for colliders is  $\sim 10^{31} cm^{-2} s^{-1}$ , whereas for fixed target machines it is  $\sim 10^{37} cm^{-2} s^{-1}$  [5].

Luminosity is related to another useful physical quantity called differential cross section which can be measured experimentally. If a beam of incoming particles with uniform luminosity  $L$  is directed towards a target then the number of particles crossing differential cross-section  $d\sigma$  per unit time is  $dN = Ld\sigma$ . Hence:

$$dN = Ld\sigma = L \frac{d\sigma}{d\Omega} d\Omega \Rightarrow \frac{d\sigma}{d\Omega} = \frac{1}{L} \frac{dN}{d\Omega} \quad (5.1)$$

Particle physicists describe cross section as the likelihood of interaction between particles. In other words it characterizes the probability of occurrence of a particular physical reaction, or the statistical nature of scattering events. For instance when two particles collide with each other, their cross section is a measure of the interaction event between them. Unit of the cross section is area, usually it is expressed in barn.

The quantity of interest for experimentalists working in HEP is the number of measured events. For instance, in order to measure the angular distributions one can measure events per unit space angle to measure the angular distribution. The number of events measured depends upon the cross section  $\sigma$ , integrated luminosity of the physical process  $L$  and the detector efficiency  $\epsilon$  i.e.  $N = \sigma L \epsilon$  [67].

## 5.2 Electron-Positron Colliders

For more than 40 years,  $e^+e^-$  colliders have proved to be an innovative experimental tools to investigate fundamental phenomenon in particle physics in general and Stan-

Standard Model in particular. The hallmark of such colliders is their huge luminosity in the low energy region to explore many dimensions of Standard Model and physics beyond Standard Model with greater precision. Standard Model can not answer many questions about nature. The questions are either related to the unexplored energy region or non-perturbative QCD [46]. For example, it is expected that at energy far above 100 GeV, some new phenomenon (supersymmetry, dark matter) and new particles (supersymmetric particles, weakly interacting massive particles) may result. LHC is aimed at investigating phenomenon related to Standard Model and new physics, and ILC is being planned to test and confirm the results of LHC with better accuracy. Although QCD has been well tested in perturbative regime, at short distance, but it is not useful technique at long distance where for large value of strong coupling constant non-perturbative effects appear. These effects are very crucial regarding the structure and spectrum of hadrons. To address such effects, we need lower energy with high luminosity. The better place for such process is no other than  $e^+e^-$  colliders.

The promising advantage of  $e^+e^-$  colliders lies in the fact that  $e^+e^-$  annihilation creates virtual photons with  $J^{PC} = 1^{--}$  which are directly coupled to quarks and leptons [68]. Thus many meson states with quantum numbers of photons can be directly produced in electron positron colliders. They provide a clean environment with low background and well defined initial state to study many aspects of Standard Model [68, 69, 70].

In factuality,  $e^+e^-$  colliders can produce plethora of charmonium states with large cross sections and abundant resonances and thus are ideal laboratories for the study of charmonium, charm and QCD. Charm quark lies at the border line of pQCD and non-pQCD and study of production and decay of bound states of charm anti-charm quark can be useful to probe Lattice QCD. Decay of charmonium through three-gluon loop is one of the best channels to search for hybrids and glueballs [71] which are predicted by QCD but yet to be established experimentally.

Many electron-positron colliders were built in late 60s and early 70s. SPEAR is the

prominent example where both the  $J/\psi$  and tau were discovered which was the beginning of the tau-charm physics. Many charmonium states and charmed mesons were discovered at Doris and SPEAR. Examples of contemporary colliders are the Phi factory at Frascati, KEKb collider at Tsukuba, the BEPCII collider at IHEP Beijing focussing on  $\phi$  meson and kaon production, B physics, and tau-charm physics respectively [72]. But here we discuss only BEPCII/BESIII (for detail construction and working of BESIII see Refs. [46, 68, 70, 73]).

### 5.3 BEPCII Collider

BEPCII [73] (Beijing electron positron collider) is an upgradation of BEPC and is a double-ring multi-bunch collider (Fig. 5.1) with a design luminosity of  $\sim 1 \times 10^{33} \text{cm}^{-2} \text{s}^{-1}$  and energy of 1.89 GeV and beam current of 0.9 A.

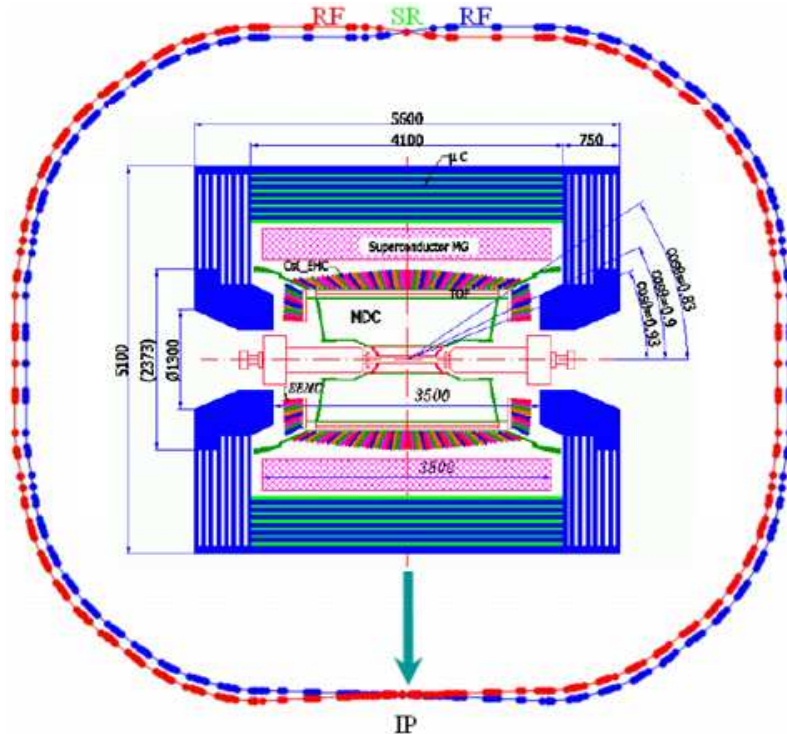


Figure 5.1: Schematic diagram for  $e^+e^-$  BEPCII collider and BESIII detector [68].

Physics data taking at BEPCII started in March of 2009. Each ring has circumference of 237.5 m and can be filled with up to 93 bunches with a bunch length of 1.5 cm. Beams of electron and positrons collide at the southern interaction region with a horizontal crossing-angle of  $\pm 11 \text{ mrad}$ . Current of single beam is designed to be 0.91 A. Superconducting Micro- $\beta$  quadruples, Superconducting RF system of 500 MH and low impedance vacuum chambers are used.

## 5.4 BEPCII Detector

BESIII [73] is a general purpose detector and upgraded from its predecessor BESII. It consists of four sub-detectors namely; Main Drift Chamber (MDC), Time Of Flight (TOF) chamber, Electro-magnetic Calorimeter (EMC) and Muon (MU) chamber (Fig.5.1). Their working and functions are briefly described in the following section.

- The multilayer main drift chamber (MDC) is the most important component of the BES-III detector and surrounds the beam pipe. It is composed of inner and outer chambers without any intervening wall. The polar angle coverage of the MDC is  $|\cos\theta| < 0.93$ . Length of MDC is 2.4m with an inner radius of 60 mm and outer radius of 800 mm. Drift cells have 43 cylindrical layers, coaxial with the beam pipe, 8 layers in the inner chamber and 35 layers in the outer chamber. In the inner chamber all 8 layers are stereo; in the outer chamber there are 19 axial layers and 16 stereo layers which are interleaved in the outer chamber. There are 6796 signal wires, in total.

Particle identification and tracking is important part of job for experimentalists during their analysis. Particles are usually identified from their paths traversed in detector in magnetic fields. Charged particles move in straight lines in the absence of magnetic field, but magnetic field bend their path into curves. From the curvature, momentum of particles is measured which is used to identify particles. In BESII

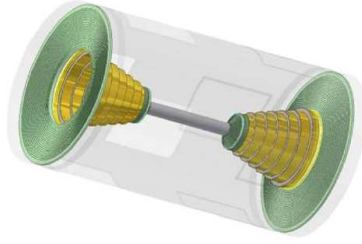


Figure 5.2: Schematic diagram of MDC [68].

MDC detector is used for tracking of relatively low momentum charged particles by precisely measuring their momentum, as well as for particle identification by measuring their specific energy lost i.e.  $dE/dx$ . The normalized pulse height, which is proportional to  $dE/dx$ , is a function of  $\beta\gamma = p/m$ , where  $m$  and  $p$  are the mass and momentum of a charged particle. Using  $dE/dx$  pulse height measurements, we cannot distinguish Pions, electrons and muons with momenta around 0.2 GeV/c. Similarly, the  $dE/dx$  pulse heights will not separate electrons from kaons in the 0.5-0.6 GeV/c momentum range. The  $dE/dx$  measurement resolution is expected to be between 6% and 7% after calibration.  $3\sigma$   $K/\pi$  separation can be carried out by using  $dE/dx$  information, for momentum below 0.6 GeV/c; for all momenta above 0.4 GeV/c a good  $e/\pi$  separation can be achieved .

Single wire resolution of MDC is better than  $120 \mu m$  and a  $dE/dX$  resolution is better than 6%. The momentum resolution  $\sigma_p/p$  is better than 0.5% in magnetic field of 1T for charged tracks with a momentum of 1 GeV/c. Length of MDC is 2.4 m, with outer radius of 800 mm, and inner radius of 60 mm, thus covering the polar angle  $|\cos\theta| < 0.93$ . there are 43 cylindrical layers of drift cells that are coaxial with the beam pipe. Mixture of Helium-propane gas is used to decrease the process of multiple coulomb scattering and re-interaction in the gas.

- The Time-of-Flight (TOF) sub-detector consists of plastic scintillator counters and is placed between MDC and the electromagnetic calorimeter (EMC). TOF consists of

barrel and endcap. The barrel part covers the polar angle  $|\cos\theta| < 0.83$ , the endcap covers  $0.85 < |\cos\theta| < 0.95$ . The Barrel of two layers of 88 plastic scintillators are arranged in a cylinder; A fine mesh PMT at each end can read out each scintillator. There is an array of 48 fan-shaped elements at each endcap of TOF; these can be read out by a single fine-mesh PMT from one end of the scintillator.



Figure 5.3: Schematics of TOF [68].

TOF is exploited in BESIII detector to identify particles of relatively high momenta by measuring their flight time. It can also measure the energy loss  $dE/dx$  for both neutral and charged particles. In order to improve the shower energy resolution, this energy loss can then be added to that in the EMC. TOF can also help to reject cosmic ray backgrounds and provides a fast trigger. Combined expected time resolution for the two-layer barrel is between 100 and 110 ps for  $K$ s and  $\pi$ s, providing  $2\sigma K/\pi$  separation up to 0.9 GeV/c. The velocity ( $\beta c$ ) and mass ( $m$ ) of the charged particle can be calculated as

$$\beta = \frac{L}{c \times t_{mea}}, m^2 = p^2 \times \frac{1 - \beta^2}{\beta} \quad (5.2)$$

where  $p$  and  $L$  are the corresponding momentum of the charged particle given by MDC measurements and flight path, and  $c$  is the velocity of light in vacuum, and  $t_{mea}$  is the measured time-of-flight,

- The Electro-Magnetic Calorimeter (EMC) is important sub-detector of BESIII detector. It consists of one barrel and two endcap parts. The polar angle coverage of barrel part is  $|\cos\theta| < 0.83$ . while that of endcap is  $0.85 < |\cos\theta| < 0.93$ . The total acceptance is 93% of  $4\pi$ . The barrel consists of 44 rings of crystals along the z direction, each with 120 crystals. Each endcap comprises 6 rings that are split into two tapered half-cylinders. There are 6272 CsI(Tl) crystals in the calorimeter.

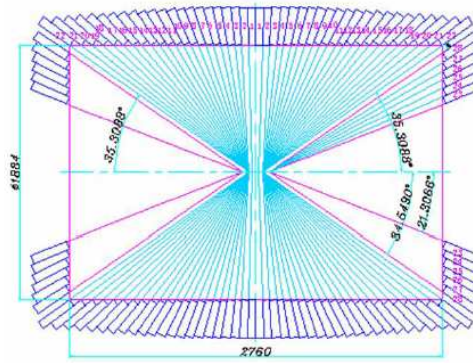


Figure 5.4: Schematic diagram for EMC [68].

The EMC measures positions and the the energies of electrons and photons precisely and its designed energy measurement range for electrons or photons is from 20 MeV to 2 GeV. The spatial and energy resolutions are 0.6 cm and 2.5% at 1 GeV, respectively. For PID the shape of the shower and the energy deposited can be used as discrimination variables. Electromagnetic showers of electrons and positrons result from loss of all of their energies in the calorimeter, the ratio of deposited energy to the track momentum  $(E/p) \approx 1$ .

- BESIII muon identifier (MU) system comprises layers of resistive plate chambers(RPCs) inserted in the steel plates of the magnetic flux return yoke of the solenoid magnet. The barrel part of the muon identifier is divided into octants, each consisting of 9 layers of muon counters inserted into gaps in the iron. Each endcap is organized into quadrants, each of which consists of 8 RPC layers.

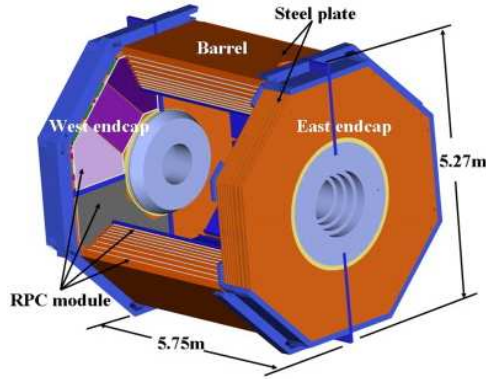


Figure 5.5: Schematic diagram for muon chamber [68].

The muon identifier chamber basically distinguishes muons from charged pions, other hadrons and backgrounds based on their hit patterns in the flux return yoke. Identification of muons with the lowest possible momentum is important for muon chamber. Average energy lost by muons as minimum ionizing particles is 160 MeV in the 28 cm long CsI crystals. Bending of muons in the solenoid magnetic field can also effect their minimum momentum that can be identified. Muon identifiers start to become effective at the minimum muon momentum of approximately 0.4GeV/c.

It is very important for BESIII detector to measure muons, since in  $e^+e^-$  collision many final state physics processes contain one or two muons. Important evidence in this regard was the narrow sharp enhancement of  $e^+e^-\mu^+\mu^-$  cross-section in the discovery of  $J/\psi$  meson. Mass of  $\tau$  at BES was also precisely measured mainly through  $e^+e^-\tau^+\tau^- \rightarrow e\mu + 4\nu$  [4]. For instance, measurement of branching fraction of purely leptonic decay, study of semi leptonic decay etc. rely on the ability of muons identification [5].

## 5.5 Physics Goals of BEPCII/BESIII

It is now well recognized by the high energy physics community that comprehensive studies of  $e^+e^-$  annihilation in the charm-tau threshold region is very crucial and can open some new horizons regarding the process of hadronization and the interplay of perturbative and non-perturbative aspects of QCD. The quarks were accepted as truly dynamical objects of SU(3) gauge group mainly after the discoveries of the low-lying charmonia and of open-charmed hadrons. For the past few years, the interest in hadron spectroscopy with and without charm has been enhanced considerably after the surprising discoveries of many charm resonances around 4 GeV region, the narrow  $D_{s,J}$  mesons, and X(1835) at BESII [46].

Violation of the famous 12% rule has been observed with different decay channels of  $J/\psi$  and  $\psi(2S)$ . The detection of some Cabibbo-suppressed  $J/\psi$  decay channels is also expected with huge data samples. Such decays will be useful to detect possible effects of new physics at BEPCII. It will also offer an opportunity to search for evidence of flavor-changing neutral currents. These with many other phenomenon are expected to be studied at BESIII with even greater precision for the understanding of non-perturbative QCD. We summarize physics goals of BESIII as follows [73].

- High precision tests of electroweak interactions in quark and leptons sector
- Study of light hadron spectroscopy and decay properties with high statistics.
- High precision studies of the production and decay properties of the charmonium  $J/\psi$ ,  $\psi(2S)$  and  $\psi(2377)$  states.
- Search for quark hybrids, multi-quarks states, glueballs and exotic states via hadronic and radiative decays of charmonium.
- $\tau$ -physics studies
- Studies of production and decay properties of charm mesons including D and  $D_s$  and charmed baryons.

- Precise measurement of standard model parameters such as CKM matrix etc.
- To investigate physics beyond standard model or new physics by probing area of oscillations, CP violations and forbidden decays in c-hadron and  $\tau$ -lepton sector.

# Chapter 6

## Analysis Results

### 6.1 Introduction

Charmonium system has played a crucial role to understand strong force [33, 46, 47, 74]. The production of  $J/\psi$  and  $\psi(2S)$  in  $e^+e^-$  annihilation and their two body hadronic decays can be used to test the predictive power of QCD/pQCD [75]. Such two-body hadronic decays of  $J/\psi$  and  $\psi(2S)$  are predicted to proceed either through annihilation of  $c\bar{c}$  into three gluons or into a photon [62]. The resultant photon or gluons may lead to hadron anti-hadron pairs.

Decay modes of charmonium involving baryon-antibaryon pairs is a good experimental laboratory to explore many fundamental questions about baryon physics. Charmonium being a bound state of charm-anticharm quark is a good probe to study many aspects of QCD both in perturbative and non-perturbative region [76]. In the production of charmonium states in hadronic interactions the interplay between perturbative QCD (pQCD) and non-perturbative QCD is especially significant. At the scale of the charm quark mass  $m_c$ , the strength of strong coupling constant  $\alpha_s(m_c^2)$  becomes sufficiently small and is suitable to apply pQCD so as to describe parton level production of  $c\bar{c}$  pair [77].

Conventional picture of baryons is that they consists of three quarks. Theoretical study of baryon system is limited owing to their complex structure. The composition and interaction of three valence quarks, sea quarks and gluons inside the baryons is not fully understood yet [78]. The non-relativistic constituent quark model (NRQCM) successfully describes the static properties like mass and magnetic moment of the spatial ground states of SU(3) octet and decuplet baryons. However, its predictions about excited states of baryons are not well established [79]. The quark model also predicts some missing baryons in the light quark sector and QCD predicts the existence of hybrid baryons with gluonic field in excited state, but such states are yet to be observed experimentally.

The experimental study of baryonic decays of  $J/\psi$  and  $\psi(2S)$  is an excellent technique to trace the structure and properties of conventional baryons and their excited states such as  $\Lambda^*$ ,  $\Xi^{*+}$ ,  $\Xi^*$ ,  $\Sigma^*$  etc.

Sine the innovative discovery of the  $J/\psi$  and  $\psi(2S)$  at BNL and SLAC in 1974 [55, 56], many tow-body exclusive baryonic decay modes of these charmonia have been observed. However, many two-body baryonic decays are still un-observed. The BESIII data sample of  $2.25 \times 10^8$   $J/\psi$  events and data sample of  $1.06 \times 10^8$   $\psi(2S)$  events offer a good opportunity for experimentations to look for such missing decays. It also provides a novel opportunity to look for new decay channels of  $J/\psi$  and  $\psi(2S)$  and test the famous “12% rule” which is defined as:

$$Q_h = \frac{B(\psi(2S) \rightarrow h)}{B(J/\psi \rightarrow h)} = \frac{B(\psi(2S) \rightarrow e^+e^-)}{B(J/\psi \rightarrow e^+e^-)} \simeq 12\%.$$

So far, no experimental study has been tried for the decay channel;  $J/\psi \rightarrow \Xi^0(1530)\bar{\Xi}^0(1530)$ . While for the decay mode;  $\psi(2S) \rightarrow \Xi^0(1530)\bar{\Xi}^0(1530)$ , only an upper limit has been reported [80].

## 6.2 Data Set and Software Framework

These analyses are based on  $2.25 \times 10^8$   $J/\psi$  events and  $1.06 \times 10^8$   $\psi(2S)$  events collected with the BESIII detector at  $e^-e^+$  collider; BESPCII from 12th June to 28th July 2009.

BOSS(BESIII Offline Software System) [81] version 6.5.5 has been used as the software framework for the data analysis. BOSS is based on Gaudi framework [82].

Monte-Carlo (MC)simulation is carried out for the determination of detection efficiency of each channel, optimize event selection criteria and backgrounds. Event generator is provided by BOOST (BESIII Object Oriented Simulation Tool) which contains the description of detector geometry and simulates the detector response and signal digitization. For the description of detector material and the tracking of the decay particles through the detector Geant4 [83], has been used. The generator KKMC [84], has been exploited for the production of charmonium resonances such as  $J/\psi$  and  $\psi(2S)$ . BesEvtGen [85] is used to generate signal events of  $J/\psi \rightarrow \Xi^0(1530)\bar{\Xi}^0(1530)$  and  $\psi(2S) \rightarrow \Xi^0(1530)\bar{\Xi}^0(1530)$ , using J2BB2 model.

About 225M  $J/\psi$  and 106 M  $\psi(2S)$  inclusive MC samples are used to estimate possible background channels. In these samples, the branching ratios of the main known hadronic decay modes are set to world average values according to Particle Data Group (PDG) 2010, while the remaining physics process are generated by Lundcharm [86].

## 6.3 Analysis of $J/\psi \rightarrow \Xi^0(1530)\bar{\Xi}^0(1530)$

### 6.3.1 Initial Event Selection

- Good Charged Track Selection.

A track is a good charged track if it is well fitted to a three dimensional helix, originates from the interaction point and has a polar angle in the range  $|\cos\theta| < 0.93$ .

The decay channel under investigation is 8 charged track system and follows the

following sequence of event topology:

$$J/\psi \rightarrow \Xi^0(1530)\bar{\Xi}^0(1530), \Xi^0(1530) \rightarrow \Xi^- \pi^+, \Xi^- \rightarrow \Lambda \pi^-, \Lambda \rightarrow p \pi^- \text{ and } \bar{\Xi}^0(1530) \rightarrow \bar{\Xi}^+ \pi^-, \bar{\Xi}^+ \rightarrow \bar{\Lambda} \pi^+, \bar{\Lambda} \rightarrow \bar{p} \pi^+.$$

Therefore, 8 final state charged particles are listed as:  $p\bar{p}\pi^+\pi^+\pi^+\pi^-\pi^-\pi^-\pi^-$ .

1. The tracks are reconstructed from MDC with good helix fit.
  2. Polar angle in MDC:  $|\cos\theta| < 0.93$ .
  3. Transverse momentum  $p_t < 0.05 \text{ GeV}/c$ .
  4. Using the technique of one missing track [44], in the selected events the number of good charged tracks satisfying the above criteria is 7 or 8. Total charge is 0 for 8 good charge tracks. Total charge is +1 or -1 for 7 charge tracks.
- Particle Identification.
    1. In particle identification only dE/dx information of MDC is used.
    2. In order to avoid loss of efficiency, only proton and anti-proton are identified.
    3. Proton is identified with the condition;  $prob(p) > prob(\pi^+)$  and  $prob(p) > prob(K^+)$ .
    4. Anti-proton is identified with the condition;  $prob(\bar{p}) > prob(\pi^-)$  and  $prob(\bar{p}) > prob(K^-)$ .
  - Kinematic Fitting.
 

After successful identification of good charged tracks, an event having 7 or 8 identified particles is accepted for further analysis. In case of 8 identical particles ( $N_p = 1, N_{\bar{p}} = 1, N_{\pi^+} = 3, N_{\pi^-} = 3$ ), four constraint (4-C) kinematic fit is applied with the hypothesis;  $J/\psi \rightarrow p\bar{p}\pi^+\pi^+\pi^+\pi^-\pi^-\pi^-$  using conservation of total momentum and energy. While for events with seven identified particles ( $N_p = 1, N_{\bar{p}} = 1, N_{\pi^+} \leq 3, N_{\pi^-} \leq 3$ ), one constraint (1-C) kinematic fit is used with one of the hypothesis:  $J/\psi \rightarrow p\bar{p}\pi^+\pi^+\pi^+\pi^-\pi^-$  ( $\pi^-$  missing) or  $J/\psi \rightarrow p\bar{p}\pi^+\pi^+\pi^-\pi^-\pi^-$  ( $\pi^+$  missing).

- Selection of  $\Lambda/\bar{\Lambda}, \Xi^-/\bar{\Xi}^+, \Xi^0(1530)/\bar{\Xi}^0(1530)$

$\Lambda$  and  $\bar{\Lambda}$  are required to be reconstructed using candidate  $p/\bar{p}$  and looping over the negative/positive charged tracks of three  $\pi^-/\pi^+$ . The selected track  $\pi^-/\pi^+$  that comes from the decay of  $\Lambda/\bar{\Lambda}$  should have minimum mass deviation of  $\Lambda/\bar{\Lambda}$  ( $\Delta = M_{p\pi^-}/M_{\bar{p}\pi^+} - 1.116$ ).  $\Lambda/\bar{\Lambda}$  selection is followed by the selection of  $\Xi^-$  and  $\bar{\Xi}^+$ , which are to be reconstructed with candidate  $\Lambda/\bar{\Lambda}$  and looping over the remaining two  $\pi^-/\pi^+$ . Selected track coming from the decay of  $\Xi^-/\bar{\Xi}^+$  should have minimum mass deviation of  $\Xi^-/\bar{\Xi}^+$  ( $\Delta = M_{\Lambda\pi^-}/M_{\bar{\Lambda}\pi^+} - 1.321$ ). Finally  $\Xi^0(1530)$  and  $\bar{\Xi}^0(1530)$  are selected from the combination of  $\Xi^-/\bar{\Xi}^+$  and one free  $\pi^+/\pi^-$ .

The invariant mass distributions after kinematic fit are shown in Figs. 6.1, 6.2 and 6.3.

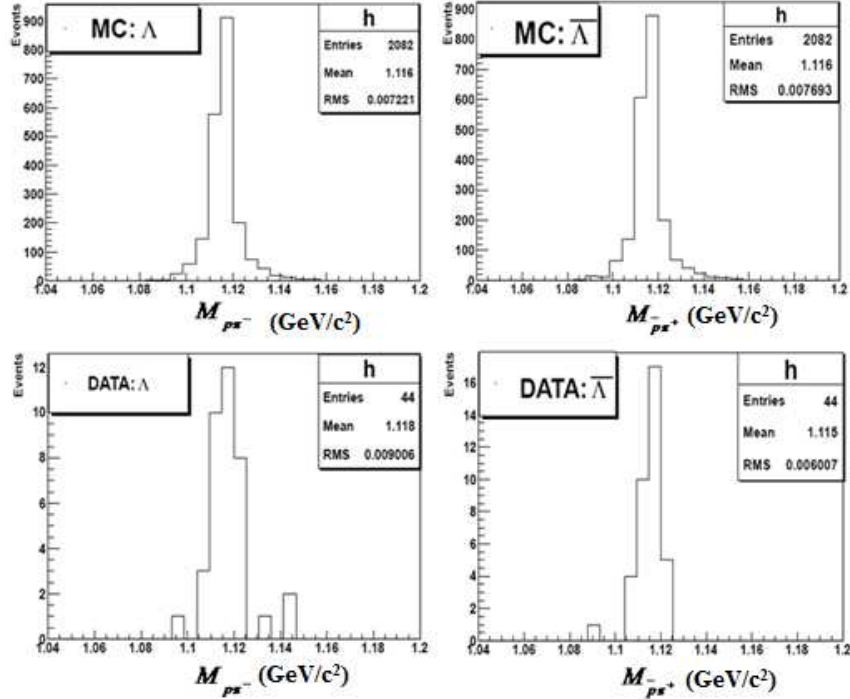


Figure 6.1: MC and data invariant mass distributions of  $p\pi^-$  and  $\bar{p}\pi^+$  after kinematic fit results

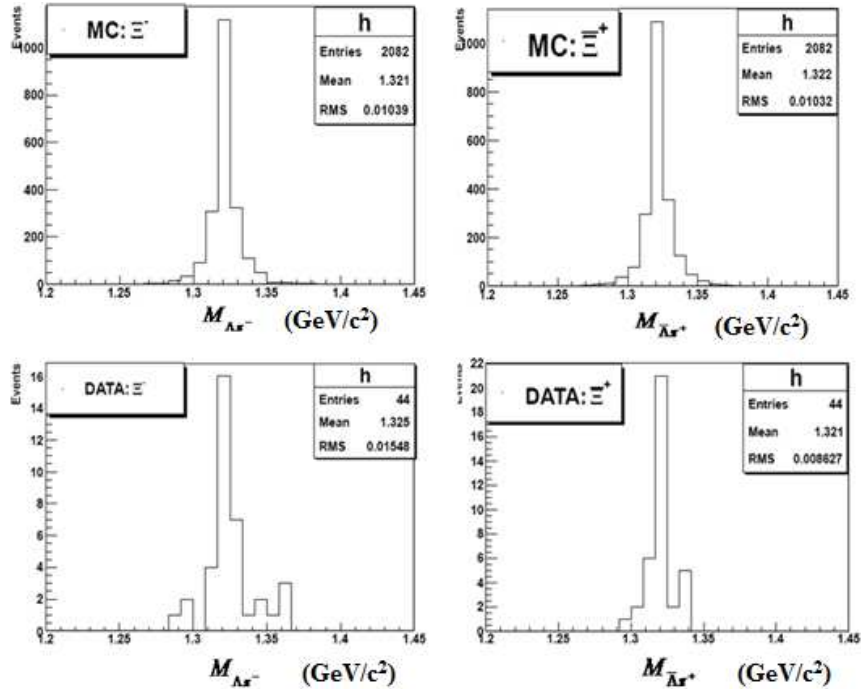


Figure 6.2: MC and data invariant mass distributions for  $\Lambda\pi^-$  and  $\bar{\Lambda}\pi^+$  after kinematic fit results

### 6.3.2 Final Event Selection

- $\chi^2$  Optimization

In order to get pure signal we further suppress background by optimizing  $\chi^2$ . This is also done to enhance the signal to signal plus background ratio i.e.  $\frac{S}{\sqrt{S+B}}$ . Here S is for signal and B for background. For signal, MC sample is used and for S+B, data is used. We have optimized  $\chi^2$  for 1C kinematic fit and set its threshold value at 80.

To get more refined signal events with minimum possible background, we have applied following mass cuts in the range of  $3\sigma$  along with  $\chi^2 < 80$  for final event selection. The mass constraints used are listed below:

- mass cut for  $p\pi^-$  distribution:  $|M_{p\pi^-} - 1.1156| < 0.012$

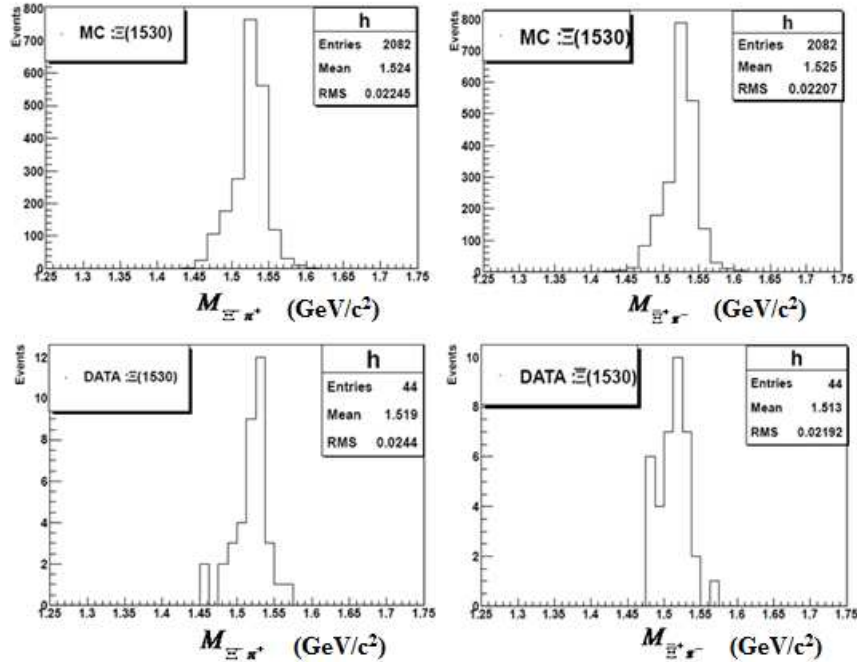


Figure 6.3: MC and data invariant mass distributions for  $\Xi^- \pi^+$  and  $\Xi^+ \pi^-$  after kinematic fit results

- mass cut for  $\bar{p}\pi^+$  distribution:  $|M_{\bar{p}\pi^+} - 1.1156| < 0.012$
- mass cut for  $\Lambda\pi^-$  distribution:  $|M_{\Lambda\pi^-} - 1.321| < 0.015$
- mass cut for  $\bar{\Lambda}\pi^+$  distribution:  $|M_{\bar{\Lambda}\pi^+} - 1.321| < 0.015$
- mass cut for  $\Xi^- \pi^+$  distribution:  $|M_{\Xi^- \pi^+} - 1.531| < 0.03$
- mass cut for  $\Xi^+ \pi^-$  distribution:  $|M_{\Xi^+ \pi^-} - 1.531| < 0.03$

After relevant final event selection criteria as stated above, important MC and data invariant mass distributions without 1C and 4C fit results are shown in Figs. 6.4-6.6. While the same MC and data invariant mass distributions after 1C and 4C fit results are shown in Figs. 6.7-6.12

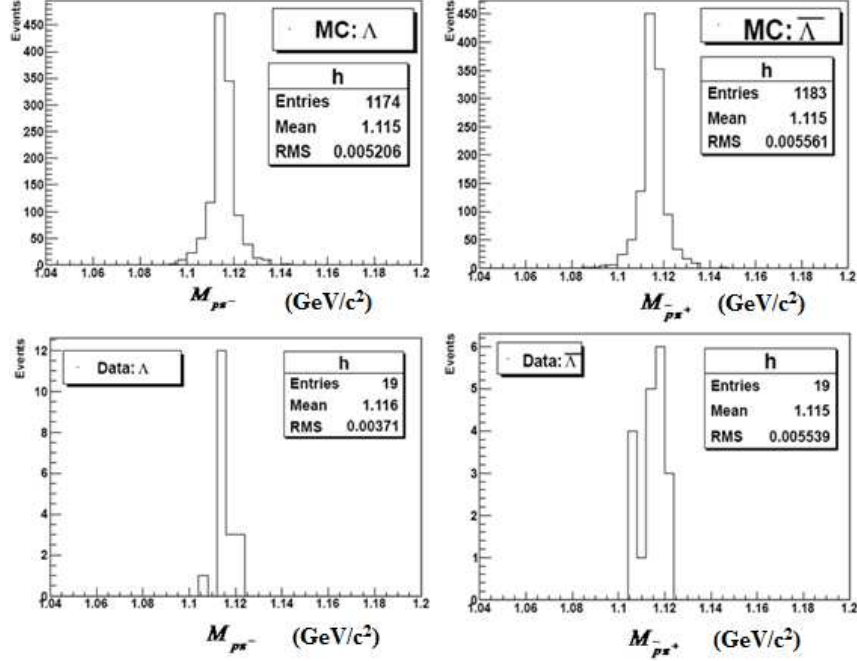


Figure 6.4: MC and data invariant mass distributions for  $p\pi^-$  and  $\bar{p}\pi^+$  after final event selection criteria

### 6.3.3 Background Analysis

Background was estimated from exclusive channels, about 225 M MC inclusive events and side band region.

#### 1. Background from Inclusive Monte Carlo

No appreciable peaking background was found from any inclusive MC decay channels as shown in the Table 6.1.

#### 2. Background from Exclusive Background

For exclusive background, we have generated phase space MC sample events of 1M for the following 8 charged tracks channels:  $J/\psi \rightarrow \Lambda^0(1405)\bar{\Lambda}^0(1405)$ , where  $\Lambda^0(1405) \rightarrow \Sigma^{*+}\pi^-, \bar{\Lambda}^0(1405) \rightarrow \bar{\Sigma}^{*-}\pi^+, \Sigma^{*+} \rightarrow \Lambda\pi^+, \Lambda \rightarrow \pi^-p, \bar{\Sigma}^{*-} \rightarrow \bar{\Lambda}\pi^-, \bar{\Lambda} \rightarrow \bar{p}\pi^+$ ;  $J/\psi \rightarrow \Lambda^0(1405)\bar{\Lambda}^0(1405)$ , where  $\Lambda^0(1405) \rightarrow \Sigma^{*-}\pi^+, \bar{\Lambda}^0(1405) \rightarrow \bar{\Sigma}^{*+}\pi^-, \Sigma^{*-} \rightarrow \Lambda\pi^-, \Lambda \rightarrow \pi^-p, \bar{\Sigma}^{*+} \rightarrow \bar{\Lambda}\pi^+, \bar{\Lambda} \rightarrow \bar{p}\pi^+$ ;  $J/\psi \rightarrow \Xi^-\bar{\Xi}^+\pi^+\pi^-$ , where  $\Xi^- \rightarrow \Lambda\pi^-, \Lambda \rightarrow \pi^-p$  and  $\bar{\Xi}^+ \rightarrow \bar{\Lambda}\pi^+, \bar{\Lambda} \rightarrow \pi^+\bar{p}$ ; and  $J/\psi \rightarrow \Lambda^0(1520)\bar{\Lambda}^0(1520)$ , where  $\Lambda^0(1520) \rightarrow \Lambda\pi^+\pi^-, \Lambda \rightarrow$

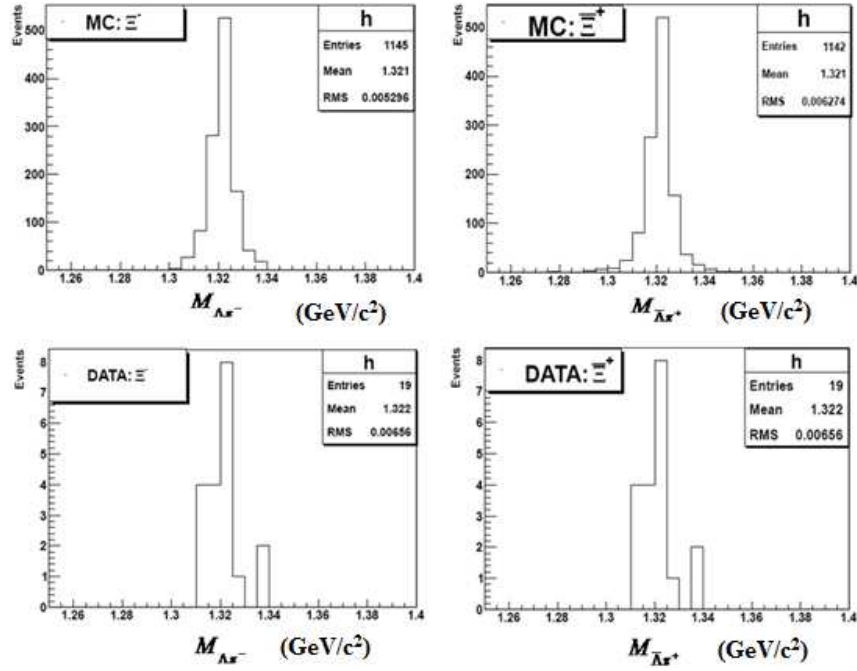


Figure 6.5: MC and data invariant mass distributions for  $\Lambda\pi^-$  and  $\bar{\Lambda}\pi^+$  after final event selection criteria

No	Decaychannels	Final states	$N_{\text{evt}}$
1	$J/\Psi \rightarrow \Xi^- \bar{\Xi}^0(1530)\pi^+$ $\Xi^- \rightarrow \Lambda\pi^-, \Lambda \rightarrow p\pi^-$ $\bar{\Xi}^0(1530) \rightarrow \bar{\Xi}^-\pi^+, \bar{\Xi}^- \rightarrow \bar{\Lambda}\pi^+, \bar{\Lambda} \rightarrow \bar{p}\pi^+$	$p\bar{p}\pi^-\pi^+\pi^-$ $\pi^-\pi^+\pi^-$	2
2	$J/\Psi \rightarrow \Xi^-\Xi^0(1530)\pi^+$ $\Xi^0(1530) \rightarrow \Xi^-\pi^+, \Xi^- \rightarrow \Lambda\pi^-, \Lambda \rightarrow p\pi^-$ $\Xi^- \rightarrow \bar{\Lambda}\pi^+, \bar{\Lambda} \rightarrow \bar{p}\pi^+$	$p\bar{p}\pi^-\pi^+\pi^-$ $\pi^-\pi^+\pi^-$	1
3	$J/\Psi \rightarrow \bar{\Sigma}(1385)^+\pi^-\Sigma(1385)^+\pi^-$ $\bar{\Sigma}(1385)^+ \rightarrow \bar{\Lambda}\pi^+, \bar{\Lambda} \rightarrow \bar{p}\pi^+$ $\Sigma(1385)^+ \rightarrow \Lambda\pi^+, \Lambda \rightarrow p\pi^-$	$p\bar{p}\pi^+\pi^+\pi^-$ $\pi^-\pi^+\pi^-$	1
4	$J/\Psi \rightarrow \bar{\Sigma}(1385)^-\pi^+\Sigma(1385)^+\pi^-$ $\bar{\Sigma}(1385)^- \rightarrow \bar{\Lambda}\pi^-, \bar{\Lambda} \rightarrow \bar{p}\pi^+$ $\Sigma(1385)^+ \rightarrow \Lambda\pi^+, \Lambda \rightarrow p\pi^-$	$p\bar{p}\pi^+\pi^+\pi^-$ $\pi^-\pi^+\pi^-$	0

Table 6.1: MC inclusive background decay modes for the signal channel:  $J/\psi \rightarrow \Xi^0(1530)\bar{\Xi}^0(1530)$ .

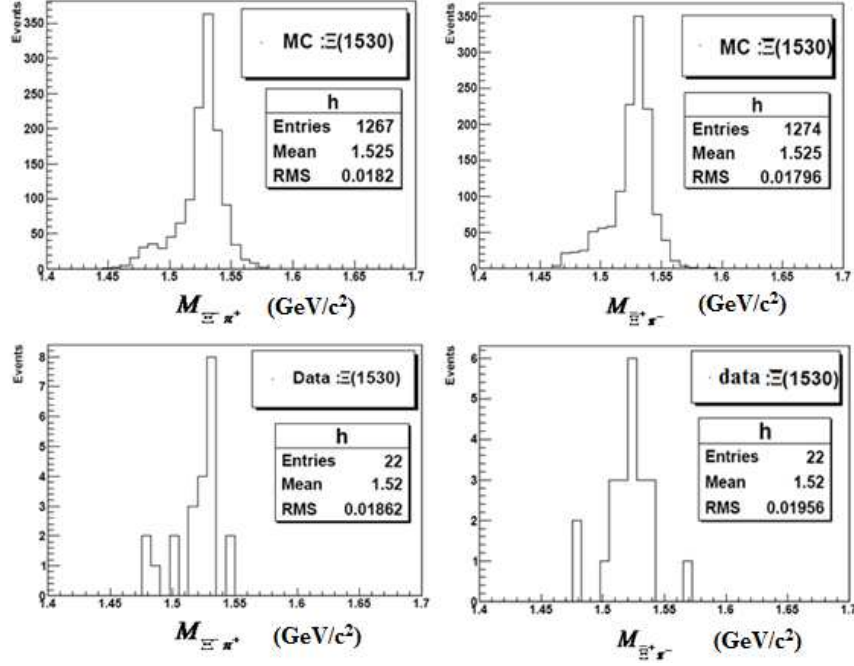


Figure 6.6: MC and data invariant mass distributions for  $\Xi^- \pi^+$  and  $\Xi^+ \pi^-$  after final event selection criteria

$p\pi^-$ ,  $\bar{\Lambda}^0(1520) \rightarrow \bar{\Lambda}\pi^+\pi^-$ ,  $\bar{\Lambda} \rightarrow \bar{p}\pi^+$ . Invariant mass spectra of  $\Xi^- \pi^+$  and  $\Xi^+ \pi^+$  for the above mentioned decay MC inclusive background decay channels are shown below in Figs. 6.13-6.16, while the respective scatter plots for these decay channels are shown in Figs. 6.17-6.21.

### 3. Background from Sideband

In order to estimate background for the signal channel:  $J/\psi \rightarrow \Xi^0(1530)\bar{\Xi}^0(1530)$  from sideband region, scatter plot of  $\Xi^0(1530)$  vs  $\bar{\Xi}^0(1530)$  for 1C and 4C fit results is shown in Fig. 6.21. Background is estimated from side band boxes,  $0.012 \text{ GeV}/c^2$  away from signal box. Signal and side bands have width of  $6\sigma$  i.e.  $0.072 \text{ GeV}/c^2$ . The range for signal  $\Xi^0(1530)$  is  $1.495 < |M_{\Xi^- \pi^+}| < 1.567$  while range for side bands (N4,N3) and (N1,N5) is  $1.409 < |M_{\Xi^- \pi^+}| < 1.483$  and  $1.495 < |M_{\Xi^- \pi^+}| < 1.567$  respectively. Range for signal  $\bar{\Xi}^0(1530)$  is  $1.495 < |M_{\Xi^+ \pi^-}| < 1.567$  while range for side bands (N1,N3) and (N4,N5) is  $1.409 < |M_{\Xi^+ \pi^-}| < 1.483$  and  $1.495 < |M_{\Xi^+ \pi^-}| < 1.567$  respectively.

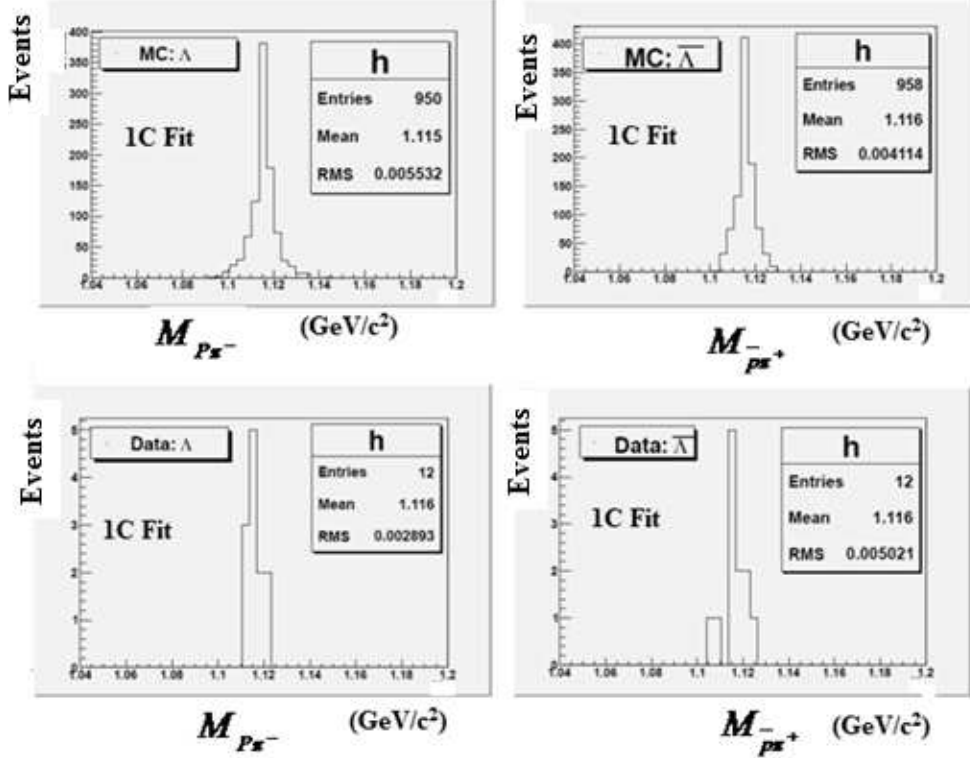


Figure 6.7: MC and data invariant mass distribution for  $p\pi^-$  and  $\bar{p}\pi^+$  after 1C fit results

Now background events for 1C and 4C fits are estimated by formula  $N^{bkg} = (N4 + N5 - N1 - N3)/2 + N2$ . The number of events from 1C and 4C fits for the signal channel  $J/\psi \rightarrow \Xi^0(1530)\bar{\Xi}^0(1530)$  are estimated to be  $10 \pm 3.5$  and  $7 \pm 2.6$  respectively.

### 6.3.4 Determination of Branching Fraction

Branching ratio for the decay channel  $J/\psi \rightarrow \Xi^0(1530)\bar{\Xi}^0(1530)$  is measured using the formula:

$$Br[J/\psi \rightarrow \Xi^0(1530)\bar{\Xi}^0(1530)] = \frac{N^{obs}}{\varepsilon \cdot N^{J/\psi} \cdot Br[\Lambda \rightarrow p\pi^-]^2 \cdot Br[\Xi^- \rightarrow \Lambda\pi^-]^2}$$

Where number of observed events  $N^{obs}$  for 1C and 4C fits are  $10 \pm 3.5$  and  $7 \pm 2.6$  respectively, total number of  $J/\psi$  events  $N^{J/\psi}$  are  $(225.3 \pm 2.8) \times 10^6$ , branching fraction of intermediate resonances are  $Br[\Lambda \rightarrow p\pi^-] = 0.639$  and  $Br[\Xi^- \rightarrow \Lambda\pi^-] = 0.9987$  [87]. MC % efficiency for 1C fit is measured to be 1.03 %, while MC % efficiency for 4C fit is

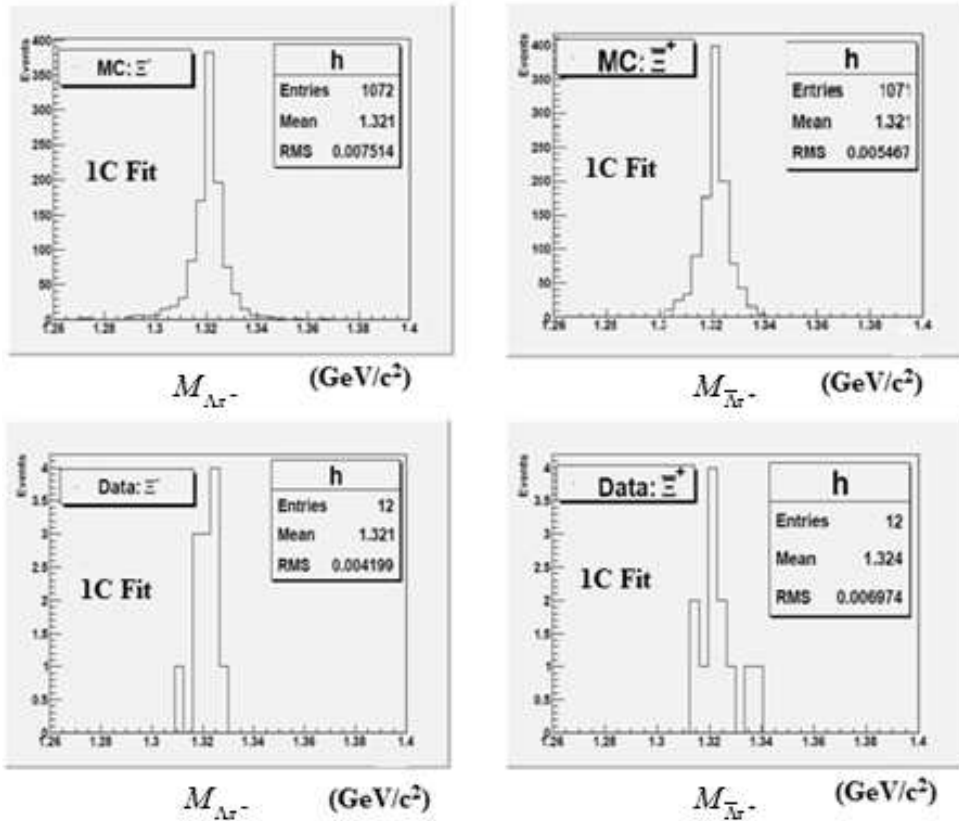


Figure 6.8: MC and data invariant mass distribution for  $\Lambda\pi^-$  and  $\bar{\Lambda}\pi^+$  after 1C fit results

measured to be 0.26%. The overall detection efficiency for 1C and 4C fit for the signal channel  $J/\psi \rightarrow \Xi^0(1530)\bar{\Xi}^0(1530)$  is 1.29 %. Now branching ratios for 1C and 4C fits are measured to be  $(1.06 \pm 0.37_{stat}) \times 10^{-5}$  and  $(2.94 \pm 1.10_{stat}) \times 10^{-5}$  respectively which are consistent within  $2\sigma$ .

### 6.3.5 Systematic Error Analysis

#### 1. Particle Identification.

The systematic error due to particle identification is taken as 1% each for proton and anti-proton from the Ref. [79]. So total systematic error from this source is 2%.

#### 2. MDC Tracking.

The systematic error due to MDC tracking detection efficiency is taken as 1% for each

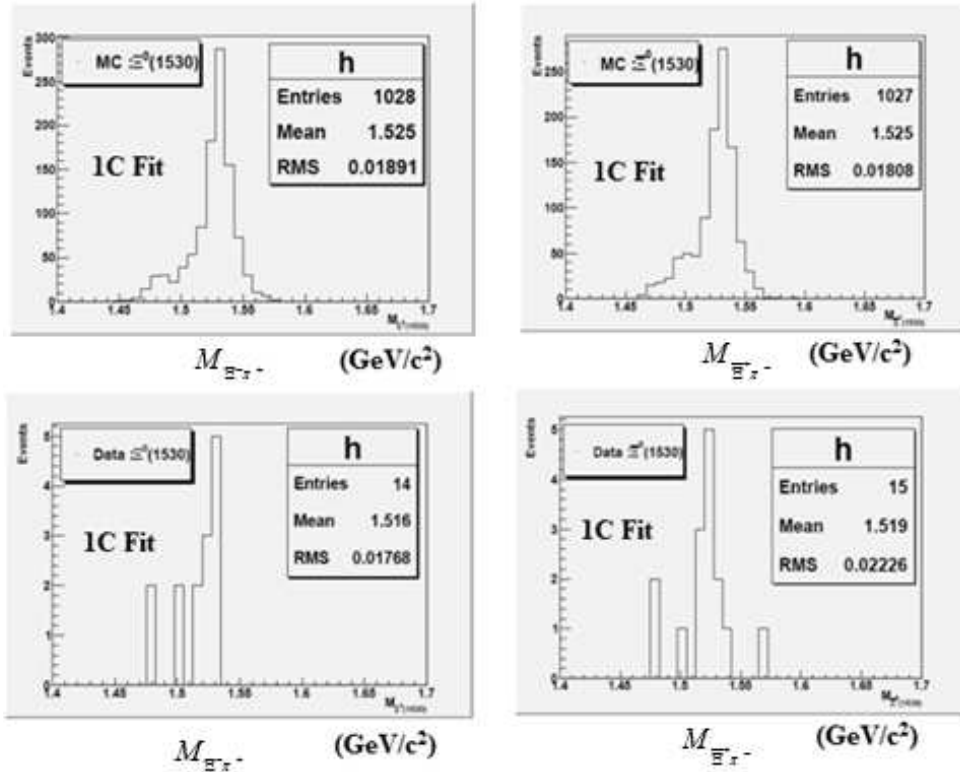


Figure 6.9: MC and data invariant mass distribution for  $\Xi^-\pi^-$  and  $\Xi^+\pi^-$  after 1C fit results

charged track as calculated in Ref. [79]. As there are 8 charged tracks in the final states, so systematic error from this source is taken as 8% for 4C tracking and 7% for 1C tracking.

The systematic error due to MDC tracking detection efficiency is taken as 1% for each charged track as calculated in Ref. [79]. As there are 8 charged tracks in the final states, so systematic error from this source is taken as 8% for 4C tracking and 7% for 1C tracking.

**3. Total Number of  $J/\psi$  Events.** Systematic error from  $(225.3 \pm 2.8) \times 10^6$  number of  $J/\psi$  events is 1.24 % [88].

**4. Error from MC Model.** PHSP MC sample of 100000 events was generated and MC detection efficiency was compared with J2BB2 sample. Relative error in MC detection efficiency is determined to be 0 %.

### 5. Monte Carlo Statistical Error

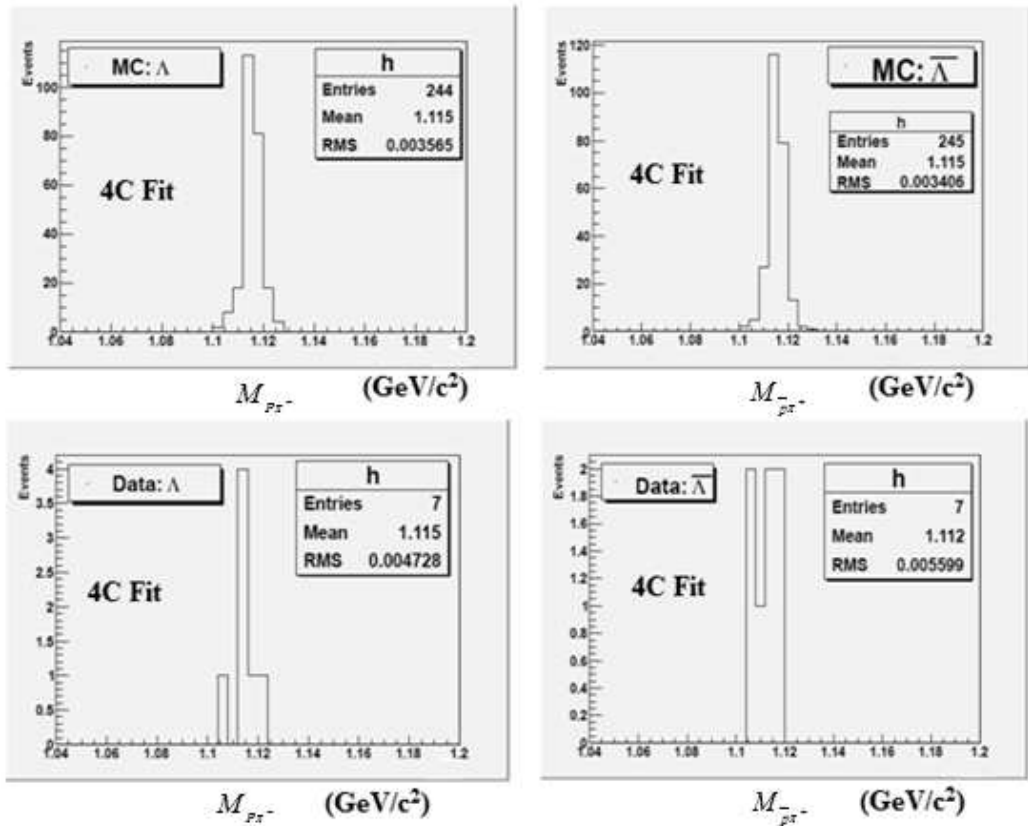


Figure 6.10: MC and data invariant mass distribution for  $p\pi^-$  and  $\bar{p}\pi^+$  after 4C fit results

The monte carlo statistical error for 1C and 4C fit results was estimated by using the respective detection efficiencies and the total number of events of the signal channel  $J/\psi \rightarrow \Xi^0(1530)\bar{\Xi}^0(1530)$  generated by J2BB2 generator in the relation [44]

MC Statistical Error =  $\frac{\Delta\epsilon}{\epsilon} = \frac{\sqrt{\frac{\epsilon(1-\epsilon)}{N_{gen}}}}{\epsilon}$ . Where  $\epsilon$  and  $N_{gen}$  represent the detection efficiency and total number of signal MC generated events. Using the value of detection efficiencies for 1C and 4C kinematic fit results, the monte carlo statistical errors for 1C and 4C fit results are 3.1% and 6.2% respectively.

## 6. Error from Intermediate Resonances.

Systematic Error due to branching ratio of intermediate resonances is calculated to be 1.5%:

$$\text{Br}[\Lambda/\bar{\Lambda} \rightarrow \pi^- p/\pi^+ \bar{p}] = (63.9 \pm 0.5)\%$$

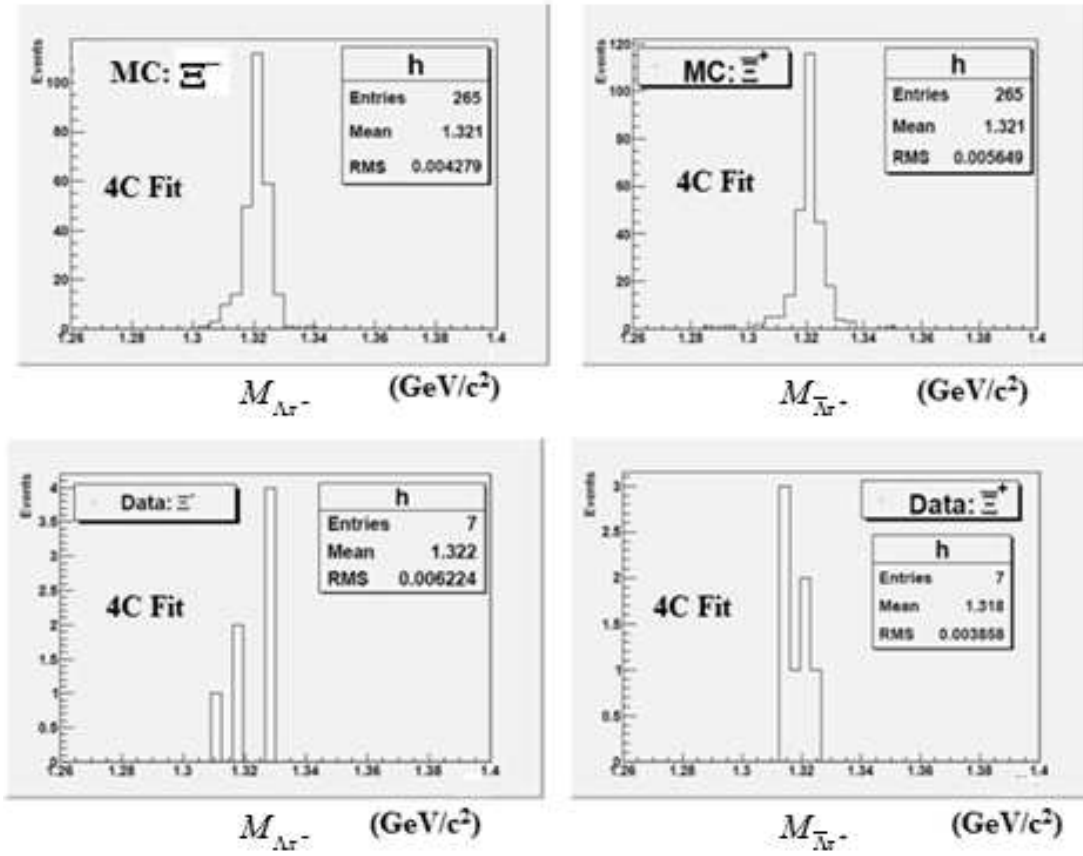


Figure 6.11: MC and data invariant mass distribution for  $\Lambda\pi^-$  and  $\bar{\Lambda}\pi^+$  after 4C fit results

$$\text{Br}[\Xi^-/\bar{\Xi}^+ \rightarrow \Lambda\pi^-/\bar{\Lambda}\pi^+] = (99.89 \pm 0.035)\%.$$

Therefore the system error in branching fraction from this source is 1.5%.

Now the total systematic error for 1C and 4C fit results is shown below in Table 6.2 and Table 6.3 respectively.

Therefore, after incorporating systematic error branching ratios for 1C and 4C fit results are given by:

$$\text{Br}^{1C}[J/\psi \rightarrow \Xi^0(1530)\bar{\Xi}^0(1530)] = (1.06 \pm 0.07_{\text{sys}} \pm 0.37_{\text{stat}}) \times 10^{-5}$$

and

$$\text{Br}^{4C}[J/\psi \rightarrow \Xi^0(1530)\bar{\Xi}^0(1530)] = (2.94 \pm 0.06_{\text{sys}} \pm 1.10_{\text{stat}}) \times 10^{-5}.$$

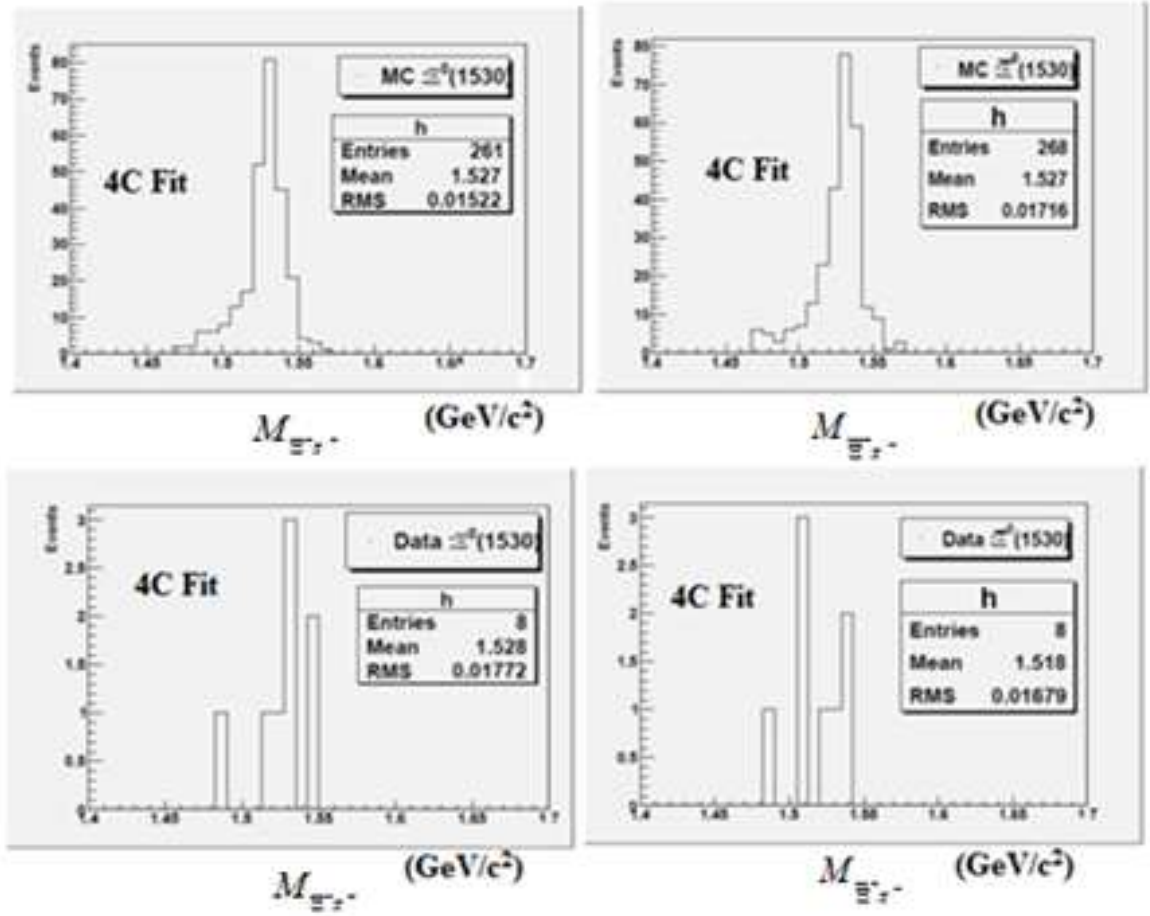


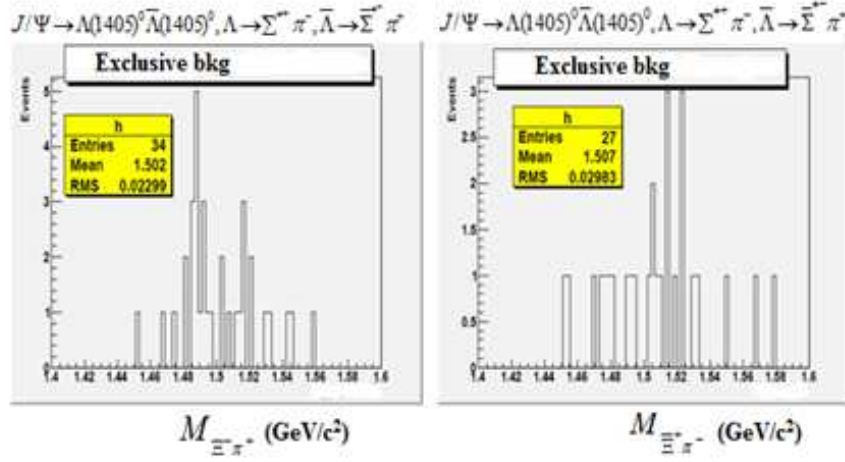
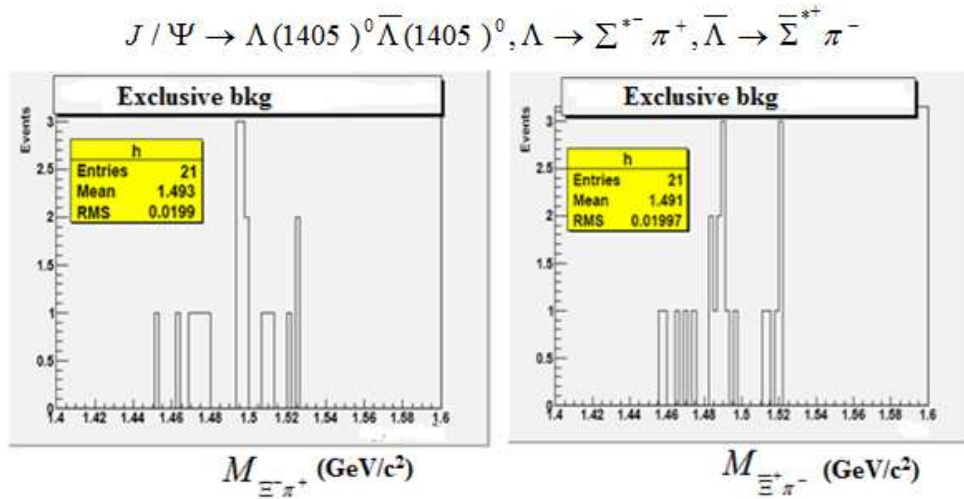
Figure 6.12: MC and data invariant mass distribution for  $\Xi^-\pi^+$  and  $\bar{\Xi}^+\pi^-$  after 4C fit results

## 6.4 Analysis of $\psi(2S) \rightarrow \Xi^0(1530)\bar{\Xi}^0(1530)$

### 6.4.1 Initial Event Selection

This decay channel proceed through the following sequence of event topology:  $\psi(2S) \rightarrow \Xi^0(1530)\bar{\Xi}^0(1530)$ ,  $\Xi^0(1530) \rightarrow \Xi^-\pi^+$ ,  $\Xi^- \rightarrow \Lambda\pi^-$ ,  $\Lambda \rightarrow p\pi^-$  and  $\bar{\Xi}^0(1530) \rightarrow \bar{\Xi}^+\pi^-$ ,  $\bar{\Xi}^+ \rightarrow \bar{\Lambda}\pi^+$ ,  $\bar{\Lambda} \rightarrow \bar{p}\pi^+$ . Hence there are 8 final states charged particles:  $p\bar{p}\pi^+\pi^+\pi^-\pi^-\pi^-\pi^-$ .

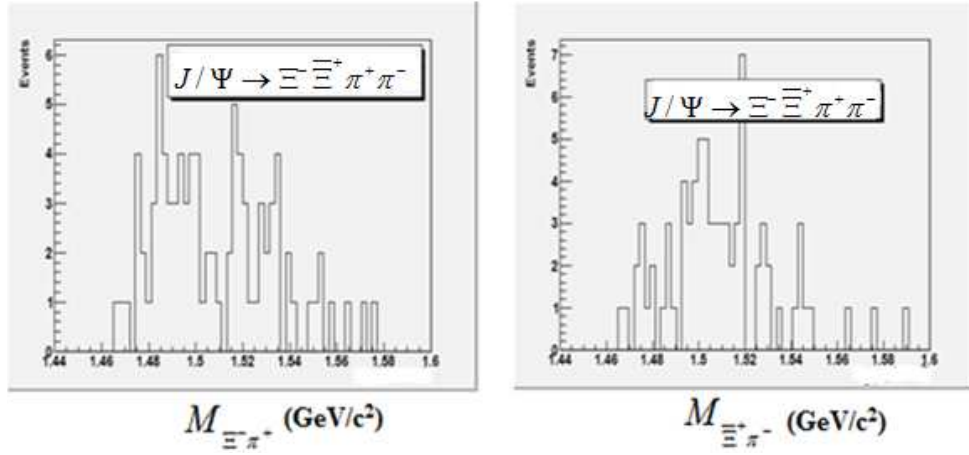
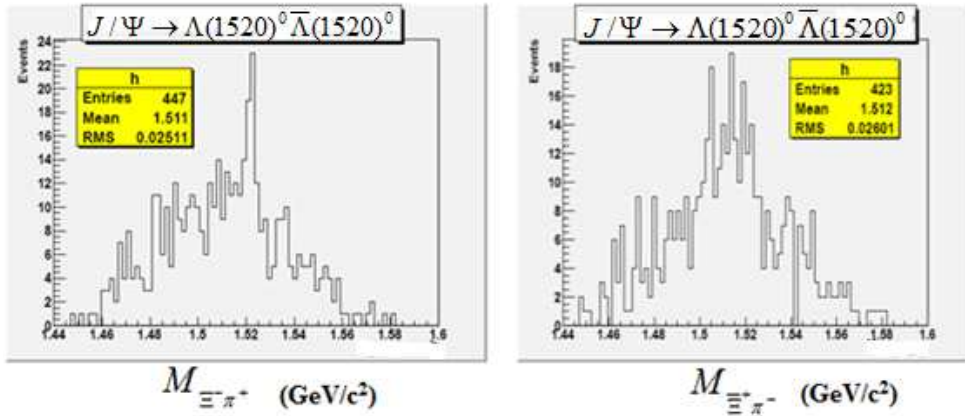
Being analogous to the previous decay channel, the same initial event selection criteria has been applied for this decay channel. Invariant mass distribution plots after kinematic fit are shown below


 Figure 6.13:  $M_{\Xi^- \pi^+}$  and  $M_{\Xi^+ \pi^-}$  distribution

 Figure 6.14:  $M_{\Xi^- \pi^+}$  and  $M_{\Xi^+ \pi^-}$  distribution

## 6.4.2 Final Event Selection

- $\chi^2$  Optimization

In order to get pure signal we further suppress background by optimizing  $\chi^2$ . This is also done so as to enhance the signal to signal plus background ratio i.e.  $\frac{S}{\sqrt{S+B}}$ . Here S is for signal and B for background. For signal MC sample is used and for S+B, data is used. In final event selection we have used optimized  $\chi^2$  for 1C kinematic fit


 Figure 6.15:  $M_{\Xi^-\pi^+}$  and  $M_{\Xi^+\pi^-}$  distribution

 Figure 6.16:  $M_{\Xi^-\pi^+}$  and  $M_{\Xi^+\pi^-}$  distribution

with value 85.

In order to get more refined signal events with possible minimum background we have applied following mass cuts in the range of  $3\sigma$  along with  $\chi^2 < 85$  for the final event selection.

- mass cut for  $p\pi^-$  distribution:  $|M_{p\pi^-} - 1.1156| < 0.012$
- mass cut for  $\bar{p}\pi^+$  distribution:  $|M_{\bar{p}\pi^+} - 1.1156| < 0.012$
- mass cut for  $\Lambda\pi^-$  distribution:  $|M_{\Lambda\pi^-} - 1.321| < 0.018$

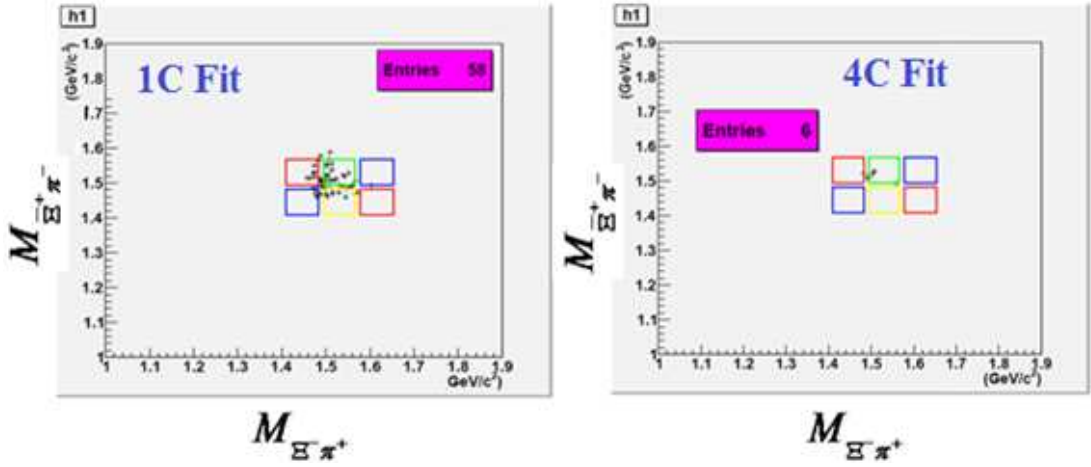


Figure 6.17: Scatter plot of  $M_{\Xi^-\pi^+}$  VS  $M_{\Xi^+\pi^-}$  distribution after 1C and 4C fit results for MC exclusive decay channel  $J/\psi \rightarrow \Lambda^0(1405)\bar{\Lambda}^0(1405)$ , where  $\Lambda^0(1405) \rightarrow \Sigma^{*+}\pi^-$ ,  $\bar{\Lambda}^0(1405) \rightarrow \bar{\Sigma}^{*-}\pi^+$ ,  $\Sigma^{*+} \rightarrow \Lambda\pi^+$ ,  $\Lambda \rightarrow \pi^-p$ ,  $\bar{\Sigma}^{*-} \rightarrow \bar{\Lambda}\pi^-$ ,  $\bar{\Lambda} \rightarrow \bar{p}\pi^+$

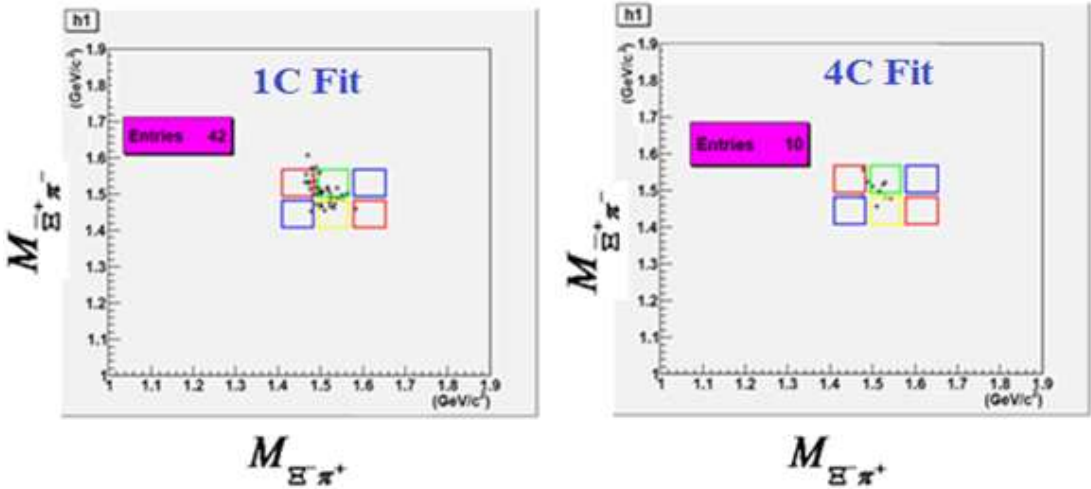


Figure 6.18: Scatter plot of  $M_{\Xi^-\pi^+}$  VS  $M_{\Xi^+\pi^-}$  distribution after 1C and 4C fit results for MC exclusive decay channel  $J/\psi \rightarrow \Lambda^0(1405)\bar{\Lambda}^0(1405)$ , where  $\Lambda^0(1405) \rightarrow \Sigma^{*-}\pi^+$ ,  $\bar{\Lambda}^0(1405) \rightarrow \bar{\Sigma}^{*+}\pi^-$ ,  $\Sigma^{*-} \rightarrow \Lambda\pi^-$ ,  $\Lambda \rightarrow \pi^-p$ ,  $\bar{\Sigma}^{*+} \rightarrow \bar{\Lambda}\pi^+$ ,  $\bar{\Lambda} \rightarrow \bar{p}\pi^+$

- mass cut for  $\bar{\Lambda}\pi^+$  distribution:  $|M_{\bar{\Lambda}\pi^+} - 1.321| < 0.018$
- mass cut for  $\Xi^-\pi^+$  distribution:  $|M_{\Xi^-\pi^+} - 1.531| < 0.03$

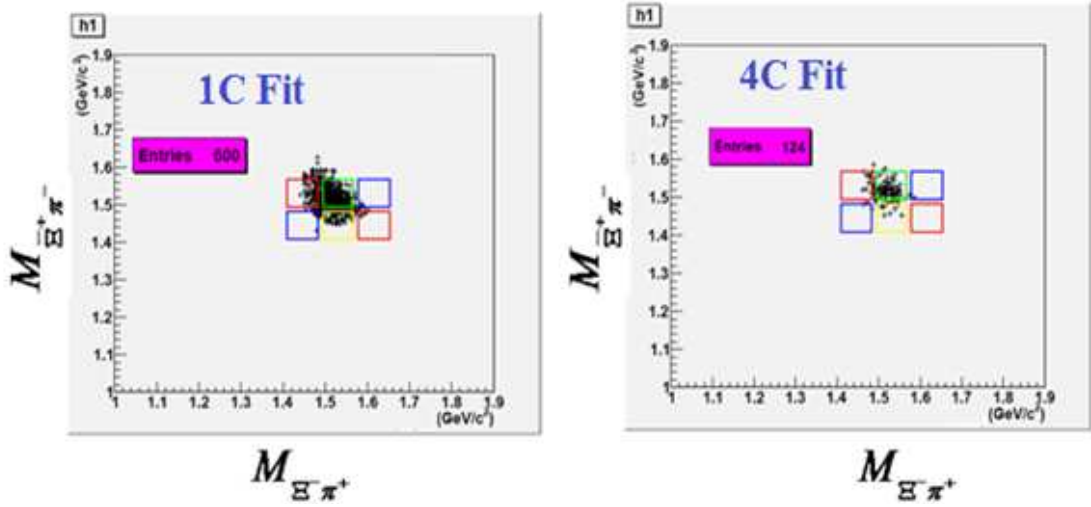


Figure 6.19: Scatter plot of  $M_{\Xi^-\pi^+}$  VS  $M_{\Xi^+\pi^-}$  distribution after 1C and 4C fit results for MC exclusive decay channel  $J/\psi \rightarrow \Xi^-\bar{\Xi}^+\pi^+\pi^-$ , where  $\Xi^- \rightarrow \Lambda\pi^-$ ,  $\Lambda \rightarrow \pi^-p$  and  $\bar{\Xi}^+ \rightarrow \bar{\Lambda}\pi^+$ ,  $\bar{\Lambda} \rightarrow \pi^+\bar{p}$

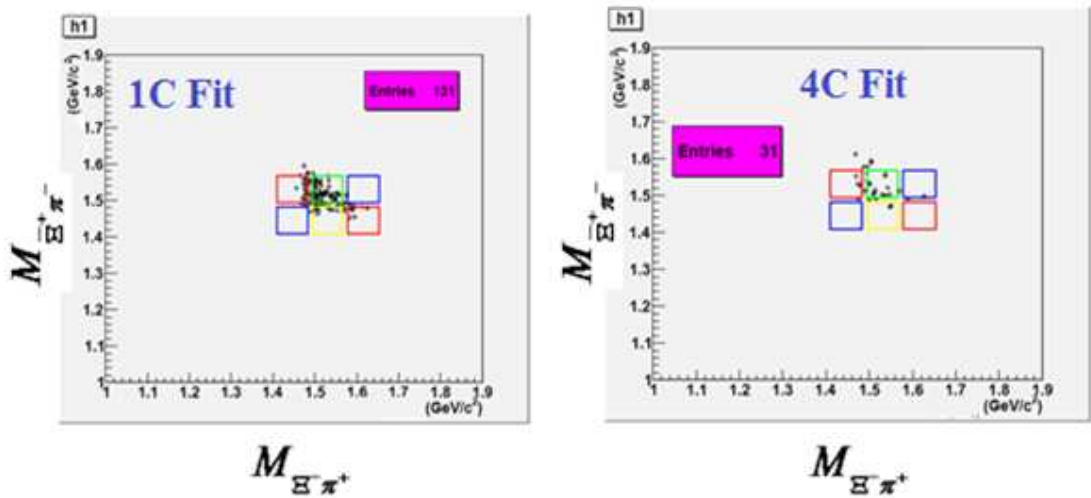


Figure 6.20: Scatter plot of  $M_{\Xi^-\pi^+}$  VS  $M_{\Xi^+\pi^-}$  distribution after 1C and 4C fit results for MC exclusive decay channel  $J/\psi \rightarrow \Lambda^0(1520)\bar{\Lambda}^0(1520)$ , where  $\Lambda^0(1520) \rightarrow \Lambda\pi^+\pi^-$ ,  $\Lambda \rightarrow p\pi^-$ ,  $\bar{\Lambda}^0(1520) \rightarrow \bar{\Lambda}\pi^+\pi^-$ ,  $\bar{\Lambda} \rightarrow \bar{p}\pi^+$ .

- mass cut for  $\bar{\Xi}^+\pi^-$  distribution:  $|M_{\bar{\Xi}^+\pi^-} - 1.531| < 0.03$

In order to reject the events from the background channel found from inclusive MC

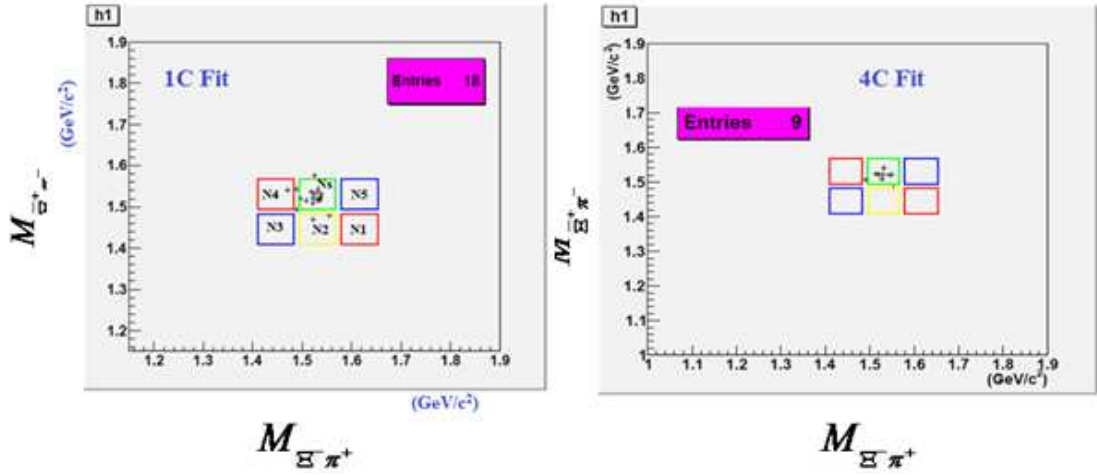


Figure 6.21: Scatter plot of  $\Xi^- \pi^+$  VS  $\Xi^+ \pi^-$  after 1C and 4C fit results for the signal decay channel  $J/\psi \rightarrow \Xi^0(1530)\bar{\Xi}^0(1530)$ .

Error source	(%) error
$p\bar{p}$ PID	2
MC statistics	3.1
MDC tracking	7
MC model	0
Number of $J/\Psi$ events	1.24
Intermediate resonances	1.5
<b>Total</b>	<b>8.15</b>

Table 6.2: Systematic errors from 1C fit results for the signal channel:  $J/\psi \rightarrow \Xi^0(1530)\bar{\Xi}^0(1530)$

background analysis:  $\psi(2S) \rightarrow J/\psi \pi^+ \pi^-$ , where  $J/\psi \rightarrow \Xi^- \bar{\Xi}^+$ ,  $\Xi^- \rightarrow \Lambda \pi^-$ ,  $\Lambda \rightarrow p \pi^-$ ,  $\bar{\Xi}^+ \rightarrow \bar{\Lambda} \pi^+$ ,  $\bar{\Lambda} \rightarrow \bar{p} \pi^+$ , we use the following exclusive mass constraint:

- $|M_{\Xi^- \bar{\Xi}^+} - 3.097| > 0.018$

After relevant final event selection as given above, important MC and data invariant mass distributions are shown below in Figs. 6.22-6.27. While the same MC and data invariant mass distributions after 1C and 4C fits results are shown in Figs. 6.28-6.33.

Error source	(%) error
$p\bar{p}$ PID	2
MC statistics	6.2
MDC tracking	8
MC model	0
Number of $J/\psi$ events	1.24
Intermediate resonances	1.5
<b>Total</b>	<b>10.5</b>

Table 6.3: Systematic errors from 4C fit results for the signal channel:  $J/\psi \rightarrow \Xi^0(1530)\bar{\Xi}^0(1530)$

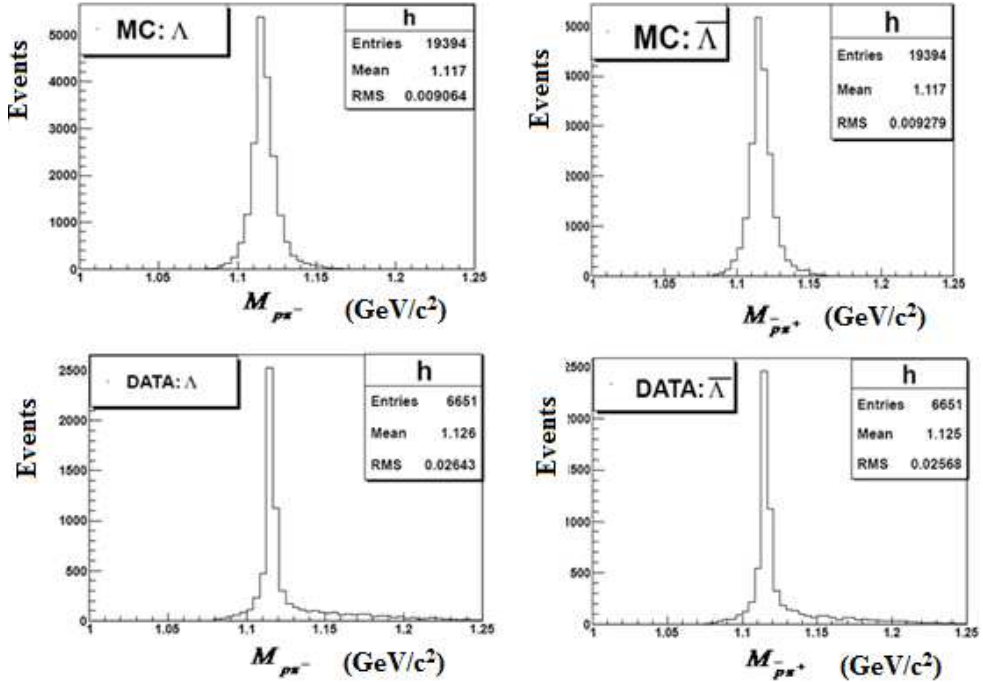


Figure 6.22: MC and data invariant mass distribution for  $p\pi^-$  and  $\bar{p}\pi^+$  after kinematic fit

### 6.4.3 Background Analysis

Background was estimated from exclusive channels, 225 M MC inclusive events and side band region.

#### 1. Background from Inclusive Monte Carlo

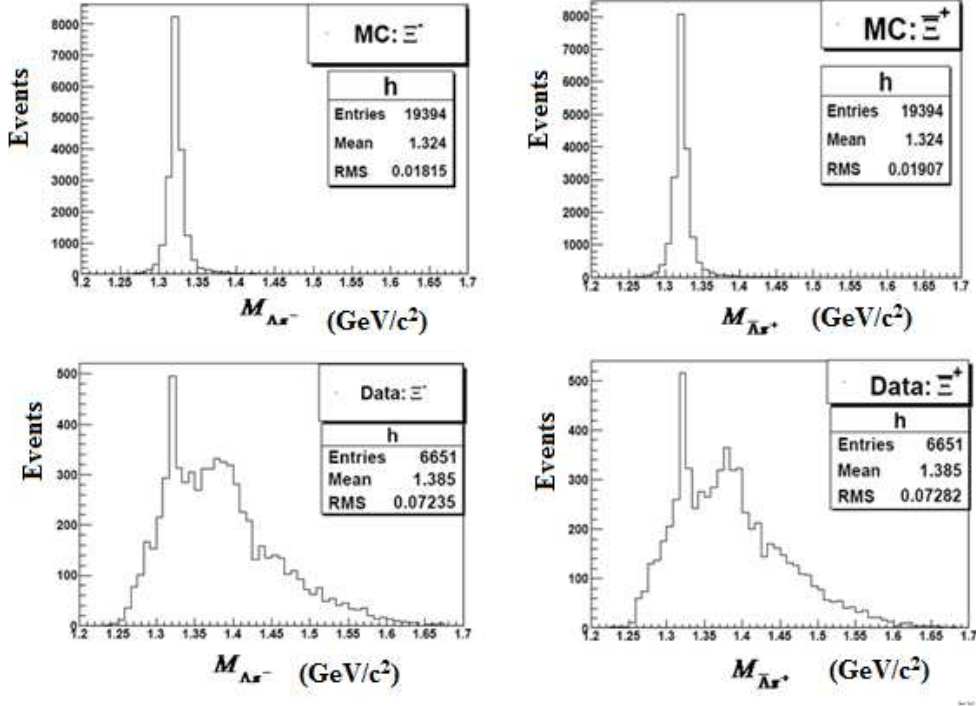


Figure 6.23: MC and data invariant mass distribution for  $\Lambda\pi^-$  and  $\bar{\Lambda}\pi^+$  after kinematic fit

List of background decay channels studied from MC inclusive background is shown in Table 6.4. Background channel from MC inclusive events is  $\psi(2S) \rightarrow J/\psi\pi^+\pi^-$ . After final event selection criteria total 77 events were survived. In order to remove this background exclusive mass cut  $M_{\Xi^-\bar{\Xi}^+} > 0.018\text{GeV}/c^2$  has been used.

## 2. Background from Exclusive Background

For exclusive background, we have generated the following 8 charged tracks channels  $\psi(2S) \rightarrow \Lambda^0(1520)\bar{\Lambda}^0(1520)$ , where  $\Lambda^0(1520) \rightarrow \Lambda\pi^+\pi^-$ ,  $\Lambda \rightarrow p\pi^-$ ,  $\bar{\Lambda}^0(1520) \rightarrow \bar{\Lambda}\pi^+\pi^-$ ,  $\bar{\Lambda} \rightarrow \bar{p}\pi^+$ ;  $\psi(2S) \rightarrow \Lambda^0(1690)\bar{\Lambda}^0(1690)$ , where  $\Lambda^0(1690) \rightarrow \Lambda\pi^+\pi^-$ ,  $\Lambda \rightarrow p\pi^-$ ,  $\bar{\Lambda}^0(1690) \rightarrow \bar{\Lambda}\pi^+\pi^-$ ,  $\bar{\Lambda} \rightarrow \bar{p}\pi^+$ ;  $\psi(2S) \rightarrow \Lambda^0(1520)\bar{\Lambda}^0(1520)$ , where  $\Lambda^0(1520) \rightarrow \Sigma^{*+}\pi^-$ ,  $\bar{\Lambda}^0(1520) \rightarrow \bar{\Sigma}^{*-}\pi^+$ ,  $\Sigma^{*+} \rightarrow \Lambda\pi^+$ ,  $\Lambda \rightarrow \pi^-p$ ,  $\bar{\Sigma}^{*-} \rightarrow \bar{\Lambda}\pi^-$ ,  $\bar{\Lambda} \rightarrow \bar{p}\pi^+$ ;  $\psi(2S) \rightarrow \Lambda^0(1520)\bar{\Lambda}^0(1520)$ , where  $\Lambda^0(1520) \rightarrow \Sigma^{*-}\pi^+$ ,  $\bar{\Lambda}^0(1520) \rightarrow \bar{\Sigma}^{*+}\pi^-$ ,  $\Sigma^{*-} \rightarrow \Lambda\pi^-$ ,  $\Lambda \rightarrow \pi^-p$ ,  $\bar{\Sigma}^{*+} \rightarrow \bar{\Lambda}\pi^+$ ,  $\bar{\Lambda} \rightarrow \bar{p}\pi^+$  and  $\psi(2S) \rightarrow \Xi^-\bar{\Xi}^+\pi^+\pi^-$ , where  $\Xi^- \rightarrow \Lambda\pi^-$ ,  $\Lambda \rightarrow \pi^-p$  and  $\bar{\Xi}^+ \rightarrow \bar{\Lambda}\pi^+$ ,  $\bar{\Lambda} \rightarrow \pi^+\bar{p}$ .

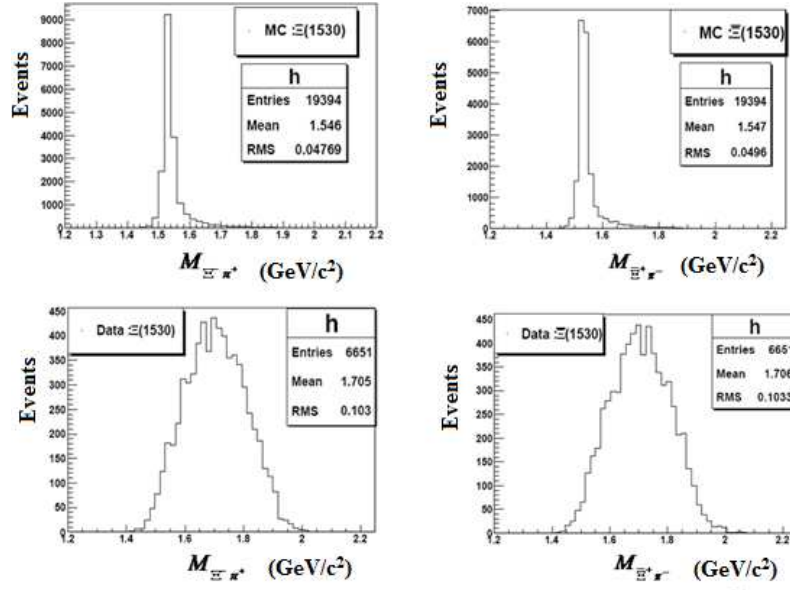


Figure 6.24: MC and data invariant mass distribution for  $\Xi^- \pi^+$  and  $\Xi^+ \pi^-$  after kinematic fit

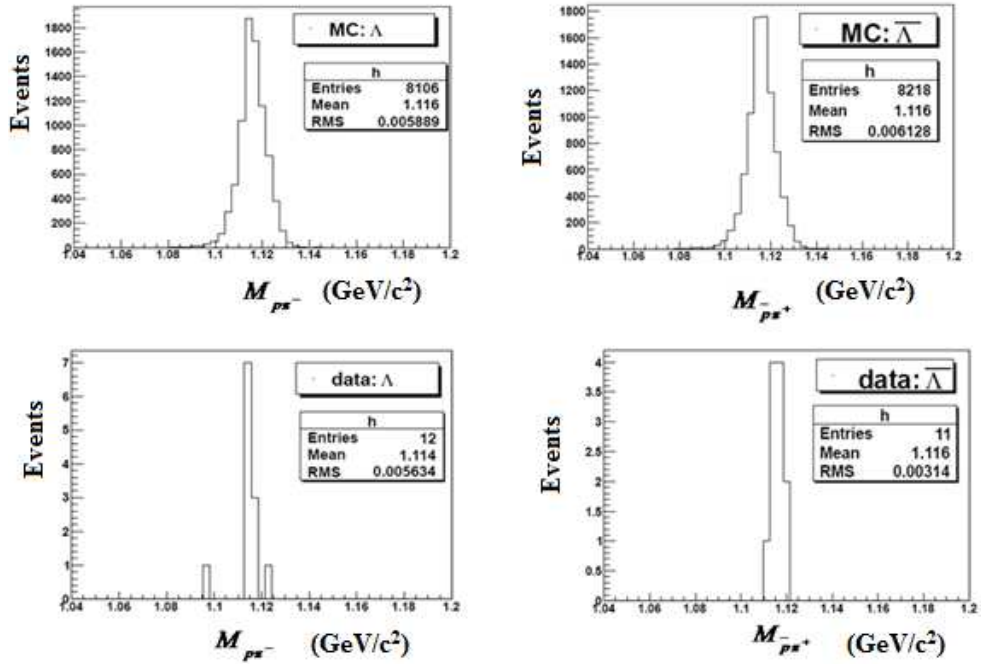


Figure 6.25: MC and data invariant mass distribution for  $p \pi^-$  and  $\bar{p} \pi^+$  after final event selection

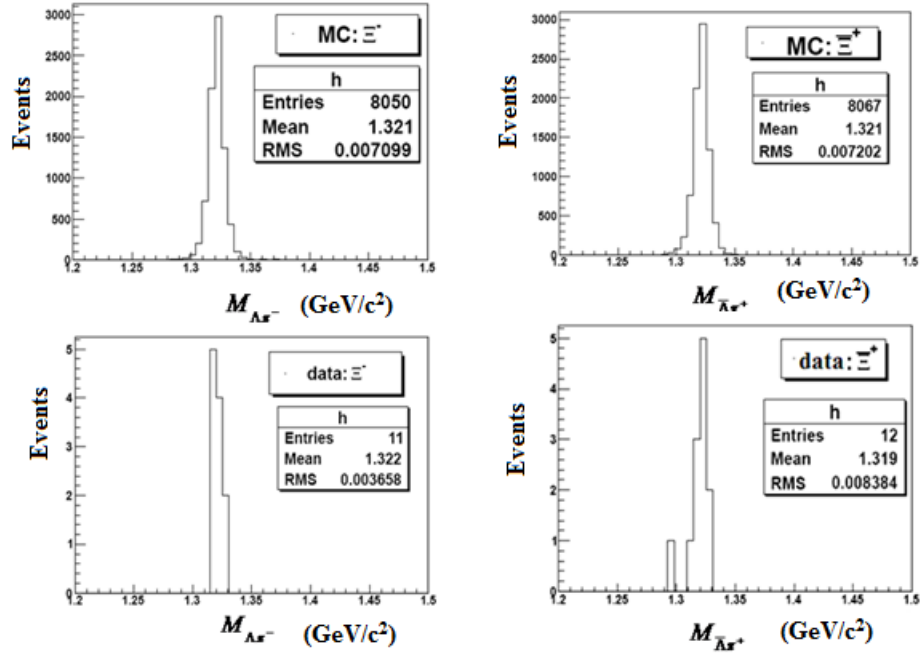


Figure 6.26: MC and data invariant mass distribution for  $\Lambda\pi^-$  and  $\bar{\Lambda}\pi^+$  after final event selection

Invariant mass distributions of  $\Xi^-\pi^+$  and  $\Xi^+\pi^-$  for above mentioned exclusive background decay channels are shown below in Fig. 6.34, Fig. 6.35, Fig. 6.36, Fig. 6.37 and Fig. 6.38 respectively.

Now scatter plots for the above mentioned decay channels are shown in the Figs. 6.39-6.43. The green box shows the signal region while other boxes represent the side band region.

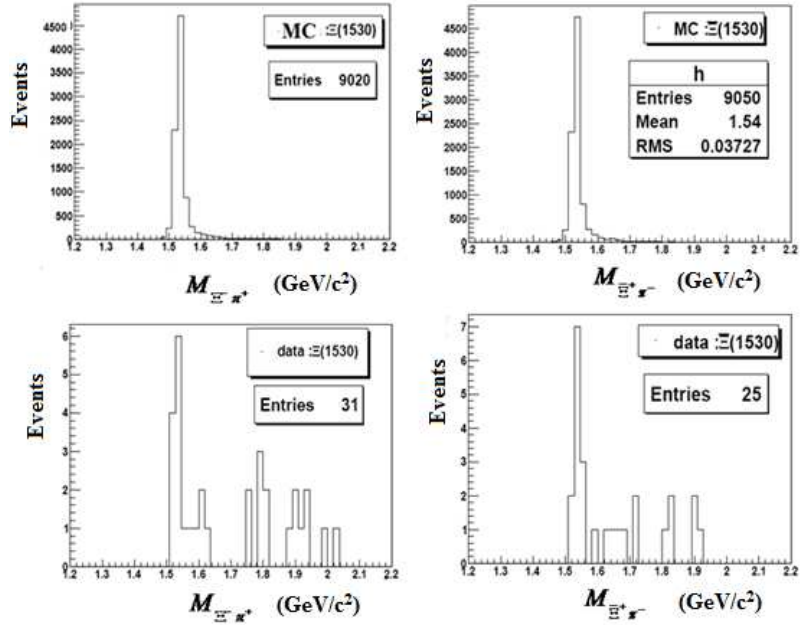


Figure 6.27: MC and data invariant mass distribution for  $\Xi^- \pi^+$  and  $\Xi^+ \pi^-$  after final event selection

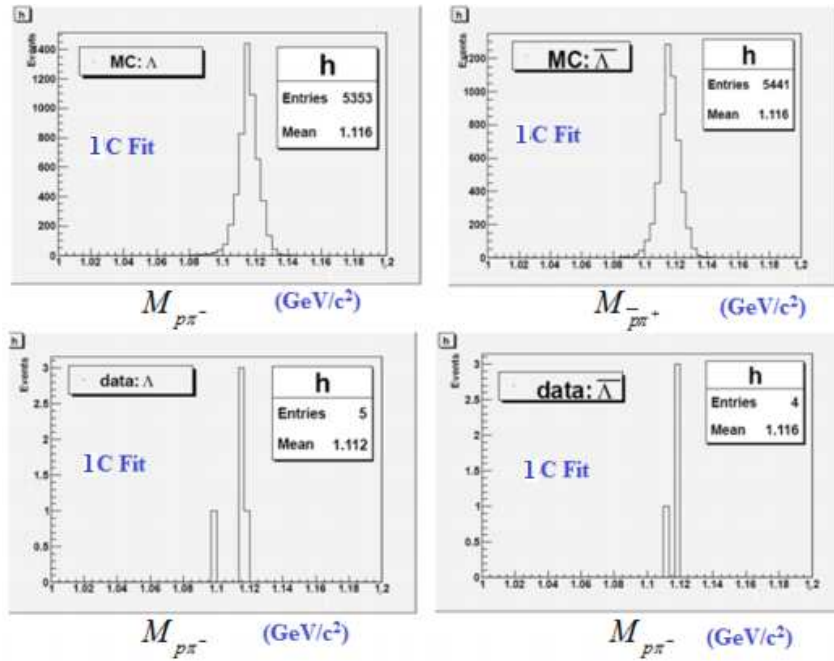


Figure 6.28: MC and data invariant mass spectra for  $p\pi^-$  and  $\bar{p}\pi^+$  after 1C fit results.

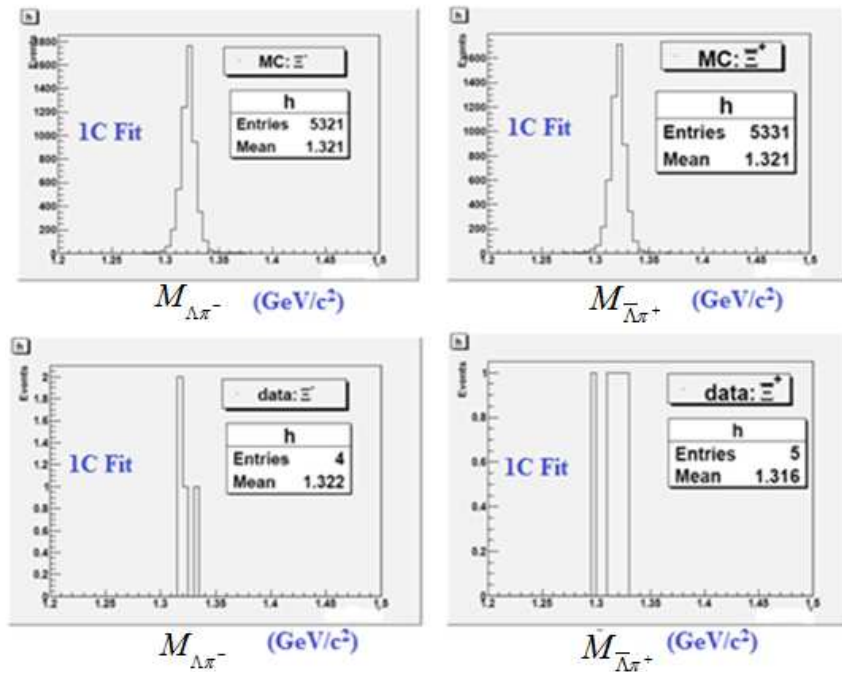


Figure 6.29: MC and data invariant mass spectra for  $\Lambda\pi^-$  and  $\bar{\Lambda}\pi^+$  after 1C fit results.

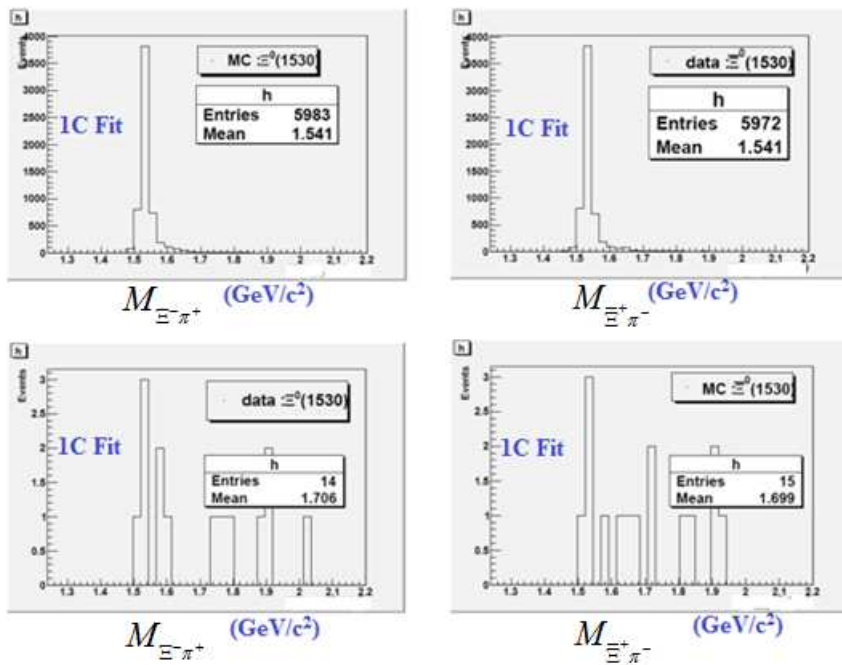


Figure 6.30: MC and data invariant mass spectra for  $\Xi^-\pi^+$  and  $\Xi^+\pi^-$  after 1C fit results.

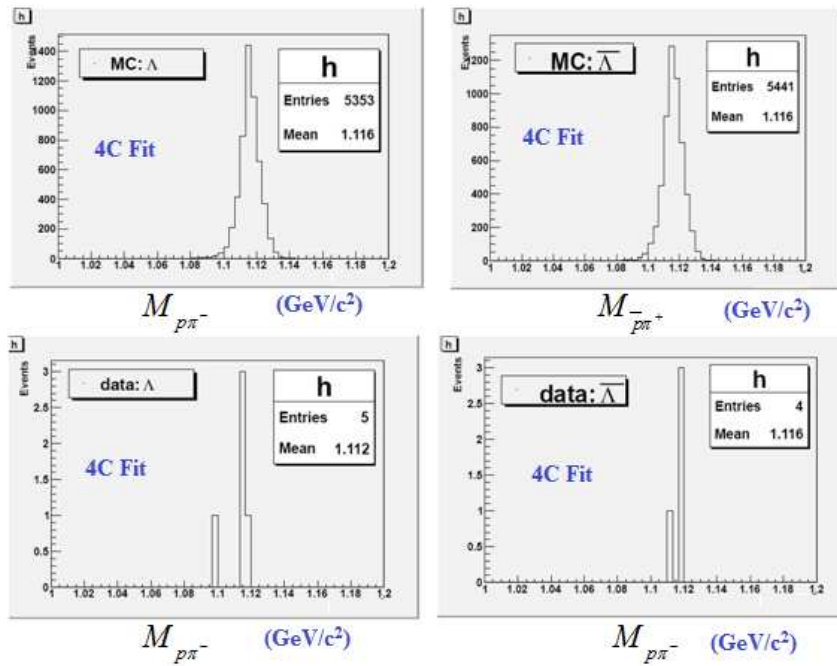


Figure 6.31: MC and data invariant mass spectra for  $p\pi^-$  and  $\bar{p}\pi^+$  after 4C fit results.

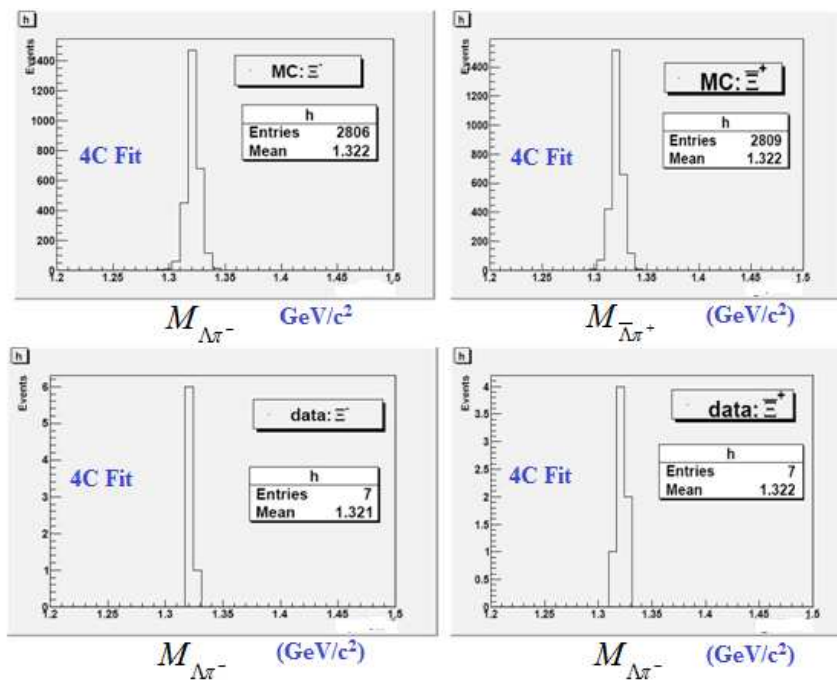


Figure 6.32: MC and data invariant mass spectra for  $\Lambda\pi^-$  and  $\bar{\Lambda}\pi^+$  after 4C fit results.

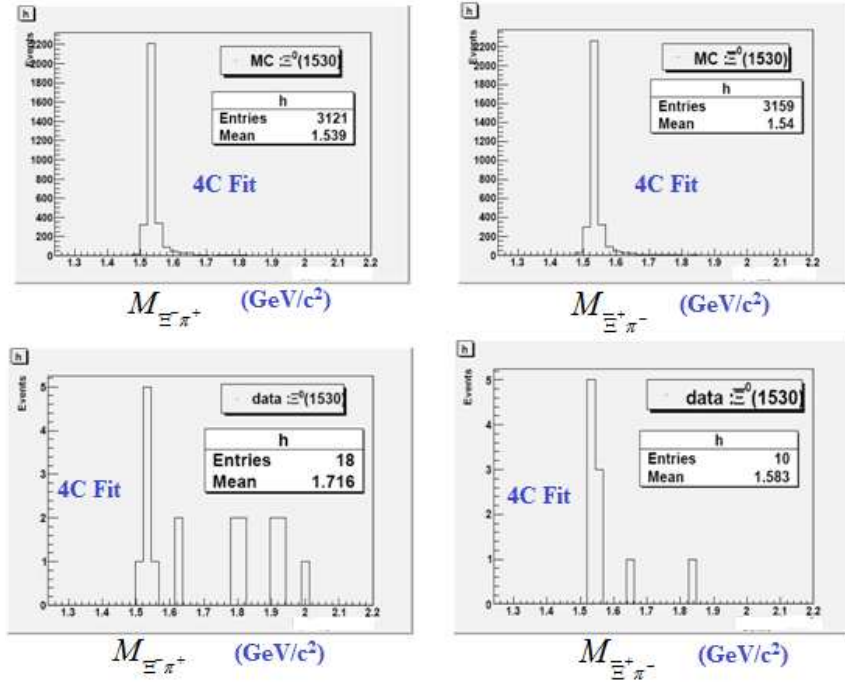


Figure 6.33: MC and data invariant mass spectra for  $\Xi^-\pi^+$  and  $\Xi^+\pi^-$  after 4c fit results.

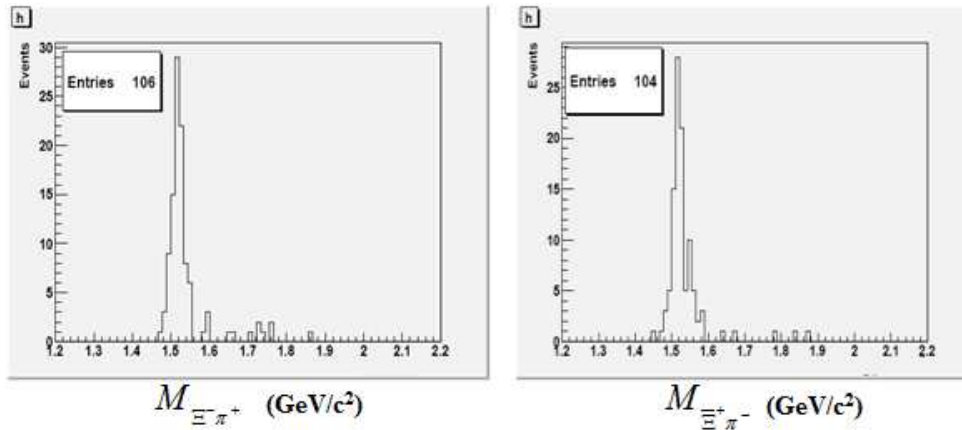


Figure 6.34: Invariant mass spectrum of  $\Xi(1530)^0$  and  $\bar{\Xi}(1530)^0$  for MC exclusive background decay channel  $\psi(2S) \rightarrow \Lambda(1520)\bar{\Lambda}(1520)$

### 3. Background from Sideband Region

The two dimensional scatter plot of  $\Xi^0 1530$  Vs  $\bar{\Xi}^0(1530)$  is shown in Fig. 6.44. Background is estimated from side band boxes  $0.008 \text{ GeV}/c^2$  away from signal box. Signal and

No	Decay Channel	Final states	$N_{\text{Evt}}$
1	$\Psi(2S) \rightarrow J/\Psi \pi^+ \pi^-, J/\Psi \rightarrow \Xi^- \bar{\Xi}^+$ $\Xi^- \rightarrow \Lambda \pi^-, \Lambda \rightarrow p \pi^-, \bar{\Xi}^+ \rightarrow \bar{\Lambda} \pi^+, \bar{\Lambda} \rightarrow \bar{p} \pi^+$	$p \bar{p} \pi^+ \pi^+ \pi^+$ $\pi^- \pi^- \pi^-$	77
2	$\Psi(2S) \rightarrow J/\Psi \pi^+ \pi^-, J/\Psi \rightarrow \bar{\Sigma}^-(1385) \Sigma^+(1385)$ $\bar{\Sigma}^-(1385) \rightarrow \bar{\Lambda} \pi^-, \bar{\Lambda} \rightarrow \bar{p} \pi^+$ $\Sigma^+(1385) \rightarrow \Lambda \pi^+, \Lambda \rightarrow p \pi^-$	$p \bar{p} \pi^+ \pi^+ \pi^+$ $\pi^- \pi^- \pi^-$	1
3	$\Psi(2S) \rightarrow J/\Psi \pi^+ \pi^-, J/\Psi \rightarrow \bar{\Sigma}^+(1385) \Sigma^-(1385)$ $\bar{\Sigma}^+(1385) \rightarrow \bar{\Lambda} \pi^+, \bar{\Lambda} \rightarrow \bar{p} \pi^+$ $\Sigma^-(1385) \rightarrow \Lambda \pi^-, \Lambda \rightarrow p \pi^-$	$p \bar{p} \pi^+ \pi^+ \pi^+$ $\pi^- \pi^- \pi^-$	0
4	$\Psi(2S) \rightarrow J/\Psi \pi^+ \pi^-, J/\Psi \rightarrow \bar{\Sigma}^+(1385) \Lambda \pi^-$ $\bar{\Sigma}^+(1385) \rightarrow \bar{\Lambda} \pi^+, \bar{\Lambda} \rightarrow \bar{p} \pi^+, \Lambda \rightarrow p \pi^-$	$p \bar{p} \pi^+ \pi^+ \pi^+$ $\pi^- \pi^- \pi^-$	0
5	$\Psi(2S) \rightarrow J/\Psi \pi^+ \pi^-, J/\Psi \rightarrow \bar{\Sigma}^-(1385) \pi^+ \Lambda$ $\bar{\Sigma}^-(1385) \rightarrow \bar{\Lambda} \pi^-, \bar{\Lambda} \rightarrow \bar{p} \pi^+, \Lambda \rightarrow p \pi^-$	$p \bar{p} \pi^+ \pi^+ \pi^+$ $\pi^- \pi^- \pi^-$	0
6	$\Psi(2S) \rightarrow J/\Psi \pi^+ \pi^-, J/\Psi \rightarrow \pi^+ \bar{p} f_0' \pi^+ \pi^- \pi^+ \pi^-$	$p \bar{p} \pi^+ \pi^+ \pi^+ \pi^- \pi^- \pi^-$	0

Table 6.4: MC inclusive background decay modes for the signal channel:  $\psi(2S) \rightarrow \Xi^0(1530) \bar{\Xi}^0(1530)$

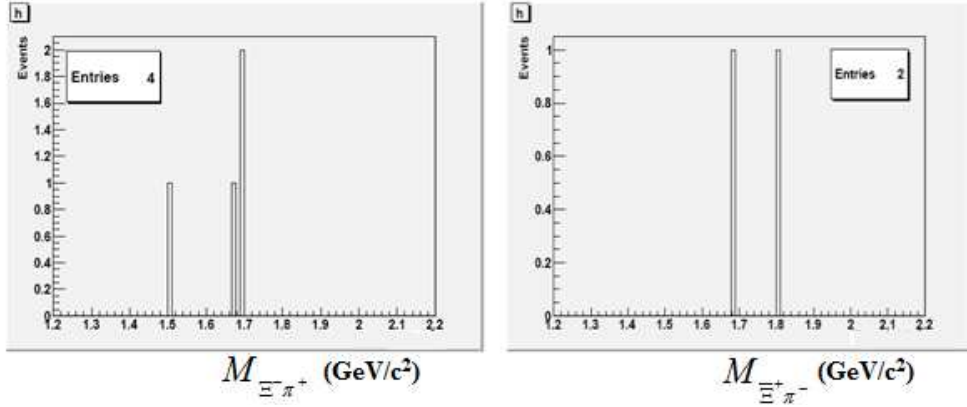


Figure 6.35: Invariant mass spectrum of  $\Xi^0(1530)$  and  $\bar{\Xi}^0(1530)$  for MC exclusive background decay channel  $\psi(2S) \rightarrow \Lambda^0(1690) \bar{\Lambda}^0(1690)$

side bands have width of  $6\sigma$  i.e.  $0.05 \text{ GeV}/c^2$ . Range of  $\Xi^0(1530)$ ,  $|M_{\Xi^-\pi^+} - 1.531| < 0.025$  is for signal box (1.5065, 1.5571). Range for side bands N4 and N5 is  $1.4485 < |M_{\Xi^-\pi^+}| <$

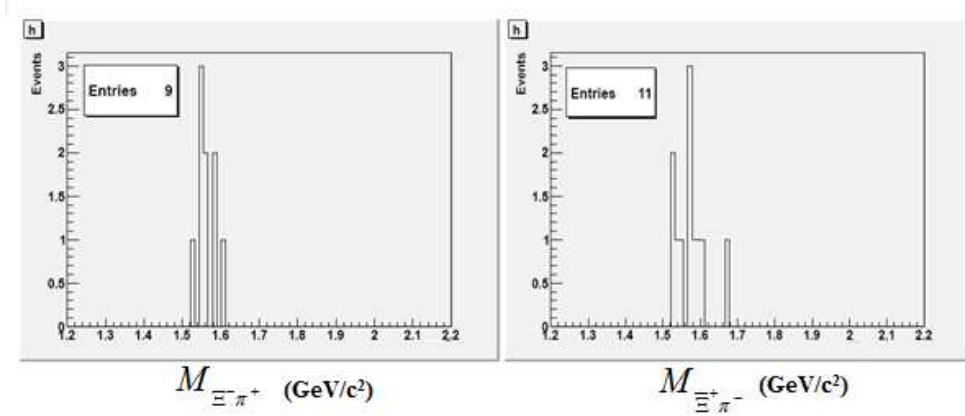


Figure 6.36: Invariant mass spectrum of  $\Xi^0(1530)$  and  $\bar{\Xi}^0(1530)$  for MC exclusive background decay channel  $\psi(2S) \rightarrow \Lambda^0(1520)\bar{\Lambda}^0(1520)$  where  $\Lambda^0(1520) \rightarrow \Sigma^{*+}\pi^-$ ,  $\bar{\Lambda}^0(1520) \rightarrow \bar{\Sigma}^{*-}\pi^+$ ,  $\Sigma^{*+} \rightarrow \Lambda\pi^+$ ,  $\Lambda \rightarrow \pi^-p$ ,  $\bar{\Sigma}^{*-} \rightarrow \bar{\Lambda}\pi^-$ ,  $\bar{\Lambda} \rightarrow \bar{p}\pi^+$

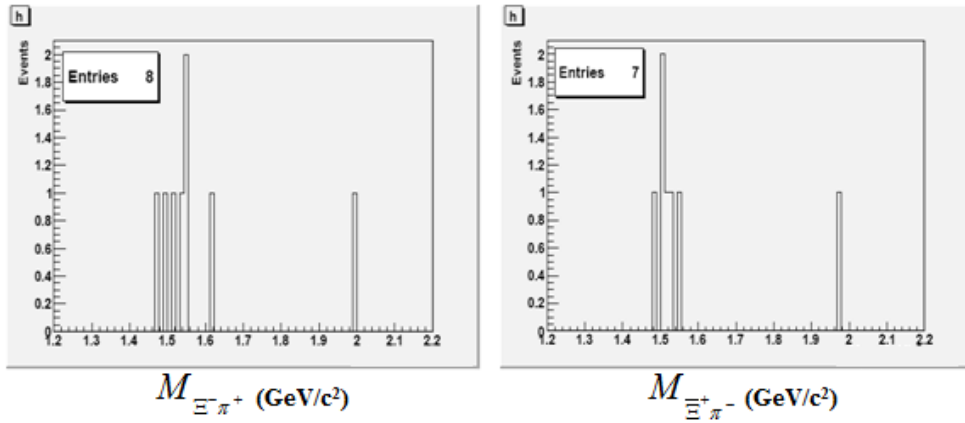


Figure 6.37: Invariant mass spectrum of  $\Xi^0(1530)$  and  $\bar{\Xi}^0(1530)$  for MC exclusive background decay channel  $\psi(2S) \rightarrow \Lambda^0(1520)\bar{\Lambda}^0(1520)$ , where  $\Lambda^0(1520) \rightarrow \Sigma^{*-}\pi^+$ ,  $\bar{\Lambda}^0(1520) \rightarrow \bar{\Sigma}^{*+}\pi^-$ ,  $\Sigma^{*-} \rightarrow \Lambda\pi^-$ ,  $\Lambda \rightarrow \pi^-p$ ,  $\bar{\Sigma}^{*+} \rightarrow \bar{\Lambda}\pi^+$ ,  $\bar{\Lambda} \rightarrow \bar{p}\pi^+$

1.4985 and  $1.5655 < |M_{\Xi^-\pi^+}| < 1.6160$  respectively. Range of  $\bar{\Xi}^0(1530)$ ,  $|M_{\bar{\Xi}^+\pi^-} - 1.531| < 0.025$  is for signal box (1.5065, 1.5571). Range for side bands is  $1.5655 < |M_{\bar{\Xi}^+\pi^-}| < 1.6160$ . Now background events are estimated as  $0.5(N1 + N3 - N4 - N5) + N2 = 1.5$ , number of signal events in signal region S are 11, hence number of observed events are 9.5.

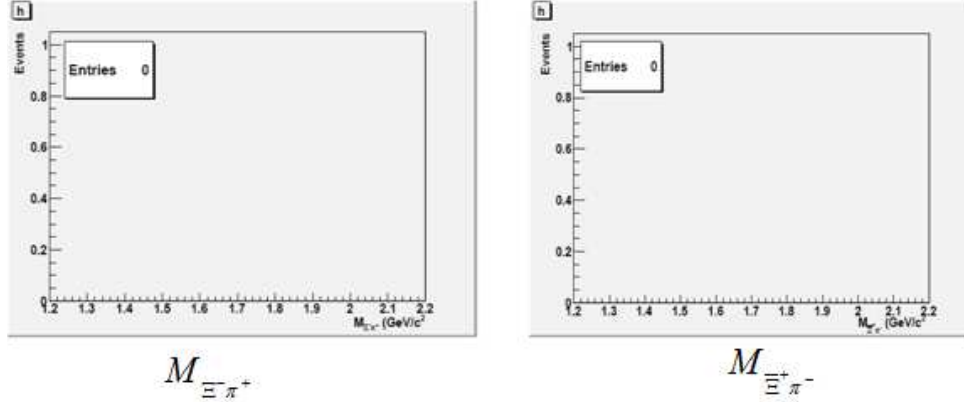


Figure 6.38: Invariant mass spectrum of  $\Xi^0(1530)$  and  $\bar{\Xi}^0(1530)$  for MC exclusive background decay channel  $\psi(2S) \rightarrow \Xi^-\bar{\Xi}^+\pi^+\pi^-$

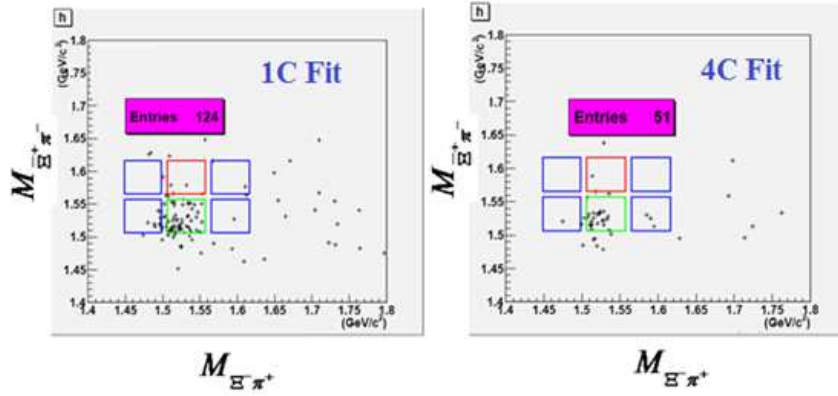


Figure 6.39: Scatter plot of  $M_{\Xi^-\pi^+}$  VS  $M_{\bar{\Xi}^+\pi^-}$  distribution for MC exclusive decay channel  $\psi(2S) \rightarrow \Lambda^0(1520)\bar{\Lambda}^0(1520)$ , where  $\Lambda^0(1520) \rightarrow \Lambda\pi^+\pi^-$ ,  $\Lambda \rightarrow p\pi^-$ ,  $\bar{\Lambda}^0(1520) \rightarrow \bar{\Lambda}\pi^+\pi^-$ ,  $\bar{\Lambda} \rightarrow \bar{p}\pi^+$

#### 6.4.4 Determination of Branching Fraction

Branching ration for the decay channel  $\psi(2S) \rightarrow \Xi^0(1530)\bar{\Xi}^0(1530)$  is measured using the formula:

$$Br[\psi(2S) \rightarrow \Xi^0(1530)\bar{\Xi}^0(1530)] = \frac{N^{obs}}{\epsilon \cdot N^{J/\psi} \cdot Br[\Lambda \rightarrow p\pi^-]^2 \cdot Br[\Xi^- \rightarrow \Lambda\pi^-]^2}$$

Where number of observed events  $N^{obs}$  for 1C and 4C fits are  $3 \pm 2$  and  $7 \pm 2.6$  respectively, total number of  $\psi(2S)$  events  $N^{\psi(2S)}$  are  $(106 \times 10^6)$ , branching fraction of inter-

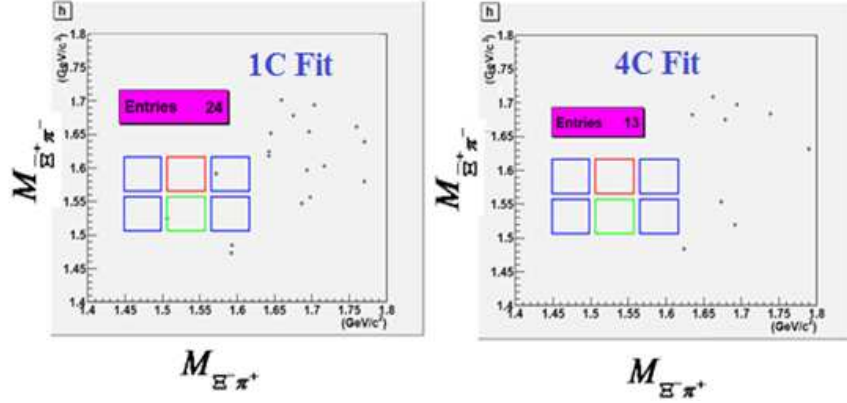


Figure 6.40: Scatter plot of  $M_{\Xi^-\pi^+}$  VS  $M_{\Xi^+\pi^-}$  distribution for MC exclusive background decay channel  $\psi(2S) \rightarrow \Lambda^0(1690)\bar{\Lambda}^0(1690)$ , where  $\Lambda^0(1690) \rightarrow \Lambda\pi^+\pi^-$ ,  $\Lambda \rightarrow p\pi^-$ ,  $\bar{\Lambda}^0(1690) \rightarrow \bar{\Lambda}\pi^+\pi^-$ ,  $\bar{\Lambda} \rightarrow \bar{p}\pi^+$ .

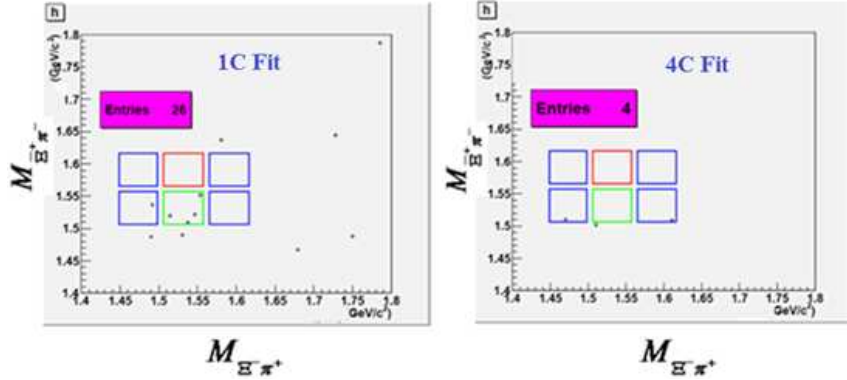


Figure 6.41: Scatter plot of  $M_{\Xi^-\pi^+}$  VS  $M_{\Xi^+\pi^-}$  distribution for MC exclusive background decay channel  $\psi(2S) \rightarrow \Lambda^0(1520)\bar{\Lambda}^0(1520)$ , where  $\Lambda^0(1520) \rightarrow \Sigma^{*+}\pi^-$ ,  $\bar{\Lambda}^0(1520) \rightarrow \bar{\Sigma}^{*-}\pi^+$ ,  $\Sigma^{*+} \rightarrow \Lambda\pi^+$ ,  $\Lambda \rightarrow \pi^-p$ ,  $\bar{\Sigma}^{*-} \rightarrow \bar{\Lambda}\pi^-$ ,  $\bar{\Lambda} \rightarrow \bar{p}\pi^+$

mediate resonances are  $\text{Br}[\Lambda \rightarrow p\pi^-] = (0.639 \pm 0.5)\%$  and  $\text{Br}[\Xi^- \rightarrow \Lambda\psi^-] = (0.9987 \pm 0.035)\%$  [87]. MC % efficiency for 1C fit results is determined to be 5.98 %, while MC % efficiency for 4C fit results is determined to be 3.14%. The overall detection efficiency for 1C and 4C fit results for the signal channel  $\psi(2S) \rightarrow \Xi^0(1530)\bar{\Xi}^0(1530)$  is 9.12 %. Now branching ratios for 1C and 4C fit results are determined to be  $(1.16 \pm 0.77_{sys} \pm 0.07_{stat}) \times 10^{-6}$

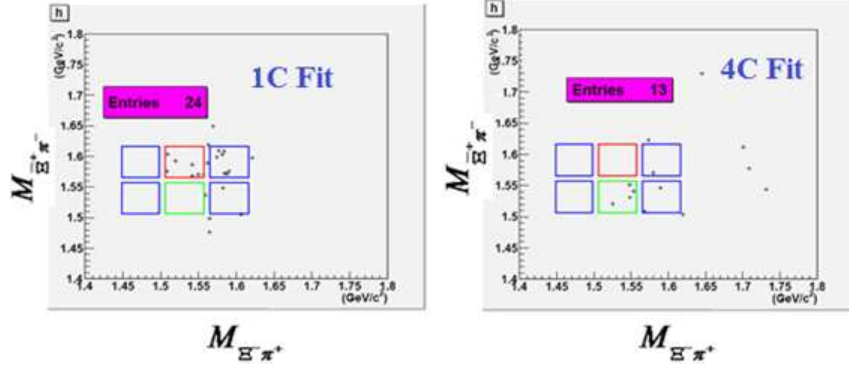


Figure 6.42: Scatter plot of  $M_{\Xi^-\pi^+}$  VS  $M_{\Xi^+\pi^-}$  distribution for MC exclusive background decay channel  $\psi(2S) \rightarrow \Lambda^0(1520)\bar{\Lambda}^0(1520)$ , where  $\Lambda^0(1520) \rightarrow \Sigma^{*-}\pi^+$ ,  $\bar{\Lambda}^0(1520) \rightarrow \bar{\Sigma}^{*+}\pi^-$ ,  $\Sigma^{*-} \rightarrow \Lambda\pi^-$ ,  $\Lambda \rightarrow \pi^-p$ ,  $\bar{\Sigma}^{*+} \rightarrow \bar{\Lambda}\pi^+$ ,  $\bar{\Lambda} \rightarrow \bar{p}\pi^+$

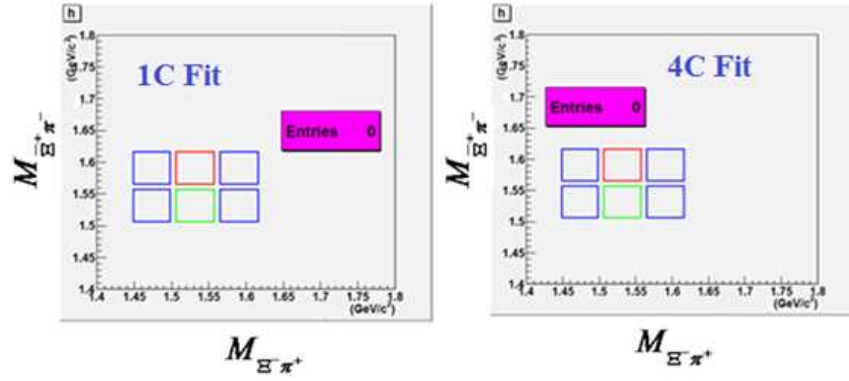


Figure 6.43: Scatter plot of  $M_{\Xi^-\pi^+}$  VS  $M_{\Xi^+\pi^-}$  distribution for MC exclusive background decay channel  $\psi(2S) \rightarrow \Xi^-\bar{\Xi}^+\pi^+\pi^-$ , where  $\Xi^- \rightarrow \Lambda\pi^-$ ,  $\Lambda \rightarrow \pi^-p$  and  $\bar{\Xi}^+ \rightarrow \bar{\Lambda}\pi^+$ ,  $\bar{\Lambda} \rightarrow \pi^+\bar{p}$ .

and  $(5.16 \pm 1.92_{sys} \pm 0.17_{stat}) \times 10^{-5}$  respectively which are consistent within  $2\sigma$ .

## 6.4.5 Systematic Error Analysis

### 1. Particle Identification.

The systematic error due to particle identification is taken as 1% each for proton and anti-proton from the Ref. [79]. So total systematic error from this source is 2%.

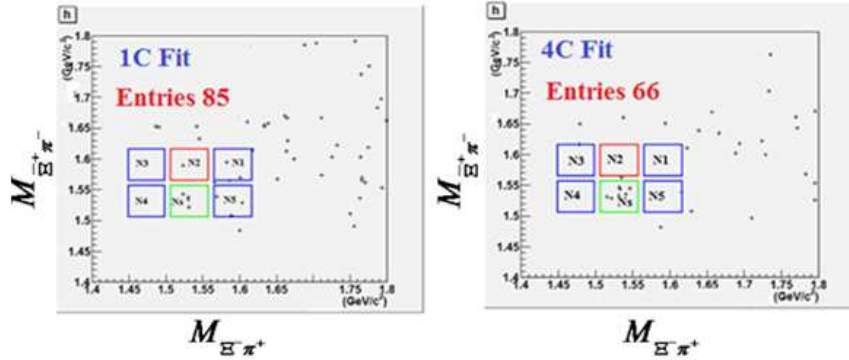


Figure 6.44: Scatter plots of  $\Xi^- \pi^+$  vs  $\Xi^+ \pi^-$  after 1C and 4C fit results for the signal channel  $\psi(2S) \rightarrow \Xi^0(1530)\bar{\Xi}^0(1530)$ .

## 2. MDC Tracking.

The systematic error due to MDC tracking detection efficiency is taken as 1% for each charged track as calculated in Ref. [79]. As there are 8 charged tracks in the final states, so systematic error from this source is taken as 8% for 4C tracking and 7% for 1C tracking.

**3. Total Number of  $\psi(2S)$  Events.** Systematic error from  $(225.3 \pm 2.8)10^6$  number of  $J/\psi$  events is 1.24 % [89].

**4. Error from MC Model.** PHSP MC sample was generated and MC detection efficiency was compared with J2BB2 sample. Relative error in MC detection efficiency is determined to be 0 %.

## 5. Monte Carlo Statistical Error

The monte carlo statistical error for 1C and 4C fit results was estimated by using the respective detection efficiencies and the total number of events of the signal channel  $\psi(2S) \rightarrow \Xi^0(1530)\bar{\Xi}^0(1530)$ , generated by J2BB2 generator, in the relation [44]

MC Statistical Error =  $\frac{\Delta\epsilon}{\epsilon} = \frac{\sqrt{\frac{\epsilon(1-\epsilon)}{N_{gen}}}}{\epsilon}$ . Where  $\epsilon$  and  $N_{gen}$  represent the detection efficiency and total number of signal MC generated events. Using the value of detection efficiencies for 1C and 4C kinematic fit results, the monte carlo statistical errors for 1C and 4C fit results are 1.25% and 1.76% respectively.

### 6. Error from Intermediate Resonances.

Systematic Error due to branching ratio of intermediate resonances [87] is calculated to be 1.5%:

$$\text{Br}[\Lambda/\bar{\Lambda} \rightarrow \pi^- p/\pi^+ \bar{p}] = (63.9 \pm 0.5)\%$$

$$\text{Br}[\Xi^-/\bar{\Xi}^+ \rightarrow \Lambda\pi^-/\bar{\Lambda}\pi^+] = (99.89 \pm 0.035)\%.$$

Therefore the system error in branching fraction from this source is 1.5%.

Now the total systematic error for 1C and 4C fit results is shown below in Table 6.5 and Table 6.6 respectively.

Error source	% error
$p\bar{p}$ PID	2
MDC tracking	7
MC Statistics	1.2
MC model	2.4
Number of $\Psi(2S)$ events	4
Intermediate resonances	1.5
<b>Total</b>	<b>8.86</b>

Table 6.5: Systematic errors from 1C fit results for the signal channel:  $\psi(2S) \rightarrow \Xi^0(1530)\bar{\Xi}^0(1530)$

Error source	% error
$p\bar{p}$ PID	2
MDC tracking	8
MC Statistics	1.76
MC model	2.4
Number of $\Psi(2S)$ events	4
Intermediate resonances	1.5
<b>Total</b>	<b>9.75</b>

Table 6.6: Systematic results from 4C fit results for the signal channel:  $\psi(2S) \rightarrow \Xi^0(1530)\bar{\Xi}^0(1530)$

After incorporating systematic error branching ratios for 1c and 4C fit results are given by:

$$Br^{1C}[\psi(2S) \rightarrow \Xi^0(1530)\bar{\Xi}^0(1530)]=(1.16 \pm 0.77_{sys} \pm 0.07_{stat}) \times 10^{-6}$$

and

$$Br^{4C}[\psi(2S) \rightarrow \Xi^0(1530)\bar{\Xi}^0(1530)]=(5.16 \pm 1.92 \pm 0.17_{stat}) \times 10^{-6}.$$

# Chapter 7

## Summary and Conclusion

Based on world's largest data samples registered by BESIII detector at BEPCII: about 225 million and 106 million for  $J/\psi$  and  $\psi(2S)$ , respectively, the branching ratios for the decay channels  $(J/\psi, \psi(2S)) \rightarrow \Xi^0(1530)\bar{\Xi}^0(1530)$ , where  $\Xi^0(1530) \rightarrow \Xi^-\pi^+, \Xi^- \rightarrow \Lambda\pi^-, \Lambda \rightarrow p\pi^-$  and  $\bar{\Xi}^0(1530) \rightarrow \bar{\Xi}^+\pi^-, \bar{\Xi}^+ \rightarrow \bar{\Lambda}\pi^+, \bar{\Lambda} \rightarrow \bar{p}\pi^+$  are first time determined to be:

$$Br^{1C}[J/\psi \rightarrow \Xi^0(1530)\bar{\Xi}^0(1530)] = (1.06 \pm 0.07_{sys} \pm 0.37_{stat}) \times 10^{-5}$$

$$Br^{4C}[J/\psi \rightarrow \Xi^0(1530)\bar{\Xi}^0(1530)] = (2.94 \pm 0.06_{sys} \pm 1.10_{stat}) \times 10^{-5}.$$

$$Br^{1C}[\psi(2S) \rightarrow \Xi^0(1530)\bar{\Xi}^0(1530)] = (1.16 \pm 0.77_{sys} \pm 0.07_{stat}) \times 10^{-6}$$

$$Br^{4C}[\psi(2S) \rightarrow \Xi^0(1530)\bar{\Xi}^0(1530)] = (5.16 \pm 1.92_{sys} \pm 0.17_{stat}) \times 10^{-6}.$$

These results are consistence within  $2\sigma$ . We also tested the 12 % rule:

$$Q = \frac{Br^{1C}(\psi(2S) \rightarrow B\bar{B})}{Br^{1C}(J/\psi \rightarrow B\bar{B})} = 11\%$$

$$Q = \frac{Br^{4C}(\psi(2S) \rightarrow B\bar{B})}{Br^{4C}(J/\psi \rightarrow B\bar{B})} = 17.55 \%$$

This work can be concluded as follows:

- The technique of using events with one missing particle from the final state greatly improves the detection efficiency with better signal to signal plus background ratio. The improvement of the detection efficiency thus enabled us to measure first time the branching ratios of the discussed decay channels.
- The analysis results can be determined more precisely by using better analysis soft-

ware components such as Monte-Carlo event generators and decay models.

- The branching fractions can be determined more precisely by using data samples of bigger sizes which are expected from BESIII.
- With more precise results, the 12% rule can be better tested.

# Bibliography

- [1] S.L. Glasho, Nucl. Phys. 22,579(1961); S. Weinberg, Phys. Rev. Lett. 42, 850 (1979); Salam, A. , 1968, in Elementary Particle Theory, Proceedings of the 8th Nobel Symposium, edited by N. Svartholrn (Almqvist and Wiksell, Stockholm).
- [2] G.'t Hooft and M. Veltman, Regularization and Renormalization of Gauge Fields, Nuclear Physics B44, 189(1972).
- [3] D. C. Joshi, *Introduction to Quantum Electrodynamics and Particle Physics*, I. K. International, New Dehli (2006).
- [4] Mike Guidry, *Gauge Field Theories: An Introduction with Applications*, John Wiley and Sons, Inc. 1999.
- [5] An Introduction to particle Physics and the Standard Model, Robert Mann, CRC Press, taylor and Francis Group, LLC (2010).
- [6] J. R. Taylor et al, *Modern Physics for Scientists and Engineers*, 2nd, ed. Pearson Education (2007).
- [7] [http : //www.cpepweb.org/cpep\\_sm\\_large.html](http://www.cpepweb.org/cpep_sm_large.html), Retrieved on Aug.14, 2012.
- [8] A. Lundborg, The Charm of Excited Glue, A PhD Thesis, Uppsala University,(2006).  
:uu.diva-portal.org/smash/get/diva2:169616/FULLTEXT01.

- [9] P.W. Higgs, Phys. Rev. Lett. 12, 132 (1964), G.S. Guralnik, C.R. Hagen, and T.W.B. Kibble, Phys. Rev. Lett. 13, 585(1964), F. Englert and R. Brout, Phys. Rev. Lett. 13, 321 (1964).
- [10] arXiv:1207.7214v1[hep-ex]; arXiv:1207.7235v1 [hep-ex].
- [11] M. Olivier, *A New Approach to Matrix Element Re-Weighting*, A Ph.D Thesis., University Catholique de Louvain Facult des Sciences cole de Physique Center for Cosmology, Particle Physics and Phenomenology
- [12] Yorikiyo Nagashima, *Elementary Particle Physics Volume 1: Quantum Field Theory and Particles*, WILEY-VCHVerlag GmbH Co. KGaA, Weinheim 2010
- [13] W. Griener and B. Muller, *Gauge Theory of Weak Interactions*, 4th ed.,Springer-Verlag Berlin Heidelberg (2009).
- [14] David Griffiths, *Introduction to Elementary Particle Physics*, John Wily and Sons, INC., New York (1987).
- [15] <http://nige.wordpress.com/2008/01/30/book/interactions/>.
- [16] Gordan Frazer (Editor), *The New Physics*, Cambridge University Press, (2009).
- [17] Sergey Kalinin, PhD Thesis, Universite catholique de Louvain (2006)
- [18] J. D. Jackson and L. B. Okun, *Historical roots of gauge invariance* 2001, arXiv:hep-ph/0012061v5
- [19] S.S. Schweber, *QED and the Men who made it: Dyson, Feynman, Schwinger, and Tomonaga*, Princiton University press, 1994.
- [20] H. Fritzsch, M. Gell-Mann, *Proc. XVI'th Intern. Conf. on High Energy Physics*, Chicago-Batavia (1972).

- 
- [21] H. Fritzsch, M. Gell-Mann, H. Leutwyler, Phys.Lett. 47B, 365 (1973).
- [22] W. Marciano, H. Pagels, Phys.Rep. 36C, 137 (1978).
- [23] H. Meyer, AIP Conf. Proc. 74, 338 (1981).
- [24] G. Flugge, *Quarks and nuclear forces*, Springer (1982).
- [25] Alessandro Bettini, *Introduction to Elementary Particle Physics*, Cambridge University Press 2008
- [26] Yorikiyo Nagashima, *Elementary Particle Physics Vol.1: Quantum Field Theory and Particles*, Wiley VCH 2010.
- [27] Francis Halzen and Alan D. Martin, *Quarks and Leptons*, John Wiley and Sons (1984).
- [28] H.D. Politzer, Phys. Rev. Lett. 30, 1346(1976); Phys. Rep. 14C, 120(1974); D.J. Gross and F. Wilczek, Phys. Rev. Lett. 30, 1343(1973).
- [29] B.R. Holstein, *Chiral perturbation theory: An effective field theory*, Progress in Particle and Nuclear Physics 61, 3(2008).
- [30] *NRQCD, Effective Field Theories and Potential Models*, Nuclear Physics B (Proc. Suppl.) 93, 188(2001).
- [31] N. Brambilla, *Perturbative quark bound states in pNRQCD*, Nuclear Physics B (Proc. Suppl.) 96, 410(2001).
- [32] A. Vairo, *Heavy-quarkonium physics from effective-field theories*, Eur. Phys. J. A 31, 728(2007).
- [33] N. Brambilla et al., *Heavy quarkonium: progress, puzzles, and opportunities*, Eur. Phys. J. C 71:1534,2011., N. Brambilla, *Effective field theories for the heavy quarkonium*, Few Body Syst 43: 2530, (2008).

- 
- [34] A. Pineda and J. Soto, *Effective Field Theory for Ultrasoft Momenta in NRQCD and NRQED*, Nuclear Physics B (Proc. Suppl.) 64, 428(1998).
- [35] M. Gell-Man, Phys. Lett.8, 214(1964).
- [36] Z. George, *Origins of the Quark Model*, 1980.
- [37] R.E. Taylor, Rev. Mod. Phys. 63, 1991; H.W. Kendall, Rev. Mod. Phys. 63 (3), 597(1991).
- [38] R.P. Feynman, Phys. Rev. Lett. **23**, 1415(1969); R.P. Feynman, *Photonhadron Interactions*, Benjamin, NewYork, 1972.
- [39] A.V. Belitskya and A.V. Radyushkinb, *Unraveling hadron structure with generalized parton distributions*, Physics Reports 418, 1(2005).
- [40] N. Isgur and G. Karl, Phys. Lett. **B72**, 109(1977); Phys. Rev. **D20**, 1191 (1979); N. Isgur, G. Karl and R. Koniuk, Phys. Rev. Lett. **41**, 1269 (978); R. Koniuk and N. Isgur, Phys. Rev. Lett. **44**, 845 (1980).
- [41] J. M. G. Duarte, Isospin and SU(2) Symmetry, [web.mit.edu/woodson/Public/Duarte-isospin.pdf](http://web.mit.edu/woodson/Public/Duarte-isospin.pdf).
- [42] M. Gell-Mann, Phys. Rev. **92**, **883** (1953); T. Nakano and K. Nisjjima, prog. Theor. Phys. **10**, 581, (1953).
- [43] V.E. barnes, et al., *Phys. Rev. Lett.* **12**, 204 (1964).
- [44] T. Hussain and S. Jin, BESII Analysis Memo.
- [45] I J R Aitchison and A J G Hey, *Gauge Theories in Particle Physics* Vol.1, IOP Pub. Ltd. (2003).
- [46] Physics at BES-III, IHEP-Physics-Report-BES-III-2008-001-v1.

- 
- [47] K.K. Setha, Eur Phys. J. A 18, 563(2003).
- [48] <http://proza-2m.ihep.su/panda/physics/2008-10-22-itep/Seminar-Corrected-ITEP-2008.ppt>.
- [49] Feng Yuan et al, arXiv:hep-ph/9703438.
- [50] BES Collaboration, F. Liu, arXiv:hep-ex/9912006.
- [51] CLEO Collaboration, G.S. Huang, J. Phys: Conf. Ser. 9, 132(2005).
- [52] Ailin Zhang, Phys. Lett.B 647, 140(2007).
- [53] M.B. Voloshin, Review Charmonia, Progress in Particle and Nuclear Physics 61, 455(2008).
- [54] B. R. Martin and G. Shaw, *Particle Physics*, 2nd. ed., Wiley (1997).
- [55] J. J. Aubert et al., Phys. Rev. Lett. 33, 1404(1974).
- [56] J. E. Augustin et al., Phys. Rev. Lett. 33, 1406(1974).
- [57] Abrams et al., Phys. Lett. 33, 1453(1974).
- [58] N. Brambilla, *Heavy Quarkonium Physics*, arXiv:hep-ph:
- [59] Diego Bettoni, Roberto Calabrese, *Progress in Particle and Nuclear Physics* 54, 615(2005).
- [60] B. Povh et al., *Particles and Nuclie*, 3rd Ed. Springer 2002.
- [61] T.Barnes, S.Godfrey and E.S.Swanson, *Higher Charmonia*, Phys. Rev. D **72**, 054026 (2005)
- [62] T. K. Pedlar et al, CLEO Collaboration, Branching fraction measurements of  $\psi(2S)$  decay to baryon-antibaryon final states, 2008.

- 
- [63] S. Okubo, Phys. Lett.5, 163 (1963); G. Zweig, CERN Report No. 8182/TH 401, 1964; G. Zweig, CERN Report No. 8419/TH 412, 1964; J. Iizuka, Prog. Theor. Phys. Suppl. 37-38, 21(1966).
- [64] X.H. Mo et al., Study of the  $\rho\pi$  Puzzle in Charmonium Decay, High Energy Phys. Nucl. Phys. 31, 686-701 (2007); T. Appelquist and H. D. Politzer, Phys. Rev. Lett. 34, 43(1975); A. De Rujula and S. L. Glashow, Phys. Rev. Lett. 34, 46 (1975).
- [65] M. E. Franklin et al. (Mark-II Collaboration) *Measurement of  $\psi(3097)$  and  $\psi'(3686)$  Decays into Selected Hadronic Modes*, Phys. Rev. Lett. 51, 963 (1983).
- [66] X. H. Mo et al., *Study of the  $\rho\pi$  Puzzle in Charmonium Decay*, High Energy Phys. Nucl. Phys. 31, 686-701 (2007).
- [67] S. Lehti, [www.helsinki.fi/~karimaki/CMHEP/Lectures/lect7Slides.pdf](http://www.helsinki.fi/~karimaki/CMHEP/Lectures/lect7Slides.pdf).
- [68] Wolfgang Khn, New Physics Opportunities in the Charm/Tau Region: The BESIII - Experiment in Beijing, Act. al Phys. Pol. B 41(2), 2010.
- [69] R.-D. Heur, Electron Positron Colliders, arXiv:hep-ex/0111070v1, Vol.22,2001.
- [70] A. Zhemchugov, Status of BESIII, Nuclear Physics B (Proc. Suppl.) 189, 353(2009).
- [71] Yifang Wang, Physics of tau and charm, arXiv:1007.2911v1 [hep-ph],2010.
- [72] M. Zobov, New generation Electron-Positron Factories, Physics of Particles and Nuclie, 42(5), 782(211).
- [73] BESIII Collaboration, The construction of the BESIII experiment, Nucl. Instrum. Meth.A 598, 7(2009); A. Zhechoguv, Status of BESIII, Nuclear Physics B (Proc. Suppl.) 189, 353(2009); M. Ablikim et al., Design and construction of BESIII detector, Nucl. Instrum. Meth.A 614, 345(2010).

- 
- [74] R.E. Mitchell, An Experimental Review of Charmonium, 34th International Conference on High Energy Physics, Philadelphia, 2008, arXiv:0810.3231v1.
- [75] G. R. Farrar and R. D. Jackson, Phys. Re. Lett. 35, 1416(1975); S. J. Brodsky and G. P. Lepage, Phys. Rev. D 24(11), 2848(1981).
- [76] R. E. Mitchell, An Experimental Review of Charmonium, arXiv:0810.3233 v1, [hep-ex], 2008.
- [77] C. Brenner Mariottoab, M.B. Gay Ducatib and G. Ingelman arXiv:hep-ph/0111379v1,
- [78] Bing-Song Zou, The Baryon Spectroscopy from  $J/\psi$
- [79] W. Guogui et al., *Study of  $\psi' \rightarrow \Lambda \bar{\Xi}^+ \pi^-$ , BESIII Analysis Memo : Version 2.0, 2012.*
- [80] J. Z. Bai et al, BES Collaboration, measurement of  $\psi(2S)$  decays to Baryon pairs,PR D63, 03(2002).
- [81] W. D. Li et al., The offline Software for the BES-III Experiment, Proceeding of CHEP06(Mumbai, India, 13-17 February 2006).
- [82] <http://lhcb-com.web.cern.ch/lhcb-comp/Frameworks/Gaudi/>.
- [83] <http://geant4.web.cern.ch/geant4/>
- [84] S. Jadach, B.F.L. Ward and Z. Was, Phys. Rev. D63, 113009(2001).
- [85] R. G. Ping, China. Phys. C 32, 599 (2008).
- [86] J.C. Chen et al. Phys. Rev. D62, 034003(2000).
- [87] K Nakamura et al (Particle Data Group), J. Phys. G: Nucl. Part. Phys. 37 (2010) 075021.

- [88] M. Abilikm et al., *Determination of the number of  $J/\psi$  events with  $J/\psi$  inclusive decays*, Chinese Physics C, CPC(HEP & NP), 2011, XX(X): 111.
- [89] M. Changli et al., *Observation of  $\chi_{cJ}$  Decay to  $\Lambda\bar{\Lambda}\pi^+\pi^-$* , BESIII Analysis, Memo: Version 3.0, 2012.
- [90] *Quantum Chromodynamics and Colour Singlet Exchange in High Energy Interactions*, PhD Thesis,